JOURNAL OF TELECOMMUNICATIONS AND INFORMATION TECHNOLOGY

1/2014

(Contents Continued on Back Cover)

Editorial Board

Editorial Advisory Board

ISSN 1509-4553 on-line: ISSN 1899-8852

Circulation: 300 copies

Sowa – Druk na życzenie, www.sowadruk.pl, tel. 22 431-81-40

JOURNAL OF TELECOMMUNICATIONS AND INFORMATION TECHNOLOGY

Preface

Telecommunication technology is evolving at an accelerating rate. This result in the rapid growth of speed of transmission not only in backbone networks but also in access networks and gives the possibilities of creating new telecommunications services and make them available to customers. Competition between service providers and the offering of services as soon as possible often means that service quality is not good enough. Monitoring the quality of service is of great importance not only for users, but also for the operators. It allows them to finding the causes of insufficient quality and thanks to this gain competitive advantage. Unfortunately, the quality of research methods, especially those that relate to the signals associated with hearing and sight are still imperfect.

On September 30th of last year in Warsaw at the Faculty of Electronics and Information Technology of Warsaw University of Technology the Second International Conference on Quality of Telecommunication Services took place. The motto of the conference was "Quality Monetization in Telecoms". The conference was devoted to aspects: practical, standardization and research related to quality of service. The conference was jointly organized by Systemics PAB, Institute of Telecommunications of Warsaw University of Technology, and IEEE Communications Society – Chapter Warsaw.

The first five articles in this issue were delivered at the scientific session of the conference. All of them are dedicated to quality of service associated with the voice and video signals.

For many of us it may be surprising that we are still investigating the quality of voice services. Why is that? Telephone lines from year to year are becoming increasingly complex. The combination of mobile telephony, internet fixed-line, and the introduction of packet transmission in place of the connection circuit causes a gradual degradation of voice quality. What's worse, in many cases, looking for the causes of poor quality requires an individual approach. Such problems occur not only in the case of VoIP, or VoLTE, as well as in older solutions, such as mobile telephony 2G and 3G.

When the speech signal is transmitted into packets one of the causes of poor quality may be packet loss. The first article of this issue deals with the burst ratio parameter used in so called E-model, which describes the burstiness of a packet loss observed in digital networks, and extending the burst ratio definition to tandem concatenation of transmission channels being described by their individual burst ratios.

The next four articles are devoted to the quality of services associated with video signals.

The transmission of video signals was until recently reserved exclusively for broadcast TV or cable TV. Progress in the coding techniques and a significant increase of bitrate also in wireless networks enabled services such as IPTV or VToIP.

Now cable networks and broadcast television commonly offers HD video, and probably soon so will the 3D video. These new solutions require the development of other tools and methods for quality testing. Some proposals for such methods have been presented in three articles.

Although the theme of this feature topic in this issue of *Journal of Telecommunications and Information Technology* is the widely understood quality in telecommunications, some of the articles are primarily related to other subjects. All except one are associated with radio networks. Although they do not address directly the quality of service, a few of them discusses the issues that affect indirectly the quality of service. I am grateful to all the contributors of this issue. I thank the authors for their time and efforts in the presentation of their recent research results. I also would like to express my sincere thanks to the reviewers, who have helped us to ensure the quality of this publication.

Sławomir Kula
Guest Editor
Institute of Telecommunications
Warsaw University of Technology
E-mail: s.kula@tele.pw.edu.pl

Paper

Burst Ratio in Concatenated Markov-based Channels

Jakub Rachwalski and Zdzisław Papir

Department of Telecommunications, AGH University of Science and Technology, Krakow, Poland

Abstract—This paper deals with the burst ratio parameter, which describes the burstiness of a packet loss observed in digital networks. It is one of the input parameters of E-model – the most widely used method of assessing conversational quality of telephony. The burst ratio is defined for one channel scenario so it can be calculated when the whole transmission path has been characterized by a single set of parameters. The main objective of the paper is to extend the burst ratio definition when the transmission path is defined as a tandem concatenation of transmission channels being described by their individual burst ratios. It is assumed that packet loss of a single channel is described by a 2-state Markov chain. The final result of the research is an equation describing the burst ratio parameter when the transmission path consists of multiple concatenated channels. The derived formula has been validated by extensive simulations.

Keywords—burst ratio, bursty packet loss, E-Model, Quality of Service, Voice over IP.

1. Introduction

Telecommunication transmission channels can be described by multiple parameters. One of them is *packet loss*, describing the probability that a packet was not correctly delivered. This degradation can be caused by multiple factors, e.g., the transmission link error, congestion or failure of the transmission device. The effect of packet loss greatly influences the quality of real-time services – if just a fraction of packets are not delivered, the video conference or phone call service can be regarded as unusable [1], [2].

In order to better understand the behavior of packet networks, packet loss models have been developed. One of the common approaches is to model packet loss using a 2-state Markov model [3], which is a special case of the Gilbert-Elliott model [4]. It describes dependency in packet loss by introducing two transmission channel states: *transmitting* and *losing*, as well as the probabilities of changing each state. Although more sophisticated models exist, like the 4-state Markov model [5] or n-state models [6], the 2-state Markov model has been proven to correctly reflect network performance if it does not include long term packet loss dependencies [7]. This research is based on the 2-state Markov model, because it provides a good balance between accuracy and simplicity.

Packet loss ratio can be easily correlated with the perceived quality of real-time applications. However, the degree of degradation varies greatly depending on a spectrum of factors. One factor is the codec used for transmission. The incorporated techniques of packet loss recovery [8] may significantly decrease the amount of lost information and therefore improve overall quality. The next factor influencing the degree of deterioration is the size of the packet – it is clear that the loss of a packet which includes one second of a conversation has a greater influence on the quality than a loss of a 20 millisecond frame. The degree of quality degradation also depends on the packet loss distribution. It has been observed that if consecutive packets are lost, the voice or video are more impaired than when the lost packets are evenly distributed within the transmission [9], [10]. Therefore, it is very important to monitor and measure the packet loss distribution. One of its quantifiers is the burst ratio factor.

Burst ratio is used to describe packet loss distribution in digital networks. Moreover, it is one of the input arguments of the widely used analytical speech quality measurement method, the ITU-T E-model [11]. Although the definition of the parameter is simple, its usage is not very convenient. The biggest drawback is the fact that in order to use it, burst ratio must be measured for the whole end-to-end connection. However, packets are usually transmitted through numerous different networks, each characterized by its own burst ratio value. The parameter definition does not show how to calculate its value in that scenario – can the burst ratio values simply be added up to result in the cumulative value? Therefore, the influence of single channel performance on the quality perceived by end users cannot be analyzed.

Much research has been carried out on packet loss analysis using the E-model [12]–[14]. However, only one piece of research dealt with the problem of channel concatenation [15] assumes that the burst ratio of separate channels needs be multiplied in order to calculate the burst ratio of the whole connection. However, in this paper we have carefully studied the matter and we have showed that this assumption is wrong.

This paper deals with the issue by thoroughly analyzing the additivity properties of the burst ratio parameter. It gives a precise answer to the question of how to calculate the cumulative burst ratio when the whole path consists of multiple independent channels. The results of the research can be helpful in designing and managing networks as well as developing voice and video applications.

This paper is structured as follows. In Section 2 we describe in detail the burst ratio. In Section 3 we develop the equations which define the burst ratio in the multiple channels environment. In Section 4 a simplified equation

which reveals the nature of burst ratio is presented. It also includes calculations of the error induced by the simplification. Section 5 is devoted to describing and presenting the results of the simulations which validate the provided equations. Finally, the conclusions are given in Section 6.

2. Burst Ratio Overview

The burst ratio parameter (denoted in the equations as *BurstR*) has been defined in [16]. It quantifies the packet loss burstiness. It is calculated as the ratio of the measured average length of the packet loss bursts to the average length of the bursts in the case of random loss:

$$BurstR = \frac{\text{Average measured burst length}}{\text{Expected average burst length for random loss}}, \tag{1}$$

where the burst length is the number of consecutively lost packets. In the case of random loss, the expected average burst length is given as follows (packet loss probability is denoted as Ppl):

$$\mu = \frac{1}{1-\dfrac{Ppl}{100}}. \tag{2}$$

Packet losses in digital networks are commonly modeled using a 2-state Markov chain. An example of the chain is depicted in Fig. 1.

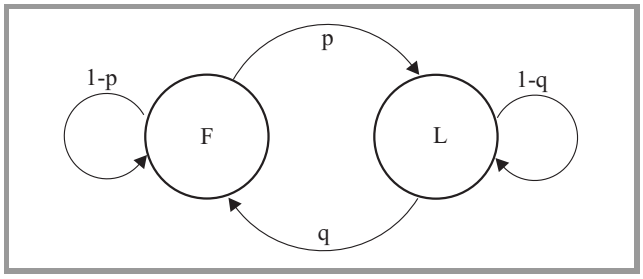

Fig. 1. 2-state Markov loss model.

In this case, if the channel successfully transmits a packet, it is in the F (Found) state. If the packet is lost, the channel is in the L (Lost) state. The p and q represent the probabilities of the channel switching between the L and F states.
According to [11], given the channel modeled in this way the *BurstR* can be calculated as:

$$BurstR = \frac{1}{p+q}, \tag{3}$$

while the packet loss is:

$$Ppl = \frac{p}{p+q} \cdot 100. \tag{4}$$

In the next section the additivity properties of the burst ratio are investigated.

3. Burst Ratio Calculation over Concatenated Channels

This section deals with the problem of using the burst ratio when the transmission path is not a single element, but consists of multiple independent packet transmission channels of known characteristics. It is depicted in Fig. 2 by a path that consists of n channels, each characterized by its own packet loss rate and packet loss burstiness.

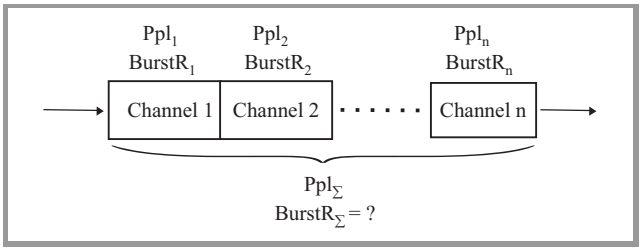

Fig. 2. The problem of the burst ratio in merged channels network.

When considering the packet loss of multiple merged channels, it must be remembered that its value in each channel is independent of other channels. Therefore, the packet loss of a path that consists of multiple channels can be described using the equations for percent addition. Eq. (5) presents the packet loss of a path that contains two channels, each characterized by packet loss, respectively Ppl_1 and Ppl_2:

$$Ppl_{1+2} = Ppl_1 + Ppl_2 - \frac{Ppl_1 \cdot Ppl_2}{100}. \tag{5}$$

The packet loss of a path that contains n multiple channels, each characterized by packet loss Ppl_n, is described by the following formula for percent addition:

$$Ppl_\Sigma = \left(1 - \prod\left(1 - \frac{Ppl_n}{100}\right)\right) \cdot 100 \tag{6}$$

Studying the burst ratio of the path consisting of multiple channels is much more complex. Referring to Fig. 2, if all merged channels are modeled with a 2-state Markov chain, then the analysis of the burst ratio of the whole path is the analysis of multiple Markov chains in a serial connection. A formula for the burst ratio of a path that contains only one channel is presented in Eq. (4). It contains probabilities of switching between the transmitting and losing state (p and q) that characterize the channel. When the path contains two channels, Channel 1 and Channel 2, in order to calculate the $BurstR_{1+2}$ value of the whole path, the probabilities p_{1+2} and q_{1+2} of the whole path must be known, as presented in the formula

$$BurstR_{1+2} = \frac{1}{p_{1+2}+q_{1+2}}. \tag{7}$$

Due to the fact that the considered path consists of two channels, the state of the total path is described by the pair: (state of Channel 1, state of Channel 2). Moreover,

the state of each channel can be either transmitting packets (Found) or losing packets (Lost). Therefore, the total path can be in one of four states, as depicted in Fig. 3. The figure also presents the probabilities of transitions between all the states. They use p_1 and q_1 as the probabilities of Channel 1, while p_2 and q_2 of Channel 2, as depicted in Fig. 1.

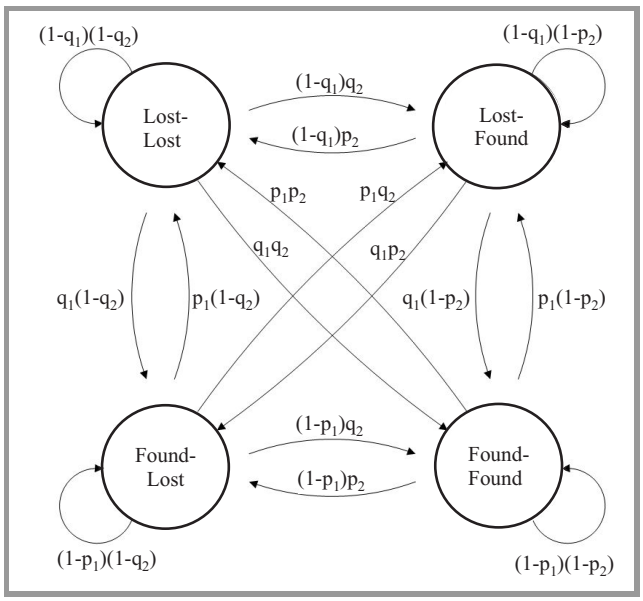

Fig. 3. Markov chains for two merged channels.

However, in order to calculate $BurstR_{1+2}$, the two channels must be considered together as a single path. In this case, the whole path is in the F state (as depicted in Fig. 1) only if both channels are in the Found-Found state (as presented in the Fig. 3). In all other situations the path is in the L state, as at least one channel is not transmitting. Therefore, the state transition probabilities of the whole path (p_{1+2} and q_{1+2}) are

$$p_{1+2} = 1-(1-p_1)\cdot(1-p_2), \tag{8}$$

$$q_{1+2} = \frac{q_1\cdot q_2\cdot(p_1+p_2-p_1\cdot p_2)}{(p_1+q_1)\cdot(p_2+q_2)-q_1\cdot q_2}. \tag{9}$$

Combining Eqs. (8)–(9) with Eq. (7) yields the final formula for the $BurstR_{1+2}$ of two merged channels:

$$BurstR_{1+2} = \frac{(p_1+q_1)\cdot(p_2+q_2)-q_1\cdot q_2}{(p_1+q_1)\cdot(p_2+q_2)\cdot(p_1+p_2-p_1\cdot p_2)}. \tag{10}$$

$BurstR_{1+2}$ can be presented as a function of $BurstR$ and Ppl parameters of both channels by transforming it using Eqs. (3)–(4). The result is:

$$BurstR_{1+2} = \frac{Ppl_1+Ppl_2-\frac{Ppl_1\cdot Ppl_2}{100}}{\frac{Ppl_1}{BurstR_1}+\frac{Ppl_2}{BurstR_2}-\frac{Ppl_1\cdot Ppl_2}{100\cdot BurstR_1\cdot BurstR_2}}. \tag{11}$$

It can be clearly seen that within Eq. (11), the numerator is equal to Eq. (5), while the denominator is similar to Eq. (5), but with $\frac{Ppl}{BurstR}$ in place of the packet loss Ppl parameter. It must be remembered that Eq. (5), which is defined for two channels only, was extended to a more general case of n-channels, as described in Eq. (6). Using this property, Eq. (11) can be extended to describe the burst ratio of an n-channel path. The resulting formula is:

$$BurstR_{\Sigma} = \frac{1-\prod\left(1-\frac{Ppl_n}{100}\right)}{1-\prod\left(1-\frac{Ppl_n}{100\cdot BurstR_n}\right)}. \tag{12}$$

Equation (12) is the final formula to calculate the burst ratio of a transmission path consisting of n channels and with only the parameters of separate channels known.

4. Equation Simplification

In the Section 3, the burst ratio equation in cases of channel concatenation was presented. Although this equation can be successfully used for accurate calculations, it does not reveal the nature of the burst ratio, its additivity characteristics. Therefore, in this section an approximation is presented. This simplified version of the equation makes it possible to perform quick estimations, without performing accurate but time- and power-consuming calculations.
The formula which authors found to be both simple and accurate in approximating the burst ratio of a whole path that consists of n channels is:

$$BurstR_{\Sigma_{simple}} = \frac{\sum Ppl_n}{\sum\frac{Ppl_n}{BurstR_n}}. \tag{13}$$

It shows that the burst ratio of the total path can be regarded as a weighted harmonic mean of the $BurstR$ of each separate channel. It needs to be noted that the value of the simplified equation of the burst ratio of the total path is always equal to or greater then the exact formula:

$$BurstR_{\Sigma_{simple}} \geq BurstR_{\Sigma}. \tag{14}$$

The error of the simplification is as follows:

$$\varepsilon_{BurstR} = BurstR_{\Sigma_{simple}} - BurstR_{\Sigma}. \tag{15}$$

If n channels are regarded, the largest error occurs if all of them are characterized by parameters of the same value (Ppl and $BurstR$). In that case, Eq. (13) is transformed into the form:

$$BurstR_{\Sigma_{simple}} = BurstR. \tag{16}$$

In this situation, Eq. (12) can also be transformed, as follows:

$$BurstR_{\Sigma} = \frac{1-\left(1-\frac{Ppl}{100}\right)^n}{1-\left(1-\frac{Ppl}{100\cdot BurstR}\right)^n}. \tag{17}$$

Transforming this equation, the formula of the burst ratio of a single channel is given by:

$$BurstR = \frac{1-(1-\frac{Ppl_{\Sigma}}{100})^{\frac{1}{n}}}{1-(1-\frac{Ppl_{\Sigma}}{100\cdot BurstR_{\Sigma}})^{\frac{1}{n}}}. \tag{18}$$

Therefore, the error of simplification can be presented as

$$\varepsilon_{BurstR} = \frac{1-(1-\frac{Ppl_\Sigma}{100})^{\frac{1}{n}}}{1-(1-\frac{Ppl_\Sigma}{100 \cdot BurstR_\Sigma})^{\frac{1}{n}}} - BurstR_\Sigma . \qquad (19)$$

The value of maximum possible relative error η_{BurstR} (ε_{BurstR} in relation to $BurstR_\Sigma$) as a function of Ppl_Σ and $BurstR_\Sigma$, if the total path consists of only two channels ($n = 2$), is presented in Fig. 4.

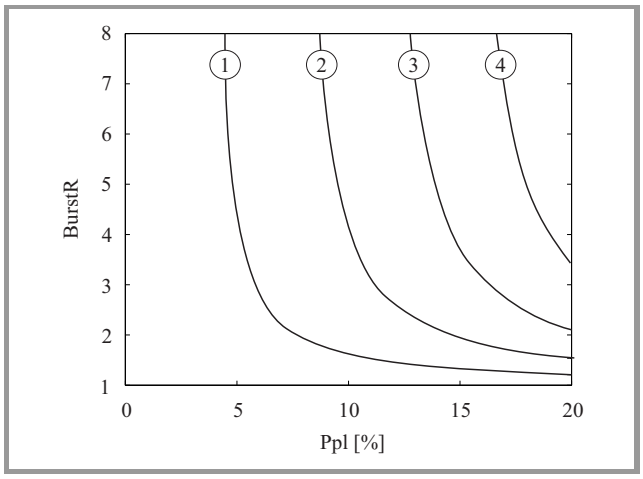

Fig. 4. The maximum possible relative error of Eq. (13) in case of two channels as a function of Ppl_Σ and $BurstR_\Sigma$.

The more channels which build up the path, the greater the maximum error generated by the simplification. Therefore, the greatest possible error induced by the simplification takes place when the path consists of $n \to \infty$ channels, each with the same packet loss, as stated below:

$$\varepsilon_{BurstR} = \lim_{n\to\infty} \frac{1-(1-\frac{Ppl_\Sigma}{100})^{\frac{1}{n}}}{1-(1-\frac{Ppl_\Sigma}{100 \cdot BurstR_\Sigma})^{\frac{1}{n}}} - BurstR_\Sigma . \qquad (20)$$

Using the properties of the natural logarithm, this equation can be transformed into the form:

$$\varepsilon_{BurstR} = \frac{ln(1-\frac{Ppl_\Sigma}{100})}{ln(1-\frac{Ppl_\Sigma}{100 \cdot BurstR_\Sigma})} - BurstR_\Sigma . \qquad (21)$$

Figure 5 presents the relative error η_{BurstR} (ε_{BurstR} in relation to $BurstR_\Sigma$) in the function of Ppl_Σ and $BurstR_\Sigma$, if the path consist of $n \to \infty$ channels, each of the same packet loss and burst ratio. This graph shows that the simplification can still be used, even if the number of concatenated channels reaches infinity, as long as the packet loss or burst ratio of the total path is small enough. In order to keep the relative error η_{BurstR} under 5%, the packet loss of the total path needs to be under 10.5% (for $BurstR_\Sigma = 8$) or $BurstR_\Sigma$ must be under 1.7 (for $Ppl_\Sigma = 20\%$).
The presented results show that the burst ratio of a transmission path which consists of multiple concatenated channels can be successfully calculated using simplified Eq. (13).

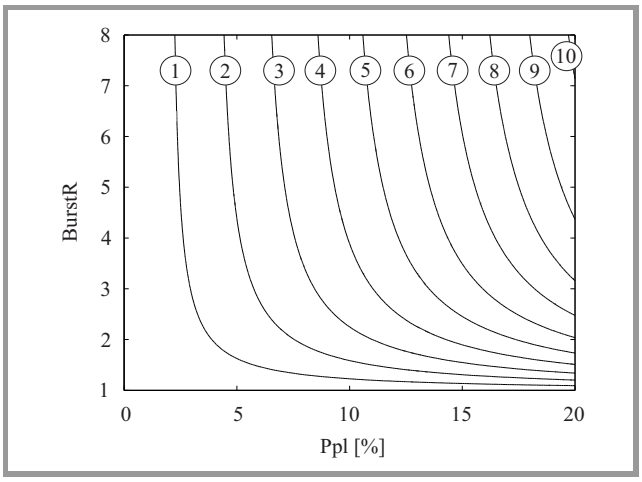

Fig. 5. The maximum possible relative error of Eq. (13) for $n \to \infty$ channels as a function of Ppl_Σ and $BurstR_\Sigma$.

It must however, be remembered that in order to keep the error of the simplification low, it cannot be used for high values of packet loss and burst ratio. Moreover, the lower the number of concatenated channels, the better the accuracy of the simplification.

5. Result Validation

In this section we present the validation methodology and validation results used to prove that Eq. (12) is the correct equation to calculate the burst ratio of a transmission path which is defined as concatenation of independent channels of known parameters.
In order to check the accuracy of the equation, simulations in Matlab were performed. The authors tried to reproduce the situation, in which data packets are transmitted through a series of channels. Each channel loses packets at a specific rate and burst ratio. Moreover, the loss is modeled using a 2-state Markov chain. The burst ratio of the total transmission path calculated using the definition Eq. (1) was compared with the value computed using Eq. (12). The latter could be calculated because the parameters of each separate transmission channel were also measured. Figure 6 presents the concept used in simulations. The simulation algorithm was designed as follows.

1. Each channel of the transmission path is modeled with a 2-state Markov chain. The p and q parameters of each Markov chain are calculated from randomly generated values of packet loss and burst ratio.
2. The first node in the chain is fed a with string of zeros (0), which represent transmitted packets.
3. The input string is processed by the Markov chain. As the result, some packets are lost, which is symbolized in the string by ones (1). The Markov chain can change its state only if it is processing a non-lost packet (zero).

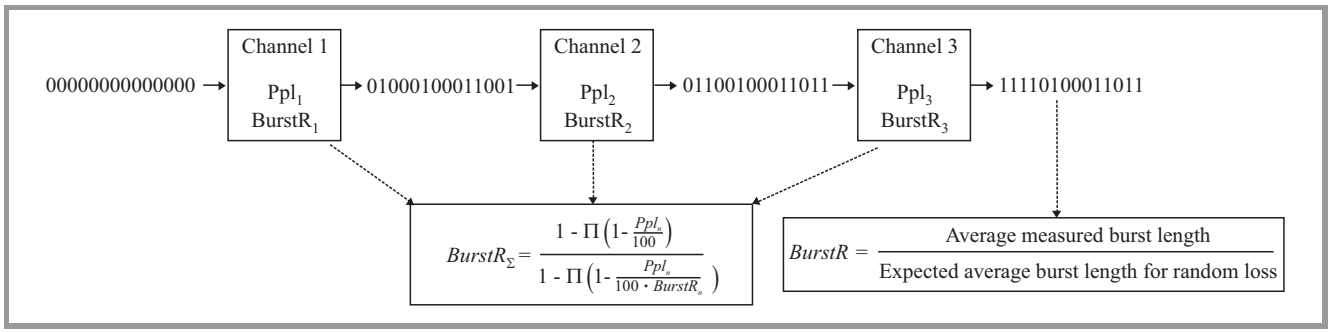

Fig. 6. The idea used in simulations run to validate Eq. (12).

Table 1
Simulation settings

	Simulation 1	Simulation 2	Simulation 3	Simulation 4
Number of packets transferred	1 000 000	10 000	1 000 000	1 000 000
Number of concatenated channels	10	10	2	10
Packet loss rate of each channel	0–1%	0–1%	0–1%	1–10%
Burst ratio of each channel	1–20			
Number of re-runs performed	1000			

4. At the output of the node the packet loss ratio and burst ratio are calculated, following the definition Eq. (1). However, only packets which were not lost (marked as zeros) before entering the node are taken into consideration. Therefore, only the burst ratio and packet loss introduced by the current node are calculated.
5. The next node of the simulated transmission path is fed with the series of ones and zeros, generated in the previous step.
6. Steps 3–5 are repeated for every simulated node.
7. When all the packets are transferred through all the 'nodesñ, the burst ratio and packet loss of the whole transmission path are calculated. Here, unlike in the previous steps, the parameters are calculated using the whole output string of ones and zeros.
8. The burst ratio of the whole transmission path is also calculated using Eq. (12). Its arguments are values of burst ratio and packet loss ratio calculated in the output of each node, as described in step 4.
9. The values of burst ratio calculated in the previous two steps are compared with each other. If they are the same, this indicates that Eq. (12) is perfectly accurate.

Simulations with 4 different settings, as described in Table 1 were performed. Figure 7 includes all the results, presented as the distribution of the relative error of the burst ratio calculation performed using Eq. (12).

The results of Simulation 1 (Fig. 7a) show that the equation was very precise – in 1000 re-runs the highest relative error was less than 0.8%.

In the next simulation, although the number of packets used have decreased, the results are still valid, as presented in Fig. 7b. However, the smaller number of packets transmitted decreased the accuracy – in over 10% of the cases the error exceeded 3%.

Simulation 3 was performed to check if the number of channels that the transmission path consists of, influences the accuracy of the equation. The results of that simulation are presented in Fig. 7c. It can be seen that the decreased number of channels slightly improved the accuracy of the equation.

The last simulation was performed to check if the packet loss rate of the channels influence the accuracy of the equation. The results are presented in Fig. 7d . Using Eq. (12) with channels which are characterized by higher and more spread values of packet loss ratio does not have any effect on the accuracy of the calculations.

The simulations undoubtedly proved that Eq. (12) correctly calculates the burst ratio value of a transmission path which consists of multiple independent channels. However, they also showed that the equation is never 100% accurate. This is caused by the fact that the burst ratio is a function of an average length of the burst of lost packets. When considering a channel concatenation, this quantity cannot be calculated with 100% accuracy, but rather with high probability. That is why all graphs present the Gaussian function.

The simulations also showed that the number of channels and their packet loss have little or no effect on the accuracy of the results. On the other hand, the number of packets transferred has a significant influence on the precision of the burst ratio calculation: for 1 million packets the 0.95 confidence interval is at the relative error of 0.4%, while for 10 thousand packets it is 3.8%. This is why it is recom-

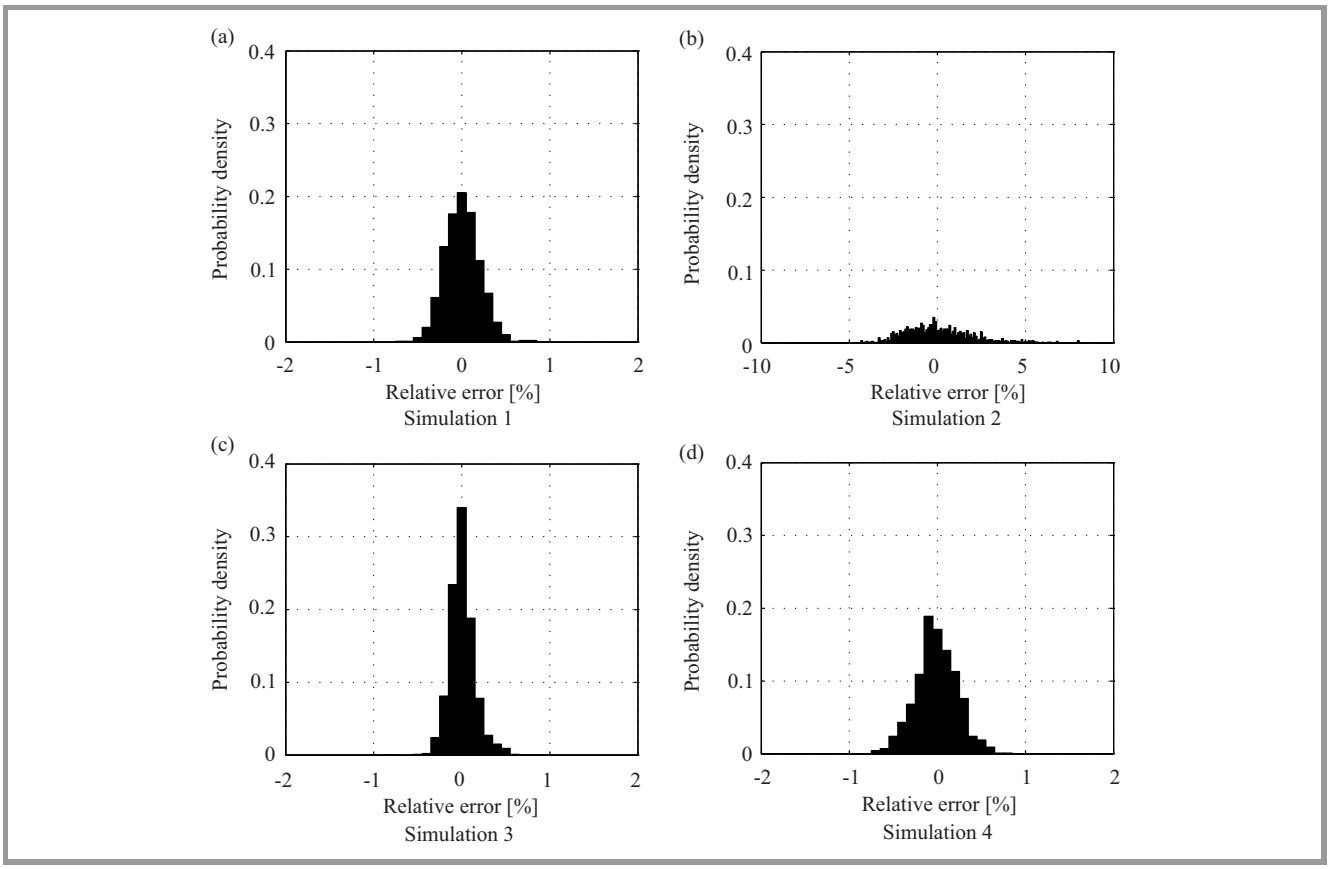

Fig. 7. The distribution of the relative error of the burst ratio calculation performed using the Eq. (12).

mended that the equation is used when dealing with mean burst ratio calculated over longer periods of time – therefore calculated over a larger number of packets – rather than the instantaneous value.

6. Conclusions

The authors have solved the problem of calculating the burst ratio when the transmission path consists of multiple channels and only the parameters of separate channels have been measured. In presented research the packet loss of each channel is modeled using a 2-state Markov chain. The solution is in the form of a function of each channel's packet loss and burst ratio. A simplification of that function is also presented, which reveals that the burst ratio of the whole transmission path can be very well approximated with a weighted harmonic mean of separate channels' properties. We also carried out a study of the error which is introduced by that simplification. The study provides information about the conditions under which the simplification is valid.

Moreover, the results of the simulation performed to validate the results is presented. The simulations showed that the provided results are correct regardless of the number of concatenated channels or the packet loss rate they introduce. However, they also indicated that the presented equation provides a very accurate result only when dealing with mean value of the burst ratio, rather than its instantaneous value.

The presented results can be used in QoS measurements and network performance assessment. Due to the fact that the burst ratio is mostly used as an input argument of the E-model, the study will help in assessing the voice quality in packet networks. The results can help evaluate the effect of a single transmission element on end-to-end quality. The presented simplified version of the final equation will help perform quick and simple estimations of the total burst ratio. The final formula can be used both during network modeling and monitoring, helping provide better quality in the real-time applications.

Acknowledgements

This work has been supported by the AGH University of Science and Technology under contract no. 11.11.230.018.

References

[1] S. Möller, *Assessment and Prediction of Speech Quality in Telecommunications*. Dordrecht, Netherlands: Kluwer, 2000.

[2] A. Raake, *Speech Quality of VoIP: Assessment and Prediction*. Chicherster, UK: Wiley, 2007.

[3] J.-C. Bolot, "Characterizing end-to-end packet delay and loss in the internet", *J. High Speed Netw.*, vol. 2, no. 3, pp. 305–323, 1993.

[4] E. Elliott, "Estimates of error rates for codes on burst-noise channels", *Bell Syst. Tech. J.*, vol. 42, no. 9, pp. 1977–1997, 1963.

[5] A. D. Clark, "Modeling the effects of burst packet loss and recency on subjective voice quality", in *Proc. IP Telephony Worksh.*, New York, 2001.

[6] H. A. Sanneck and G. Carle, "Framework model for packet loss metrics based on loss runlengths", *SPIE Proc.*, vol. 3969, pp. 177–187, 1999.

[7] M. Yajnik, S. Moon, J. Kurose, and D. Towsley, "Measurement and modelling of the temporal dependence in packet loss", in *Proc. 18th Ann. Joint Conf. IEEE Comp. Commun. Soc. INFOCOM'99*, New York, NY, USA, 1999, vol. 1, pp. 345–352.

[8] C. Perkins, O. Hodson, and V. Hardman, "A survey of packet loss recovery techniques for streaming audio", *Network, IEEE*, vol. 12, no. 5, pp. 40–48, 1998.

[9] W. Jiang and H. Schulzrinne, "Modeling of packet loss and delay and their effect on real-time multimedia service quality", in *Proc. 10th Int. Worksh. Netw. Operat. Sys. Supp. Digit. Audio and Video NOSSDAV'2000*, Chapel Hill, North Carolina, USA, 2000.

[10] L. Sun and E. C. Ifeachor, "Subjective and objective speech quality evaluation under bursty losses", in *Proc. Int. Conf. Measurement of Speech and Audio Quality in Networks MESAQIN*, Prague, Czech Republik, 2002.

[11] "The e-model, a computational model for use in transmission planning", ITU-T Rec. G. 107, 2011.

[12] M. Voznak, "E-model modification for case of cascade codecs arrangement", *Int. J. Mathem. Models Metho. Appl. Sci.*, vol. 8, pp. 1439–1447, 2011.

[13] S. Jelassi and G. Rubino, "A comparison study of automatic speech quality assessors sensitive to packet loss burstiness", in *Proc. Consumer Commun. Netw. Conf. IEEE CCNC 2011*, Las Vegas, NV, USA, 2011, pp. 415–420.

[14] W.-E. Chen, P.-J. Lin, and Y.-B. Lin, "Real-time voip quality measurement for mobile devices", *IEEE Syst. J.*, vol. 5, no. 4, pp. 538–544, 2011.

[15] I. Lopetegui, R. A. Carrasco, and S. Boussakta, "Speech quality prediction in voip concatenating multiple markov-based channels", in *Proc. 6th Adv. Int. Conf. Telecommun. AICT 2010*, Barcelona, Spain, 2010, pp. 226–230.

[16] J. W. McGowan, "Burst ratio: a measure of bursty loss on packet-based networks", US Patent 6,931,017, 2005.

Jakub Rachwalski obtained his M.Sc. from the University of Science and Technology in Krakow, Poland in 2009. He is currently a Ph.D. student under the supervision of Prof. Zdzisław Papir. His current research focuses on the Quality of Experience in VoIP applications, with special interest in the influence of the packet loss distribution on the perceived quality.

E-mail: jrachwal@agh.edu.pl
Department of Telecommunications
AGH University of Science and Technology
30 Mickiewicza Av.
30-059 Krakow, Poland

Zdzisław Papir is Professor at Department of Telecommunications (AGH University of Science and Technology in Krakow, Poland). He received the M.Sc. degree in Electrical Engineering in 1976 and Ph.D. degree in Computer Networks both from the AGH University of Science and Technology. In 1992 he received the Ph.D. Hab. degree from the Technical University of Gdańsk. He is currently lecturing on Signal Theory, Modulation and Detection Theory, and Modeling of Telecommunication Networks. In 1979 he joined the Department of Telecommunications at the University of Science and Technology, where he is currently a Professor and Deputy Chair. During 1991–1998 he made several visits at universities in Belgium, Germany, Italy, and US working on statistical modeling of telecommunication traffic. During 1994–1995 he was serving for the Polish Cable Television as a Network Design Department Manager. He co-authored five books and about 100 research papers. The book "Telecommunication traffic and packet network congestion" was awarded by the Ministry of Science and Higher Education. He was involved in organization of several international conferences at home and abroad. Between 1999–2006 he was a guest editor for IEEE Communications Magazine responsible for the Broadband Access Series. He has been participating in several R&D IST European projects (COST, Eureka Celtic, and 4th, 5th, 6th, 7th FP European programs (ACTS, ESPRIT, IST, ICT) being personally responsible for statistical modeling of telecommunication traffic and quality of experience assessment of multimedia communication services. He has also been appointed as an expert in Information and Communications Technologies by the European Commission.
E-mail: papir@kt.agh.edu.pl
Department of Telecommunications
AGH University of Science and Technology
30 Mickiewicza Av.
30-059 Krakow, Poland

Paper

New Tool for Examining QoS in the VToIP Service

Tadeus Uhl[1], Krzysztof Nowicki[2], and Stefan Paulsen[3]

[1] *Maritime University of Szczecin, Szczecin, Poland*
[2] *Gdańsk University of Technology, Gdańsk, Poland*
[3] *Flensburg University of Applied Sciences, Flensburg, Germany*

Abstract—This paper is dedicated to the subject of measuring QoS in the Video Telephony over IP (VToIP) service. QoS measurement models in general and then models designed specifically for measuring QoS in the VToIP service are presented. A new numerical tool for examining the quality of VToIP video streams VToIP is described. The tool's functionality is then put to the test in a number of analysis scenarios. The results and insights gained from the analyses are then presented in several diagrams, and interpreted. The paper concludes with a summary and an outlook on further areas of work.

Keywords—communication network, emulation tool, ITU-T G.1070, PEVQ, QoS measurement, Triple Play services, video streaming, VToIP.

1. Introduction

Quality of Service (QoS) plays a very important role in modern digital networks. The term has become a household word and can be found among other things in the definition of Next Generation Networks according to the ITU-T Standard Y.2001 [1]. In 2009, the European Parliament and European Council published directives for the standardization of networks and services [2], [3], placing great priority on quality of service.

The QoS in modern networks, and Quality of Experience (QoE) for that matter, should be measured continuously – preferably automatically. This makes specialized measurement methods and complete systems indispensable. There are, however, hardly any standardized QoE and QoS measuring methods for video-communications applications such as video-telephony. There are at present only two standards: ITU-T Rec. J.247 [4] and ITU-T G.1070 [5] to resort to. A third method for measuring the QoE of video services, the Perceptual Evaluation of Video Quality (PEVQ) Algorithm, has yet to be standardized [6]. It is one of the signal-based QoE measuring methods. According to the German license holders, the company Opticom [7], the PEVQ algorithm is in line with Recommendation J.247. So it seems it would make sense to work with this method to measure QoE in the VToIP service. However, the QoE measuring methods mentioned so far are very complex and the licenses are expensive. There are no simple, parameterized QoS measuring techniques that are quick and easy to use. Before any model can be developed, it will be necessary to clarify the relationships between QoS values and network and service parameters, admittedly using signal-based measuring methods. The analysis had to be conducted within clearly defined scenarios that yield reproducible and statistically irrefutable results. Quick analysis in meaningful, realistic environments are not possible without tools specifically designed to analyze QoS in emulations. At the moment there simply are no tools that can do that. This paper describes the design and development of such tool and its implementation.

The VToIP service operates according to Recommendation H.323 [8]. This Recommendation defines the encoding of audio and video signals. Codecs H.263, H.263+ and H.263++ are provided for video streaming. A VToIP connection can be established controlled and terminated using a range of signaling protocols. In practice, however, the SIP [9] protocol is by far the most widely used. Real-life measurements of the VToIP service have revealed that a refresh rate of 25 frames per second is usual. Common formats for the service are: CIF, QCIF, QVGA and QQVGA. From a practical point of view, this paper takes all these observations into consideration.

The paper will now present a classification of QoS measurement models in general and then those particularly designed for the VToIP service. The main impairment parameters of QoS are then presented briefly. The paper goes on to describe the newly developed numerical tool in Section 4. Following that, its functionality is tested in several various analysis scenarios (Section 5). The results and insights gained from those analysis are then presented in diagrams, and interpreted. The paper concludes in Section 6 with a summary and an outlook on future areas of work.

2. QoS Measurement Techniques for VToIP

In order to determine the QoS in a network two models are generally used: dual-ended model and single-ended model (see Fig. 1) [10]. In the case of the dual-ended model two signals are used: original and degraded. These are available uncompressed. For this reason, measurements can be carried out for both Quality of Experience (subjective evaluation) and Quality of Service (objective evaluation). When it comes to the single-ended model, only the impaired signal (compressed) is available. This allows only an

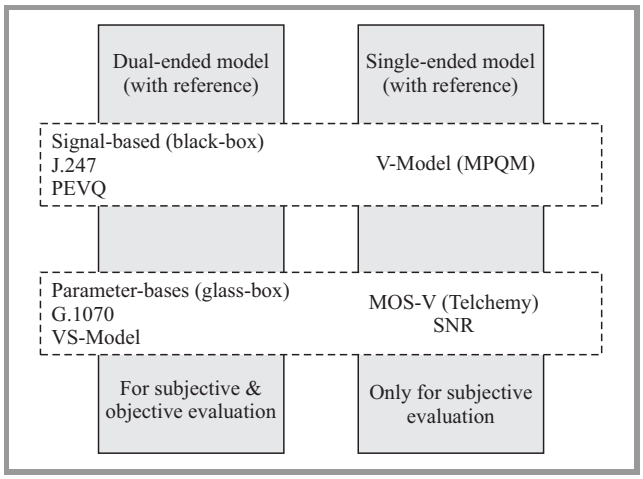

Fig. 1. Overview of QoS and QoE measurement techniques.

objective evaluation of QoS to be made. QoS measurement is referred to as "intrusive measurement" (online) in the case of the dual-ended model and as "non-intrusive measurement" (offline) in the case of the single-ended model. Two measurement techniques can be used in the two models cited: signal-based and parameter-based. The dual-ended model uses specialized algorithms to compare the input and output signals of signal-based measurements. In the case of the single-ended model, this comparison is made by using a reference signal. In both cases the system under analysis is treated as a "black box". When carrying out parameter-based measurements, a distinction is made between two types: "glass-box" and "black-box". In the first case, both the structure of the system to be assessed and the reaction of the individual system components to the reference signal are known. This knowledge is then taken into consideration within a suitable model. Additionally, the network parameters measured can be included in the calculation of the QoS. In the second case, details of the system to be assessed are limited. For this reason, only the network parameters measured and the characteristic parameters for the respective service are taken into account.
Figure 1 shows the most commonly used measurement techniques for determining the QoS in a VToIP environment. The most important techniques are: the ITU-T Rec. J.247 [4], ITU-T G.1070 [5], Perceptual Evaluation of Video Quality [6] (Part of J.247) and a proprietary solution – the VS Model [11]. They yield QoS values on the so-called MOS (Mean Opinion Score) scale (from 5, being "excellent", to 1, "bad" [12]). The new analysis tool incorporates both the PEVQ method and the VS Model.

3. QoS Impairment Parameters

QoS impairment parameters can basically be divided into two groups: network parameters and service parameters. The most influential impairment parameters in networks include: delay, jitter, packet loss, burstiness, improper packet sequencing, communications pattern, available bandwidth [13], [14]. Some of these impairments can be countered by implementing jitter buffers in the terminal equipment, one of their parameters being their size, which has a significant influence on error concealment. The second group of impairment parameters is service-related. The following parameters are associated with the VToIP service: audio and video codecs, speech sample length, video format, image refresh frequency. All of these parameters affect QoS and accordingly must be considered in any assessment of QoS. In practice two methods are used to determine whether or not impairment parameters are actually exerting a direct influence on QoS values: measuring QoS in a real environment and examining QoS using a suitable tool albeit in an emulated environment. The first approach is resource-intensive and time-consuming. The results are generally marred by a very large distribution. The second approach is admittedly extremely time-consuming during the development stage, but as soon as the tool has been successfully implemented, it is quick and easy to use. And it delivers reliable and reproducible results for a given set of parameters. This is of particular value in practical applications. That is why this paper is dedicated to the second approach. The next chapters will address the concept behind the tool, its implementation and the practical benefits of using it.

4. The New Tool for Examining QoS in the VToIP Service

Figure 2 presents a block diagram representing the concept behind the tool to examine QoS in the VToIP service that was developed during the course of the work described in this paper. To be exact, it determines the quality of the video streams in the VToIP service. That is why it came to be called QoSCalc(VSoIP) (VS standing for video streaming).

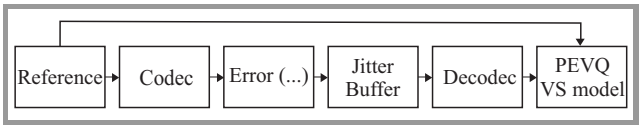

Fig. 2. Block diagram of the proposed Tool.

The following steps explain how the tool works:

- first the reference file is loaded;
- the reference signal is encoded according with the video codec selected;
- the encoded video samples are segmented and encapsulated in RTP packets in accordance with the selected settings of the parameters;
- the main impairment parameter, i.e. packet losses, is emulated in the block Error;

- the RTP packets containing the video samples are received and buffered in the jitter buffer, where they are processed. Whenever a packet loss occurs, the corresponding packet is discarded;
- once decapsulated the video samples are decoded in the next block according to the codec selected;
- finally, the received signal and the reference signal are led to the PEVQ algorithm, that then calculates the QoS as values on the MOS scale. It is also possible to input the parameters that are calculated on receipt of the RPT packets into the VS Model because it, too, is capable of determining QoS values on the MOS scale.

The tool QoSCalc(VSoIP) was developed using the programming language C Sharp. All of the steps outlined in the previous paragraph are performed on the computer. The transmission of RTP packets is done virtually within the tool itself. Figure 3 shows the tool's graphical user interface.

When using the tool QoSCalc(VSoIP), the first thing that must be done is to select a suitable reference file (see Video File panel in Fig. 3) for the video codec being used. The reference file must have a resolution that is supported by the video codec under analysis and fulfill further prerequisites (e.g., duration and content of the signal) set by the license holders in Germany of the PEVQ algorithm, i.e., the company Opticom [7]. Codec H.263 supports only the resolutions 16CIF (1408 × 1152 pixels), 4CIF (704 × 576 pixels), CIF (352 × 288 pixels), QCIF (176 × 144 pixels) and SQCIF (88 × 72 pixels), although more recent versions, H.263+ and H.263v2, do not limit resolutions and formats to quite such an extent. The selected signal is then analyzed and, among other things, its image refresh frequency, bit rate, duration and number of frames is detected. The user is asked whether height, width and image refresh frequency of the selected video should be used as a basis for a subsequent encoding. If this should not be the case, the user can enter alongside the chosen (H.263 or H.263+) alternative values and adjust the setting for bit rate (see Encoding panel in Fig. 3).

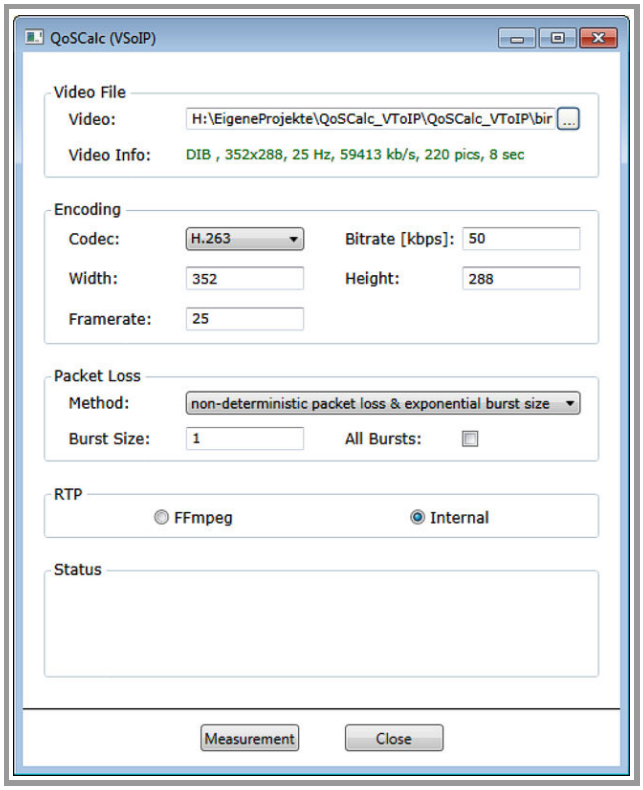

Fig. 3. Screenshot of the tool's graphical user interface.

The user can choose between three different settings to calculate PEVQ values: deterministically distributed losses at constant burst size, binomially distributed losses at constant burst size; binomially distributed losses at exponentially distributed burst size (panel Packet Loss). As a consequence of the variable burst size a series of tests comprises 15 reading points, each consisting of 31 measurements. A CSV file containing the QoS values, packet losses and, if desired, burst sizes is created by default. Besides that, the arithmetical mean, standard deviation and confidence interval are calculated for each reading point. If transformation equations exist for the VS model for the selected parameter, then the QoS values calculated according to this method are contained in the file as well. As soon as a series of tests has been completed, a window appears informing the user along with other information as well, such as duration of the measurement tests and where the CSV file has been saved. A Visual Basic macro is used to present the values as Excel data sheets in which the corresponding curves are also shown.

The user can choose between two methods of encapsulating the encoded signals into RTP packets (panel RTP). Choosing Internal will prompt the tool to encapsulate the signals according to Recommendation RFC 2190 [15]. Choosing FFmpeg, however, will cause the corresponding software tool [16] to packet the individual RTP packets, one advantage here being the large number of codecs (H.264 as well) for which a corresponding RTP segmenting is supported and which must therefore not be separately implemented. The developers are working feverishly to provide this kind of encapsulation in future versions of QoSCalc(VSoIP). Finally, the panel Status displays the current status of test series in progress.

5. Analysis Scenarios

The numerical tool QoSCalc(VSoIP) has been tested in a number of analyses. It delivers reliable and reproducible results. Its functionality and efficiency will now be demonstrated in a number of representative measurement scenarios. The analysis scenarios exhibited the following parameters:

- video codec H.263+ with encoding rates of 1308 kbit/s and 4995 kbit/s;
- image format QVGA (320 × 240 pixels);

- image refresh rate of 25 images/s;
- binomially distributed packet losses of 0 to 20%;
- negative exponential distribution burst size with mean values of 1 to 5;
- 31 measurements per value of each of the variables (here: packet loss). This ensures that confidence intervals are achieved that are less than 10% of the mean values under analysis, with a probability of error of 5%;
- PEVQ and VS Model as the QoS measuring techniques;
- an AVI file PevqRef_qvga.avi from the company Opticom [7] was chosen as the reference video. The file is 8 seconds long.

Fig. 4. Screenshot of the reference video.

Figure 4 shows a screenshot of the reference video, and the results of the comparison study are presented in Figs. 5–8.

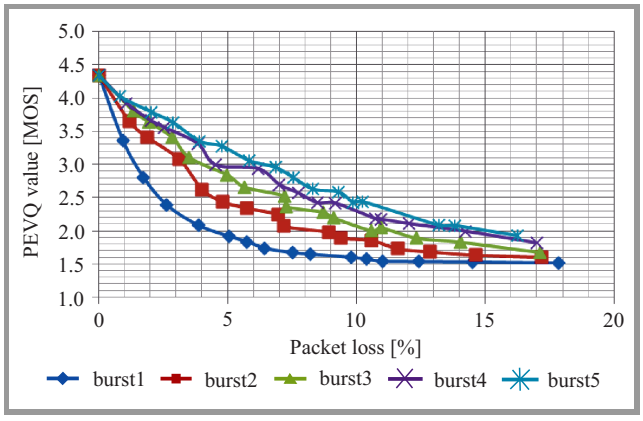

Fig. 5. PEVQ values as a function of packet losses and burst sizes at an encoding rate of 1308 kbit/s for the codec H.263+ and the image format QVGA.

Figures 5–6 show that all QoE curves develop exponentially. The curves also show that the encoding rate has a great influence on the QoE values. Burst size also has a significant influence on QoE. A burst size of 1 delivers the worst quality of experience in all three cases and improves with increasing burst size. Furthermore, the curves fall less steeply as burst size increases. The upshot of this is: it is far better for the service if fewer, larger bundles of packets are lost than lots and lots of smaller bundles. The reason for this lies in the properties of human vision. A set of curves like this could be used in the development of the parameterized QoS measuring model as was done, for example, in work [11]. In that scenario the suitability of the proposed tool, QoSCalc(VSoIP), for determining QoS in VoIP was proved beyond any doubt.

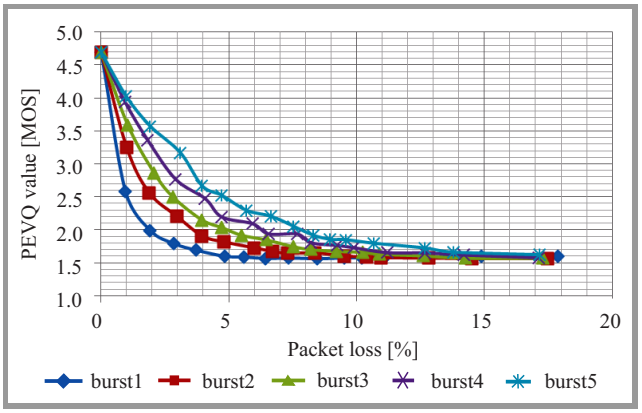

Fig. 6. PEVQ values as a function of packet losses and burst sizes at an encoding rate of 4995 kbit/s for the codec H.263+ and the image format QVGA.

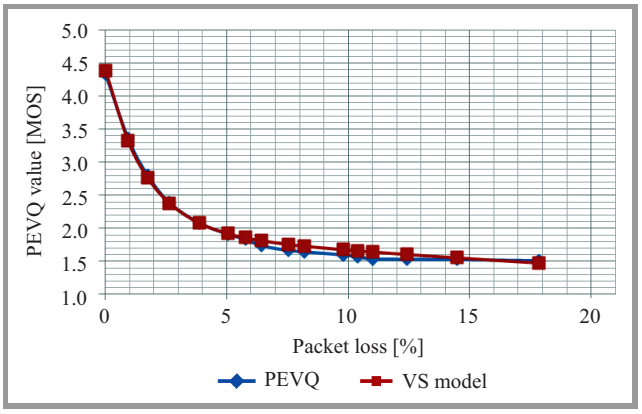

Fig. 7. QoS values as a function of packet losses gained from different measuring methods for the codec H.263+, the image format QVGA, burst size 1 and an encoding rate of 1308 kbit/s.

Figures 7–8 show that the quality of service deteriorates exponentially as packet losses increase. This is the case for both QoS measuring methods used here. The PEVQ and the VS Model curves proceed very close to each other, meaning that the numerical comparison study has proved that the VS Model is quite suitable for practical use. Whilst not forgetting that there are other various methods of measuring QoS, we have proved with this series of examinations

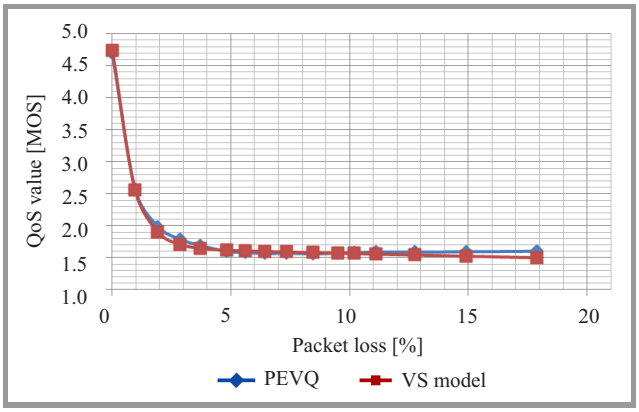

Fig. 8. QoS values as a function of packet losses gained from different measuring methods for the codec H.263+, the image format QVGA, burst size 2 and an encoding rate of 4995 kbit/s.

that QoSCalc(VSoIP), the tool developed here, is equally capable of quantifying QoS in the VToIP environment.

6. Summary and Outlook

The measurement of QoS in VToIP has been the central subject of this paper. It began with a classification of QoS measurement techniques in general before looking in more detail at those designed especially for the VToIP service. The main impairment parameters affecting VToIP were then discussed briefly. These parameters corresponded completely with the Recommendations of ITU-T [13] and ETSI [14], two leading authorities in the area. Following that, QoSCalc(VSoIP), the new numerical tool for analyzing the quality of the VToIP service was described in some detail. The design of the tool reflects recent developments in QoS measurement methodology for the VToIP service, which can only be of benefit in practical applications. The tool has room for proprietary solutions. Its user overlay is intuitive and easy to use. Several tests have proved the suitability of the new tool for examining the quality of service in VToIP. It functions impeccably and allows large-scale analyses to be configured quickly and then executed automatically. Comparable studies by other means would be both laborious and time-consuming, hardly automated as they are. This is where the new tool really shows its mettle.

In its present form the VS Model incorporated into the tool QoSCalc(VSoIP) supports the following image formats: CIF, QCIF, QVGA and QQVGA. It would make sense to expand the parameterized VS Model with further, widely-used image formats, such as: 2CIF (704×288), 4CIF (704×576), 9CIF (105×864), 16CIF (1408×1152), WQQVGA (20×120), WQVGA (40×240), VGA (640×480) and WVGA (800×480 pixels). To achieve this, further transformation formulas must be calculated for these formats, and the approach described in paper [11] can be simply taken over and applied as it is. The authors have already started work in this direction, the ultimate goal being to integrate the VS Model with the complete spectrum of image formats and the video codec H.264 within the QoS measuring system TraceView_Sim_VToIP from the company Nextragen GmbH [17] and to launch it on the telecommunications market.

The service VToIP is one of the so-called Triple Play services. It would be worthwhile developing and implementing similar QoS-analysis tools for the other real-time services, such as IPTV, since measuring QoS, especially in video services, can be quite a time-consuming endeavor, in some cases taking several minutes per measuring point. And that is where numerical tools can help. The authors intend to develop and implement a further tool that will analyze QoS in the service IPTV. The experience and insights gathered in the course of the work described in this paper will definitely be incorporated into future work.

References

[1] ITU-T Definition of NGN [Online]. Available: http://www.itu.int/rec/T-REC-Y.2001

[2] Directive 2009/140/EC of the European Parliament and of the Council of 25 November 2009 amending Directives 2002/21/EC on a common regulatory framework for electronic communications networks and services, 2002/19/EC on access to, and interconnection of, electronic communications networks and associated facilities, and 2002/20/EC on the authorisation of electronic communications networks and services (hereinafter: Better Regulation Directive). (Official Journal EU L.337/37)

[3] Directive 2009/136/EC of the European Parliament and of the Council of 25 November 2009 amending Directive 2002/22/EC on universal service and users' rights relating to electronic communications networks and services, Directive 2002/58/EC concerning the processing of personal data and the protection of privacy in the electronic communications sector and Regulation (EC) No 2006/2004 on cooperation between national authorities responsible for the enforcement of consumer protection laws (hereinafter: Citizens' Rights Directive). (Official Journal EU L 337/11)

[4] ITU-T Recommendation J.247 [Online]. Available: http://www.itu.int/rec/T-REC-J.247-200808-I

[5] ITU-T Recommendation G.1070 [Online]. Available: http://www.itu.int/rec/T-REC-G.1070/en

[6] "PEVQ Advanced Perceptual Evaluation of Video Quality" [Online]. Available: http://www.opticom.de/download/PEVQ-WP-v07-A4.pdf

[7] The company OPTICOM [Online]. Available: http://www.opticom.de

[8] ITU-T H.323 protocol suite [Online]. Available: http://www.openh323.org/standards.html

[9] IETF SIP protocol suite [Online]. Available: http://www.ietf.org/rfc/rfc3261.txt

[10] A. Raake, *Speech Quality of VoIP*. Chichester, UK: Wiley, 2006.

[11] S. Paulsen and T. Uhl, "The new, parametrised VS Model for determining the Quality of Video Streams in the video-telephony service", *Przegląd Telekomunikacyjny* (*Telecommunication Review*), no. 8–9, pp. 1155–1166, 2012.

[12] Mean Opinion Score (MOS) [Online]. Available: http://www.itu.int/rec/T-REC-P.800/en

[13] ITU-T Recommendation G.1020 [Online]. Available: http://www.itu.int/itu-t/recommendations/index.aspx?ser=G

[14] ETSI Recommendation EG 202 057-4 V1.1.1 [Online]. Available: http://www.etsi.org/deliver/etsi_eg/202000_202099/20205704/01.01.01_50/eg_20205704v010101m.pdf

[15] RTP Payload Format for H.263 Video Streams [Online]. Available: http://www.ietf.org/rfc/rfc2190.txt

[16] FFmpeg_Tool [Online]. Available: http://www.ffmpeg.org

[17] Products of the company NEXTRAGEN [Online]. Available: http://www.nextragen.de

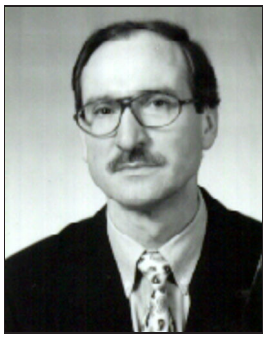

Tadeus Uhl received his M.Sc. in Telecommunications from the Academy of Technology and Agriculture in Bydgoszcz in 1975, Ph.D. from Gdańsk University of Technology in 1982 and D.Sc. from University at Dortmund (Germany) in 1992. Since 1992 he has worked as Professor at the Institute of Communications Technology, Flensburg University of Applied Sciences (Germany) and in addition since 2013 as Professor at the Institute of Transport Engineering, Maritime University of Szczecin. His main activities cover the following areas: traffic engineering, performance analysis of communications systems, measurement and evaluation of communication protocols, QoS and QoE by Triple Play services, Ethernet and IP technology. He is author or co-author of three books and some 130 papers on the subjects of LAN, WAN and NGN.

E-mail: t.uhl@am.szczecin.pl
Maritime University of Szczecin
Henryka Pobożnego st 11
70-507 Szczecin, Poland

Krzysztof Nowicki received his M.Sc. and Ph.D. in Telecommunications from Gdańsk University of Technology in 1979 and 1988, respectively. He is currently with the Faculty of Electronics, Telecommunications and Informatics, Gdańsk University of Technology, where he conducts research and teaching in computer networking, and distributed systems. He is an author or co-author of more than 150 scientific papers and books, one of them being "LAN, MAN, WAN – Computer Networks and Communication Protocols" (printed in Polish in 1998) which earned him the Ministry of Science and Higher Education Prize (2nd ed. in 2000). His book "Wired and Wireless LANs", issued in 2002 was also awarded the Ministry Prize in 2003. His scientific and research activities include network architectures, analysis of communication systems, network security problems, modeling and performance analysis of cable and wireless communication systems, analysis and design of protocols for high-speed LANs.

E-mail: know@eti.pg.gda.pl
Gdańsk University of Technology
Narutowicza st 11/12
80-952 Gdańsk, Poland

Stefan Paulsen obtained his degree in Computer Engineering from the Flensburg University of Applied Sciences in 2007. Between 2007 and 2009 he worked as a software engineer for a telecommunication management company in Kropp (Germany). In 2009 he became a scientific member of the Institute of Communications Technology at the Flensburg University of Applied Sciences, his specialist area being the development of several QoS models for communications services. Since 2012 he has worked as a software engineer for an IT service company in Flensburg (Germany). He is author or co-author of twelve papers on the subject of QoS in network services.

E-mail: stefan.paulsen@fh-flensburg.de
Flensburg University of Applied Sciences
Kanzlei st 91-93
24943 Flensburg, Germany

Paper

Analysis of Content Quality Evaluation within 3DTV Service Distribution Systems

Grzegorz Wilczewski

Faculty of Electronics and Information Technology, Warsaw University of Technology, Warsaw, Poland

Abstract—In the following paper, evaluation of quality of content distributed within 3DTV service is assessed. The performed analysis reveals a multiplicity of parameters as a compound factor defining the contemporary approach towards quality assessment. Taking into consideration a successful telecommunication service creation, an examination of content chain identifies crucial stages founding the path of modern services of stereoscopic content distribution quality evaluation.

Keywords—3D content perception, quality assessment, service creation, stereoscopic imagery.

1. Introduction

The current state of technology leads directly to a high integration of multiple services dedicated for multiple users. Concerning the fast and constantly growing needs of heterogeneity of customers, more effort is put into newer, more efficient and effective, highly developed services. Contemporary example of such a service might be stereoscopic 3DTV, where multimedia networks became prime objects of improvements and undergo constant updates. Since the information exchange is performed in an upgraded manner, the main goal of multi-service multimedia systems is to keep an appropriate quality level of service.

The main propelling power here is a motivation of transferring a certain focal point, from the service itself to the end user. An evolutionary leap from the contemporary 2D television creates a new range of business opportunities, however it is done by the cost of redesigning and remodeling of the already deployed IPTV systems. Likewise, the 3DTV service enhances the telco-branch [1]–[5], joining both content and service providers with facility manufacturers to create a separate layer of service-dedicated products.

However, in order to successfully introduce the 3DTV service to the market, quality evaluation must be performed. An identification of certain elements constructing the service is necessary to prepare a set of parameters varying the overall outcome of the deployed architecture.

2. Multidimensionality

In order to begin the analysis, one shall investigate the area of 3DTV video quality. The essential stage is to evaluate components contributing to the quality perception of the 3DTV content distribution service. Following the crude evaluation of 3DTV system, the overview of accessible model of quality evaluation is presented in the Fig. 1. By a brief inspection the multidimensionality of the problem concerning description and definition of quality within the 3DTV multimedia systems can be determined.

Starting the analysis, let's consider the guidance throughout the quality plane for the dedicated 3DTV system. Having divided the case into vertical and horizontal components of the content track, which generic contemporary telecommunication services are composed of, the quality model initiates the base layer for further conceptual model analysis. Let's follow the horizontally oriented walkthrough of the quality plane in order to determine possible anchor points for effective service quality definition.

<table>
<tr><td colspan="3">Multidimensional 3DTV quality model components & parameters</td></tr>
<tr><td>Back Office</td><td>Network</td><td>Front Office</td></tr>
<tr><td>Content Creation (techniques, coding parameters ...)</td><td>Bandwidth, packet loss</td><td rowspan="2">Viewing experience (image quality, depth quantity, naturalness, comfort, ...)</td></tr>
<tr><td>Source processing & Format (delivery-ready)</td><td>Delay, jitter synchronization</td></tr>
</table>

Fig. 1. 3DTV quality model, plane view.

From the scratch, the metrics used in quality evaluation supply the interested parties in essential information, towards the differentiation of what is perceived as good, mediocre or unacceptable quality. So, as the topic concerns services of stereoscopic data distribution, one might point out the necessity of including fundamental scheme of telecommunication services as the basic tool to model parameters determining Quality of Service (QoS). Led by research analysis [6] as well as intuitive approach, the aim of the work is to create a quality model representing insights of successful service creation. That is to satisfy the server-client interaction with apprehensible results. To verify from the point of view of the customer all the influential layers beneath the service, it is crucial to follow the path the viewed content crosses until its validity expires.

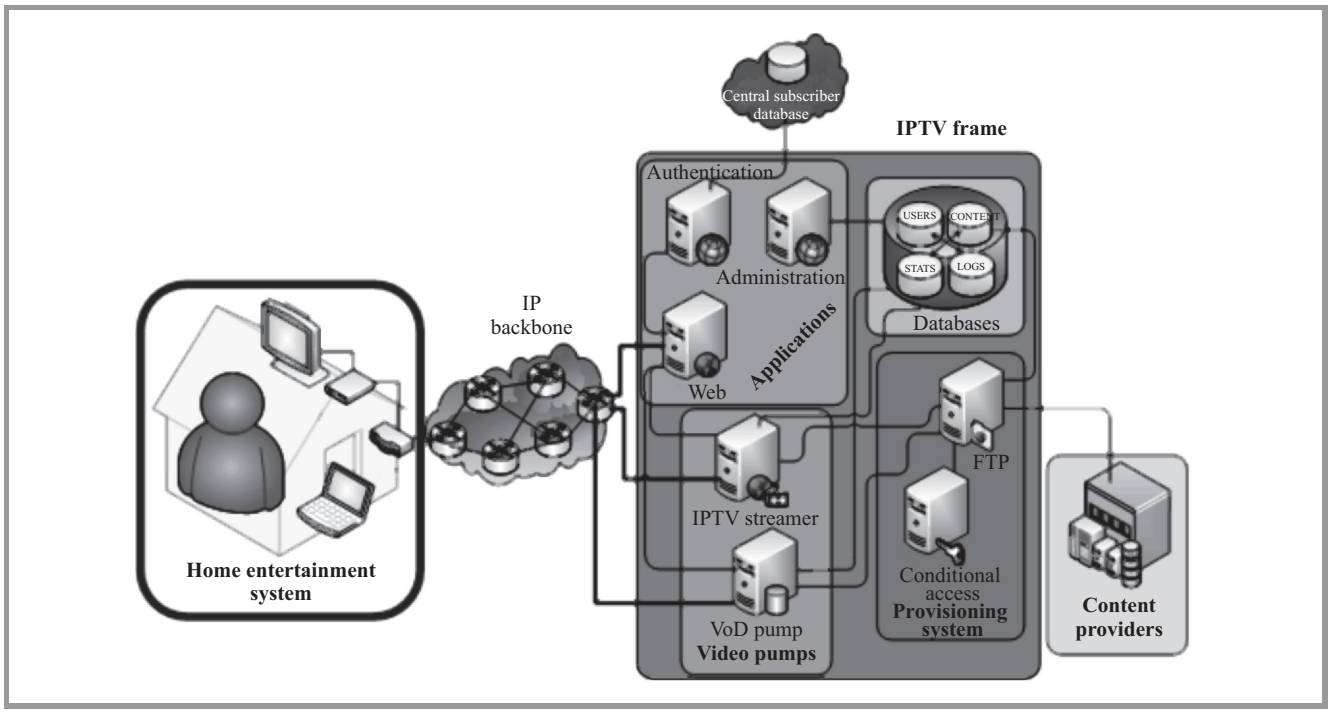

Fig. 2. Content chain inside IP based TV system.

3. Service Creation

The 3DTV service depicted on the scheme in Fig. 1 is composed of the three base vertical layers: Back Office, Network and Front Office. Core features of the aforementioned parts determine behavior of the service, varying parameters influencing final customer's experience (what is presented on the architectural layout from Fig. 2).

3.1. Back Office

The first component of the above mentioned quality plane, the Back Office module, is the origin of the service. In this unit, the video content is created, being at first acquired (in the case of real-life scenes) or synthetically built utilizing software/hardware accelerated 3D object generation. In the case of 3DTV scenario, the majority of applications is based on a video footage, constructed by using various acquisition techniques. One of the most important methods is the practice of utilizing the stereoscopic setup of cameras, camcorders receiving distinguished images. On this level of content creation a basic question rises – if the captured footage is properly composed.

Whenever the acquired video presents appropriate composition of images, thus supporting the Human Visual System (HVS) mechanics, the Back Office characteristics defines the manner in which the Content Provider delivers its product. Amongst several approaches, the ones being selected are the first order transmission of singular, elementary video streams (e.g. dual stream approach, raw data) or the utilization of high bitrate Multi-view Video Coding (MVC) expansion of a firmly established H.264 video codec [7]. Depending on the selected style, a particular stereoscopic pair of images might be given in a variety of setups. For instance, basic schemes allow the utilization of a Side-by-Side video frame positioning or Top-Bottom composition of the visual data. In some particular cases, a reduction of the vertical resolution of video frame might be observed (mainly due to throughput limitation [6], [8]).

As the content reaches the IPTV Frame (Fig. 2), on which the contemporary 3DTV service is based, asset management is performed. From the point of view of the perceived quality evaluation (QoE), this stage is of the upmost importance. Aside from ISP's content manipulation procedures, i.e., DRM or customer provisioning, the crucial point is the transcoding stage, where appropriate parts of content are transformed towards a network-native ingestion or network encapsulation, where the final video stream is formed.

3.2. Network

The area of 3DTV video quality assessment is also parameterized by a networking facility technological layout. Despite the utilized scheme of transportation (for instance Content Delivery Networks), the crude elements include the behavior of the transmission means by its resistance towards the peaks of workload. Especially in narrowband networks (i.e. wireless media) or in improperly managed fixed networks, despite the unicast paradigms of an independent content streaming, overloaded IP cores introduce phenomena which one can list as follows:

– a bandwidth limitation – significantly recognized by jerkiness or pixellate images, whenever high throughput is unavailable,

– a packet (departure/arrival) delay – in case of video sequences the inevitable timing is necessary, as a result of discarding information of no essential usage (arriving after the expected time of presentation).

– jitter – floating timing within packet ordering,

– stream synchronization – both audio and multidimensional video streams shall be delivered and decoded respectfully towards an encoder order scheme.

Network impairments take part while evaluation of the video quality is achieved. There exist several techniques utilizing network specific parameters to relate appropriate phenomena with a loss of the image quality observed on the user side [9]. From the point of view of a service developer, understanding of how the video stream is being encoded might lead to appropriate modeling and shaping of the network resources. Presented on the scheme in Fig. 3, is the generic approach of relating the visual data compression mechanisms for the 3DTV dual stream approach against the transmission manner.

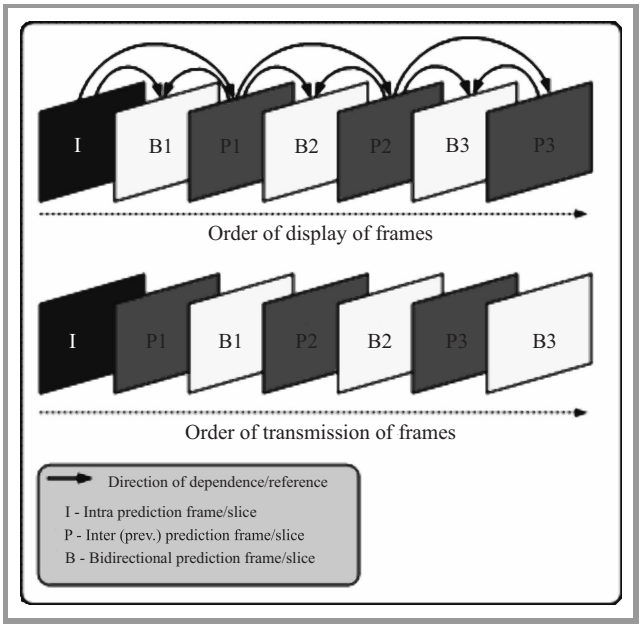

Fig. 3. Frames ordering for transmission and display.

Mentioned in [10], the prediction of inter type might be based on several frames including even those that are following to the current frame. In this point, differentiation between coded and displayed frames must be stated. The order of displaying and transmission (encoding) frames is different. Shown on the Fig. 3, the portion of 7 frames is a part of a structure called the Group of Pictures (GOP). The structure contains of diverse frames, including I, P and B types, what respectively means: intra predicted frame, inter predicted frame with reference to previous frame and bidirectional, inter predicted frame with the possible references towards the previous or further pictures. Referring to the GOP structure, it is an independent part of a motion picture containing, for instance 12 frames. The unit is recognizable by its completeness, and is always delimited by I frames (GOP consists of single "key" – I frame). Starting from the beginning, I frame is coded explicitly by the intra prediction manner, and to decode it there is no need for any previous frame data. The I picture is standalone, decodable frame and the one that has to be flawlessly transmitted. Intra prediction used for encoding process is based on the evaluation of a neighborhood of every single macroblock partition from within the frame. The I frame is thus the initial element of the Group of Pictures. Following, the P frame can be based only on intra coded frame or also the P frame. As depicted on the Fig. 3, the order of encoding determines the dependence the consecutive frames might (or not) refer to. For instance, since bidirectional frame B1 takes information about the position of certain macroblocks from both P1 and I frame, it has to be encoded after those two are completed. Therefore, the clarity of reconstruction and display of the visual data after the transmission is achievable whenever the complete sequence is not damaged. Thus, it is crucial to consider the mentioned network layer impairments while designing the policy for the 3DTV High Definition content and its requirements.

3.3. Front Office

The final stage of the content lifecycle is the Front Office layer of the quality plane. The stressed factor of the Front Office facility is the user's viewing experience. Depending on previously discussed parameters and content chain nodes, their contribution reflects the final score of perception (QoE).

The complexity of the customer side determines the layered approach to evaluate the quality of the perceived video stream. After the user's ordered stream is received and logically coherent (passing through gateway towards Set-Top-Box elements on Fig. 2), the decoding stage begins. Home Entertainment System, equipped with appropriate hardware solution, depicts 3DTV content utilizing certain compositions of the display technology and filtering stage. Market availability of Liquid Crystal Displays (LCDs), Plasma Display Panels (PDPs) and Digital Light Processing projectors (DLPs) supporting the required refresh rates extends the space of the quality evaluation problem. Moreover, sophisticated techniques of achieving stereoscopic imagery (i.e., active shutter glasses or polarization approach) add another dimension towards the definition of quality within 3DTV service, as stated in [5].

Thus, in case of a specific composition of the display technology and filtering technique, yet another case one has to consider, namely the environmental clutter of the reception area. Followed by hardware advancements, some of them might be neutralized, e.g. brightness nonuniformity caused by external reflections or manufacturing impairments. However, in explicit viewing conditions the crosstalk phenomenon will still exist [11].

Table 1
Perception of 3DTV content

Stereoscopic image perception – issues classification				
Display	Viewer	Captioning	Multi-view	Depth
Crosstalk	Condition (age, gender, previous experience)	Depth collision	Aliasing	Vergence – accommodation conflict
Geometry		Misalignment	Monocular occlusion	Depth mismatch
			View mismatch	Depth bracket
				Depth quality
				Depth discontinuity
				Interaxial distance
				Parallax

Summing up, one can identify the Front Office unit of the service creation scheme as having the heaviest impact on the perceived video quality within 3DTV content distribution systems. Further analysis shall emphasize the investigation and research of this area as crucial.

4. Viewer Experience

Referring to the content distribution chain from Fig. 2, final content perception is achieved on the Front Office side. Among various aspects of 3D content quality [12], the existence of the following areas of interest can be enumerated: image quality (assessed with the means of known metrics), depth quantity, naturalness of the scene or viewing comfort. As the 3DTV carries stereoscopic images/footage, the upmost importance is the creation of depth experience so as to perceive 3D scene. To achieve this phenomenon it is necessary to utilize consistent, coherent hardware to reproduce the feeling of the surround view. A basic classification of issues concerning 3D perception might be divided into following sections: display, user's comfort, subtitling/captioning, multi-view, depth of scene. One can distinguish multiple aspects of generation of stereoscopic vision in 3DTV systems, presented in Table 1, 3D-connected issues address the viewer's experience stage.
In order to clarify the positioned aspects of misperception observed while viewing certain content in a variable environment, the following description can be retrieved:

Display section

Crosstalk – phenomenon of image leaking from one channel to another, i.e., portion of a left-eye image seen in right-eye image, might be also observed as content dependent or not [13].

Geometry – distortions originated from irregularities of display, aside of the central point of the display surface.

Viewer section

Condition – as referred to the particular physical condition of the viewer, e.g., age, gender, the extent of the previous experience with 3DTV perception [14].

Captioning section

Depth collision – occurring while subtitles of 2D nature have to be overlaid on the 3D scene, especially of dynamic behavior.

Misalignment – discomfort of geometric gender, when left and right channel captions are not in a parallel alignment.

Multi-view section

Aliasing – depicted as high frequency components of 3D scene are improperly rendered on the display.

Monocular occlusion – occurring mainly in poorly converted 2D images into a stereoscopic view, when a part of the scene is seen only by one channel of HVS.

View mismatch – generated by impairments related to physical irregularities in acquisition hardware, e.g. lenses, sensors and inaccurate video post-processing, e.g. aperture, shutter speeds, white balance, encoding.

Depth section

Vergence – accommodation conflict – a distance dependent viewing issue: an appropriate perception of a virtual/projected 3D scene as opposed to focal comfort [5].

Depth mismatch – a phenomenon of inconsistency of HVS to reconstruct stereoscopy based on a single information cue (mismatch while natural motion of the viewer is noticed).

Depth bracket – depending on focus/vergence trade-off, the effective distance between the closest and the furthest element in the perceived scene.

Depth quality – observed in a 2D+Depth format issue of occlusive depth estimation [15].

Depth discontinuity – occurs when HVS is unable to track and follow depth variations within the fast motion scenes.

Interaxial distance – an issue of acquiring stereoscopic scene when the viewer's inter-ocular distance is smaller than (or varying) the disparity between the axes of the recording hardware lenses.

Parallax – oversaturated placement of the object due to divergence of HVS channels, when reconstructed scene tries to depict object in infinity.

The above mentioned positioning of the issues concerning the viewing experience depicts the overall complexity of the approach towards a coherent quality evaluation of 3DTV service. Some of the contemporary (2D) schemes of QoE assessment might be of use however, certain enhancements supporting the presented issues shall be obtained in order to create reliable quality metric.

5. Conclusions

The presented analysis of content quality evaluation within 3DTV service distribution systems depicts the complexity and multidimensionality of the discussed issue. The considered examination follows the crucial stages of service creation that further imply certain phenomena observed during stereoscopic content perception. The layered structure of the contemporary visual data distribution service determines the multiplicity of parameters being fundamental in conceptual and theoretical approaches towards the key point in 3DTV environment – Front Office section. The complexity of the considered issue rises rapidly, thus modeling of the quality evaluation tool becomes more compound. Resulting from research in the field of 3DTV content quality measurement, some of the mentioned parameters (especially those contributing to the content creation and processing) become plausible to determine. As for the final summary, the presented paper reveals how the contemporary IPTV, 2D TV service differs from 3DTV in terms of complexity of achievable and successful implementation of the enhanced telecommunication merchandise.

References

[1] S. Steinberg, "3DTV: Is the World Really Ready to Upgrade?", *Digital Trends*, Online Magazine, Jan. 7, 2010 [Online]. Available: http://www.digitaltrends.com/home-theater/3d-tv-is-the-world-really-ready-to-upgrade/

[2] H. Wallop, "CES 2010: 3D TVs on sale in UK by April", *The Telegraph*, Jan. 7, 2010 [Online]. Available: http://www.telegraph.co.uk/

[3] P. Otellini, Keynote Speech, Int. Consumer Electronics Show, Las Vegas (NV), Jan. 7, 2010.

[4] T. Spangler, "DirecTV to Launch 'n3D' Channel July 1", *Multichannel News*, Jun 28, 2010 [Online]. Available: http://www.multichannel.com

[5] D. Minoli, *3DTV Content Capture, Encoding and Transmission*. Chichester, UK: Wiley, 2010.

[6] B. Wonseok, L. SangJin, K. JeeGyun, and P. Sang-Il, "Korean terrestrial 3DTV broadcasting system: Current status", in *Proc. IEEE Int. Conf. Consumer Elec. ICCE 2011*, Las Vegas, NV, USA, 2011, pp. 889–890.

[7] I. E. G. Richardson, *H.264 and MPEG-4 Video Compression: Video Coding for Next-generation Multimedia*. Chichester, UK: Wiley, 2003.

[8] K. Byungsun *et al.*, "World's first hybrid 3DTV broadcasting experiment", in *Proc. IEEE Int. Symp. Broadb. Multim. Syst. Broadcast. BMSB 2012*, Seoul, South Korea, 2012, pp. 1–5.

[9] K. Wang *et al.*, "Perceived 3D TV transmission quality assessment: multi-laboratory results using absolute category rating on quality of experience scale", *IEEE Trans. Broadcast.*, vol. 58, no. 4, pp. 544–557, 2012.

[10] G. Wilczewski, "Directions of development of Video on Demand service", M.Sc. Thesis, Warsaw University of Technology, 2011.

[11] J. Bułat and L. Janowski, "Crosstalk Measurement in AGH Kraków", *VQEG Meeting*, Seoul, South Korea, June 2011.

[12] S. J. Daly, R. T. Held, and D. M. Hoffman, "Perceptual issues in stereoscopic signal processing", *IEEE Trans. Broadcast*., vol. 57, no. 2, pp. 347–361, 2011.

[13] L. Wang *et al.*, "Crosstalk evaluation in stereoscopic displays", *J. Display Technol.*, vol. 7, no. 4, pp. 208–214, 2011.

[14] S. Laframboise, D. D. Guise, and J. Faubert, "Effect of aging on stereoscopic interocular correlation", *Optom. Vision Sci*., vol. 83, no. 8, pp. 589–593, 2006.

[15] H. Wang *et al.*, "2D-to-3D Conversion Based on Depth-from-Motion", in *Proc. Int. Conf. Mechatr. Sci., Elec. Engin. Comp.*, Jilin, China, 2011, pp. 205–208.

Grzegorz Wilczewski received his B.Sc. and M.Sc. degrees in Electrical and Computer Engineering from Warsaw University of Technology, Poland, in 2009 and 2011, respectively. He is currently a Ph.D. candidate at Warsaw University of Technology. His research interests include 3DTV service quality monitoring, 3D imagery and digital signal processing.

g.wilczewski@tele.pw.edu.pl
Institute of Telecommunications
Faculty of Electronics and Information Technology
Warsaw University of Technology
Nowowiejska st 15/19
00-665 Warsaw, Poland

Paper

Quality of Variable Bitrate HD Video Transmission in New Generation Access Network

Piotr Makowski

Faculty of Electronics and Information Technology, Warsaw University of Technology, Warsaw, Poland

Abstract—Article presents influence of multiplying variable bitrate high definition (HD) video streams in an access network link on Quality of Service (QoS). The aim of a conducted study is to define key parameters influencing Quality of Experience (QoE). Numerous simulations were performed and indicators like packet loss, delay, jitter, frame loss and bandwidth utilization were observed. Moreover, two independent algorithms were used to indicate QoE values of video streams. These are SwissQual VQuadHD and Telchemy VQMon applications which provided credible full reference and no reference algorithms, respectively. In the article evaluation of accuracy of no reference algorithm is performed. In future work it is planned to build analytic model of VBR video transmission and to undertake more thorough research of transmitting multiplied HD video streams in an access network using various QoS policies and optimizing size of buffers.

Keywords—congestion in access network, Quality of Experience, streaming, variable bitrate.

1. Introduction

Nowadays, the popularity of HD and 3D television causes bandwidth demand to increase in the access network. Many publications [1], [2] prove dynamic increase of multimedia streaming in the Internet which supersedes peer-2-peer transmission model. Over-the-top television (OTT), i.e. Netflix or YouTube, becomes common and it swaps broadcast TV based on a carriers network. It is essential to deploy more efficient coding methods or guarantee more bandwidth to provide more content with better quality, particularly in the "last mile" of the network.

The European Union established a directive, which states that all members are obliged to provide connection to New Generation Access network (NGA) with bandwidth above 30 Mbit/s for 100% of households and above 100 Mbit/s for 50% [3]. Nevertheless, building NGA will proceed slowly due to the lowering prices of Internet access and the increasing costs of network investments and truck rolls. Telecommunication Service Providers (TSPs) are trying to build cheaper NGA systems using point-to-multipoint technologies like DOCSIS (Data Over Cable Service Interface Specification), PON (Passive Optical Network) or BPL (Broadband Power Line). Moreover, bandwidth demand constantly increases due to the multiplication of customer's equipment that receives video content, i.e. smartphones, tablets. Additionally, more streams are transmitted to the customer due to the aforementioned OTT as well as multiroom and Picture-In-Picture (PIP) services. All these aspects lead to insufficient bandwidth in the "last-mile" of the network. Thus, providing satisfactory Quality of Experience with existing bandwidth boundaries is still up to date.

This research focuses on the effects of various bandwidth utilization level on QoE when providing HD video streaming in IP network. The bandwidth utilization can change due to sharing the same link with other video streams and because of Internet traffic. Simulations were made in which HD content was coded producing variable bitrate (VBR) streams. Comparing with constant bitrate (CBR), VBR has better coding efficiency [4]. It maintains constant quality for the whole sequence, which is important in high-motion content, i.e. sport. Moreover, VBR allows statistical multiplexing of video streams. This multiplexing allows not only to reduce the total bandwidth utilization but also to preserve quality at the same time. The main drawback of this solution is more complicated traffic engineering and network dimensioning.

The research concentrates on quality defined as Quality of Experience, which is more generic term compared to Quality of Service. The first term includes not only Packet Loss Rate (PLR), delay and jitter but video content quality parameters. VQuadHD [5] tool from SwissQual and VQMon tool from Telchemy [6] were used to estimate subjective Mean Opinion Score (MOS), which is commonly known QoE indicator described in ITU-T P.910 standard [7]. VQuadHD implements Full Reference (FR) algorithm, i.e., it compares source with processed video. Furthermore, VQuadHD is an objective perceptual video quality measurement method and is an implementation of ITU-T J.341 recommendation [8] which is one of the most accurate full reference algorithm according to VQEG findings described in [9]. VQMon implements No Reference (NR) algorithm, i.e., it calculates results based only on receiver's data. Thus, it uses only information from RTP, MPEG2-TS, UDP and IP headers. Contrary to subjective MOS, VQMon is an objective algorithm similar to the one described in ITU-T P.1201 [10], where Pearson correlation with subjective MOS values is above 90%. In the article, the results of NR metric are compared with FR metric to validate this high correlation figure for video streams in presence of transmission errors.

Fig. 1. Sample scenes from: (a) vqeghd1_src04 and (b) vqeghd1_csrc14 sequences.

Conducted tests are introduction to innovative methods aiming to improve video quality transmission in IP network. Second section describes testing environment and architecture, whereas third part concentrates on observations' analysis and conclusions.

2. Testing Environment

In this section all HD video sequences, measuring environment and conducted tests are described.
Testing sequences were chosen from VQEG Final Report of HDTV Validation Test [11]. Two sequences illustrated in Fig. 1 have different content and coding parameters:

- vqeghd1_src04 – football game with dynamic objects moving in different directions,
- vqeghd1_csrc14 – scene in a park with low dynamic objects, however colorful and with high contrast.

Consequently, tested streams have different traffic characteristics in IP network. Common source parameters are presented in Table 1.

Table 1
Source parameters of tested sequences

Resolution	Aspect ratio	Frames per second	Chroma subsampling
HDTV 1080p (1920×1080, progressive)	16:9	29.97	4:2:2

Source files were encoded according to ITU-T H.264/MPEG4 AVC recommendation [12] using x.264 open-source encoder [13]. Streams are VBR-coded with average bitrate of 10 Mbit/s achieved during 10 seconds. Moreover, RTP and UDP protocols were used due to high capabilities of RTP/UDP stack for connectionless transmission of TV channels in Future Internet [14], [15]. In the conducted tests, MPEG2-TS/RTP/UDP stack was used instead of native RTP. There are several reasons for this assumption. Firstly, it is recommended in Broadband Forum TR-126 [16] to use main profile with level 4 coding and MPEG2-TS container. Secondly, the quality assessment algorithms described in P.1201 standard have only been evaluated for MPEG-2 TS/RTP/UDP and not for native RTP. On top of that, the size of Network Adaptation Layer (NAL) used for tested streams is not configurable in x.264 encoder. Therefore, default settings were used in which average size of NAL of type "slice" was more than 20 Kbytes, which is much more than maximum transmission unit of Ethernet frame. In this case, the difference between native RTP and MPEG2-TS used for video transmission would be subtle. Nevertheless, author of the article is aware of advantages of defining the maximum NAL size and using native RTP stack presented in [11], [15]. Including these aspects in the test scenarios is planned in the future work.

Sequences were encoded with three maximum lengths of Group of Picture (GOP) to observe influence of changing number of I frames on QoE. Table 2 contains crucial coding parameters like number of I, P and B frames, average stream bandwidth for different maximum GOP lengths.

IP network simulation tool was used as a test environment, which is compliant with ITU-T G.1050 [17] recommendation. Figure 2 presents its architecture and main settings. Model consists of core network, access node, modem, firewall and router. Traffic is sent to the core network and received at the router behind the firewall. There are five routers in the core network connected with 1 Gbit/s links. They insert together 50 ms of delay. Link between core network and access node has also 1 Gbit/s bandwidth but 0.1 ms of delay. Access node stores settings of the link to the modem for both transmission directions. These are bandwidth, BER and delay. BER is set to 10^{-10} assuming optical link according to NGA standards. It is important to mention that probability of packet loss due to transmission error is very small because 100 Mbit/s link bandwidth and simulation time is shorter than 15 seconds. Main reason of possible packet losses is queue overflow on which this research concentrates. At the end of the transmission path, there are aforementioned modem, firewall and router which are connected in a sequence and have the same settings of link bandwidth and buffers. The total minimum delay of the system is 51.1 ms and the maximum delay depends from the buffer size and obviously from the variability of

Table 2
Coding parameters for various maximum GOP lengths

	Sequence name					
	qvegd1_src04			vqeghd1_csrc14		
Maximum GOP length [frames]	15	50	250	15	50	250
Number of frames [I/P/B]	21/14/138	7/148/145	3/148/149	21/189/89	7/198/94	3/199/97
Average stream bandwidth [Mbit/s]	9.35	9.13	9.06	10.0	9.7	9.62
Standard deviation of stream bandwidth [Mbit/s]	15.1	13.3	12.0	16.7	14.4	13.5
Min. stream bandwidth [Mbit/s]	0.89	0.94	0.94	0.02	0.02	0.02
Max. stream bandwidth [Mbit/s]	59.0	66.3	61.7	73.9	82.6	83.1

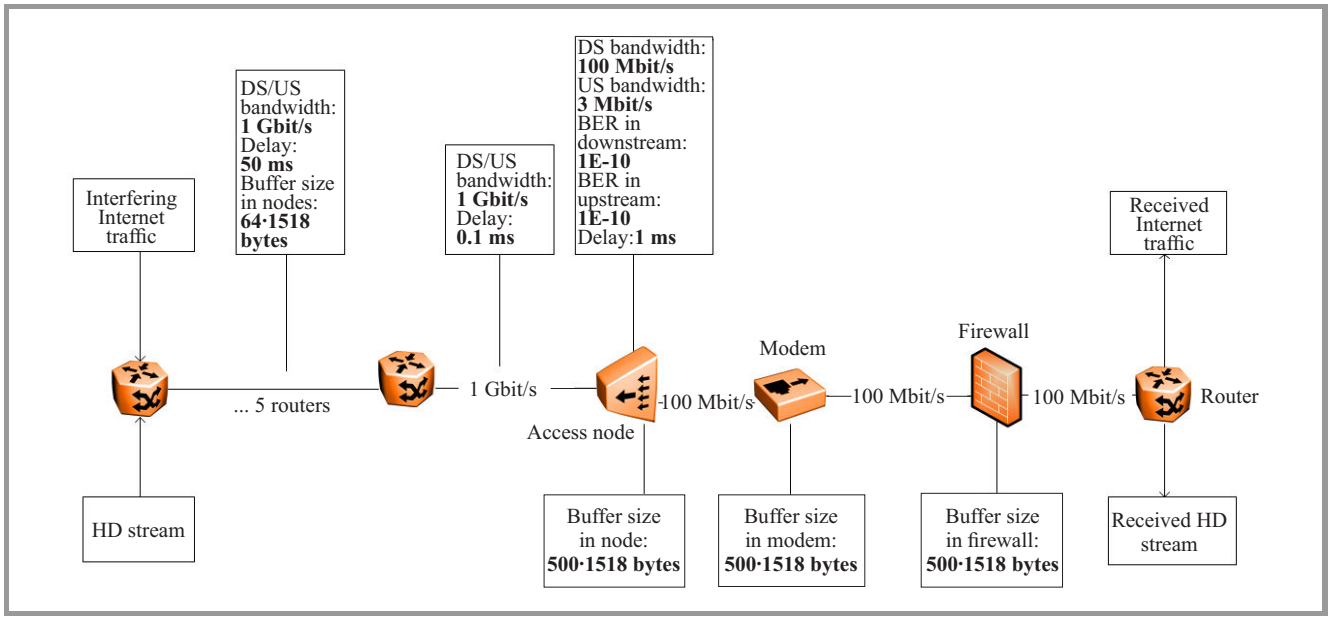

Fig. 2. Architecture and settings of G.1050 compliant network simulator.

the traffic. All elements apart from access node have buffer size limited to 97152 bytes. This value is equal to 64 Ethernet frames with size of 1518 bytes. Access node has a queue of 500 frames. This setting increases maximum delay of the whole system to 112 ms in each direction. It allows to analyse impact of the delay variations on the QoE of the video streams. 61 ms of additional delay results from the time to transmit 500 frames stored in the buffer with a speed of 100 Mbit/s.

For all six streams four tests were conducted. Firstly, bandwidth of interfering Internet traffic was increased from 0 Mbit/s to 150 Mbit/s with 15 Mbit/s step, whereas HD stream, transmitted simultaneously in the same link, was not prioritized. Therefore, buffer queues were shared between two classes of traffic (test name: same_prior). Second test differeds from first one as HD stream had higher priority compared to Internet traffic (test name: higher_prior). In the third test, interfering traffic had constant bandwidth of 15 Mbit/s, whereas quantity of HD streams was increased from 1 to 9. In the last test, all video streams were transmitted with higher priority. Therefore, only Internet traffic was not prioritized. In the tests number three and four names same_prior and higher_prior were maintained. Each simulation lasted 15 s and the total number of transmitted video streams was 683.

Testing environment allowed monitoring following parameters: packet loss rate, delay, jitter, I, P, B frame loss and bandwidth utilization. In the first and third test FIFO scheduling was applied, whereas Strict Priority Queuing (SPQ) was used in the test number two and four.

3. Observations and Conclusions

In this section, evaluation of NR algorithm by comparison with FR method is presented as well as key observations of dependencies between bandwidth utilization, number of HD streams and QoE.

Figure 3 illustrates scatter plot in which MOS-V [18] and J.341 Objective values are shown. They refer to Telchemy's VQMon and SwissQual VQuadHD metrics, respectively. From 683 test cases 521 (76%) matched to provide J.341 Objective values. Other 24% cases refer mainly to MOS-V values lower than 3 and with high percentage of impaired I-frames. The data did not matched, because it is more dif-

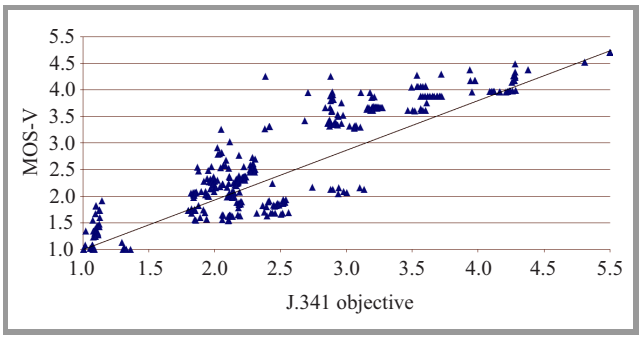

Fig. 3. Scatter plot presenting no reference MOS-V values as a function of full reference J.341 objective MOS values.

ficult to perform time and spatial alignment by VQuadHD tool for highly impaired video scenes. For 76% of data the Pearson correlation factor equals 95%. It proves that NR algorithm is sufficient for evaluation of transmission quality. Nevertheless, NR metric from Telchemy overestimates quality results in majority of cases. The reason for this is that reference video in FR algorithm provides substantial information to deeply analyze spatial artifacts, i.e. blurring, blockiness or temporal artifacts, jerkiness and freezing. These degradation types are not directly identifiable using only receiver's data. It leads to aforementioned overestimation of VQMon visible in Fig. 3.

Figure 4 illustrates results of first and second test. Providing higher priority for HD stream, i.e. higher QoS, causes

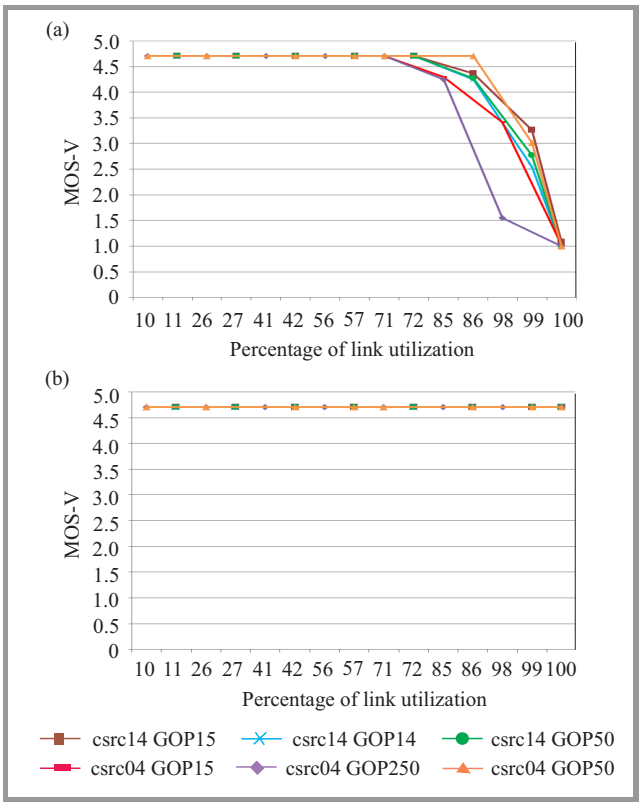

Fig. 4. Results of first and second test – MOS-V values as a function of link utilization for: (a) same_prior test and (b) higher_prior test.

packets entering the channel to be scheduled first, whereas Internet traffic as second. When stream bandwidth is not exceeding 100% utilization, queues for higher priority are not overwhelmed and packet loss rate does not occur, although Internet traffic encounters non-zero loss rate. Nevertheless, when priority for HD stream and interfering traffic is the same, higher utilization effects in decrease of MOS-V value.

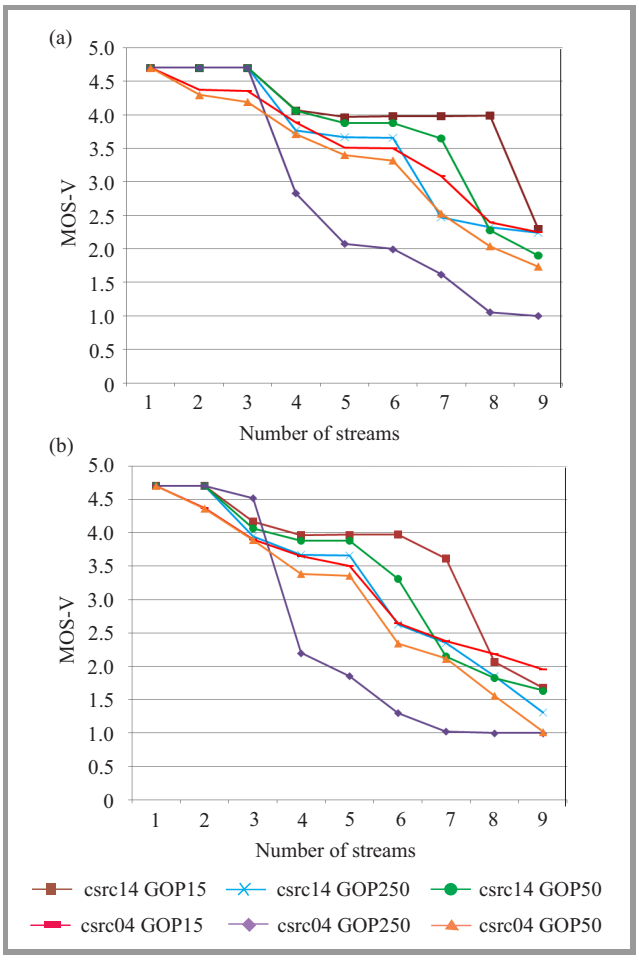

Fig. 5. Results of third and fourth test – MOS-V values as a function of number of HD streams in a link for: (a) same_prior test and (b) higher_prior test.

Packet loss rate occurs when utilization is higher than 75–80% which results in QoS drop. Reason for PLR at 75% of channel utilization and not more than 95% is VBR transmission characteristics. HD stream standard deviation of bandwidth varies from 12 to 17 Mbit/s, resulting in link congestion. Nevertheless, when streaming CBR video, the number of streams would not be higher than two assuming constant average bitrate that equals maximum bitrate. High channel utilization damages streams with long GOPs, i.e., when gap between I frames is very big. That causes substantial number of P and B frames to depend on I frames. Consequently, effects of damaged I frames are visible on numerous P and B frames, to which I frame is a reference. Therefore, increasing PLR and decreasing number of I frames, causes decay in QoE.

Figure 5 shows that increasing number of streams in a channel results in a decreased average quality. However, higher priority for video transmission is not a solution to maintain quality because the dominant share of channel utilization is video traffic and not the background Internet traffic.
As observed, in 94% of cases, for the same number of streams, videos encoded with GOP value 250 have worse quality than with GOP value 15. Therefore, profit from improved quality is not so costly due to small difference between bandwidth parameters of encoded streams (see Table 2). For tested sequences, the difference between stream with GOP value 250 and 15 is 400 kbit/s – 4% of average stream bandwidth.
From further observations, it can be concluded that serial loss of packets is more damaging for QoS than random one, which is presented in Fig. 6. Thus, using interleaving of single or multiple HD streams can result in higher average quality. However, substantial limitation of that solution is incrementing delay.

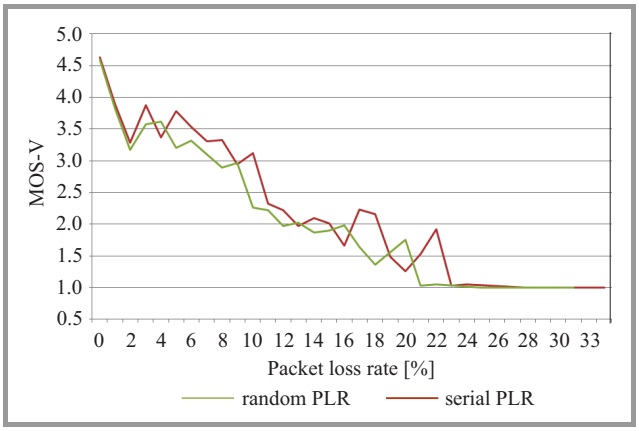

Fig. 6. Average MOS-V for random and serial packet loss rate.

Final remark refers to higher packet loss sensitivity of vqeghd1_src04 stream compared to vqeghd1_csrc14. Dynamic movement in the video causes that the traffic has lower deviation because motion vectors prediction done in the interframe domain by the encoder is not so efficient. It results in higher bandwidth consumed by P and B frames than it is in the static video sequences. It leads to less variable traffic. As a consequence, a video with lower deviation encounters more packet loss rate and is more fragile to network congestions what illustrates Fig. 7. In the presence of more than 90 Mbit/s of Internet traffic, buffers of access nodes are almost full. Congestion causes a delay of 112 ms to majority of video packets and probability of packet loss rises. Figure 7 presents that vqeghd1_src04 with lower deviation lost nearly 600 packets and vqeghd1_csrc14 lost less than 400. It is important to mention that the average bandwidth of vqeghd1_src04 is lower what proves that higher PLR is not an effect of more data sent in the channel (Table 2).
Furthermore, Fig. 7 shows that delay of 112 ms is a reason of packet loss, because it results in queue overflow. On one hand, appropriate buffer dimensioning can be a solution

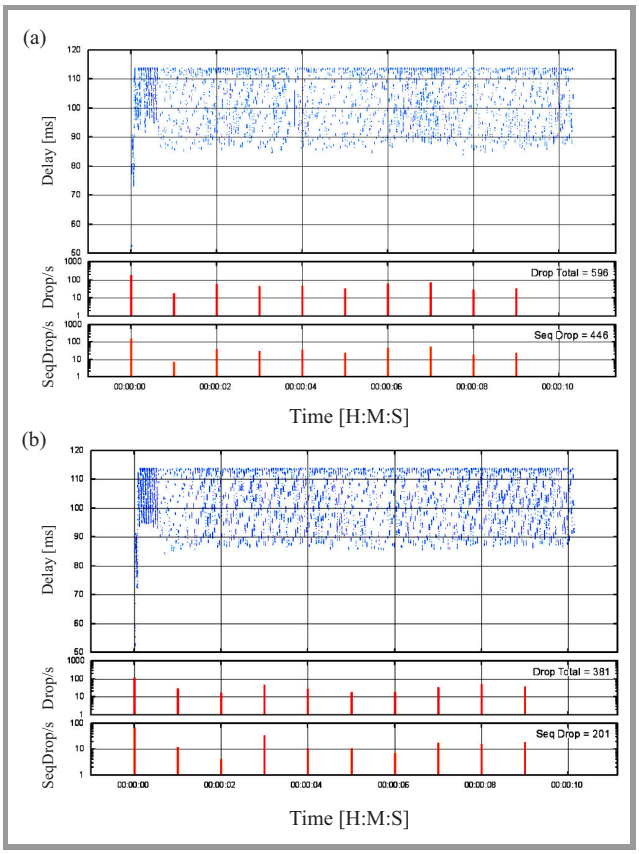

Fig. 7. Delay, packet drop and sequential packet drop values for: (a) vqeghd1_src04 and (b) vqeghd1_csrc14 streams in presence of more than 90 Mbit/s of concurrent Internet traffic.

for congestion avoidance in the presence of multiple HD streams. On the other hand, increasing buffer size causing delay of more than 3–5 seconds might be unsatisfactory solution, particularly for IPTV sport spectators.

4. Summary

This research presents influence of multiplying streams in an access network link on quality of HD video transmission. Consequences of an access network congestion evidently stunt development of new services, particularly when investments in very high broadband NGA networks progress moderately. VBR video streaming is proposed in order to facilitate transmission of multiple HD content to customer. Nevertheless, better coding efficiency causes higher deviation of bandwidth, thus traffic engineering and network dimensioning are getting more complicated.
Presented degradation of video quality is an obvious effect of network congestion. The research proved that increasing QoS for all video streams in a channel does not result in increasing QoE of HD content when video is dominant traffic in a channel. Moreover, it was observed that serial packet losses caused more severe effect on quality than random ones. In addition, sequences with lower deviation were more exposed on packet loss when congestion appears.

Furthermore, it was proved that VBR coding with high GOP values is not efficient. Short GOP values compared to long ones do not increase average bandwidth significantly, whereas quality gain is evident.
Last but not least, it was shown that NR algorithm is applicable to evaluate quality of video transmission.
In the future work, it is planned to take into consideration various NAL size settings and their influence on quality of service. It is also planned to analyze the influence of various QoS policies (i.e. shaping and scheduling) and network buffer sizes for multiple video streams in order to observe behavior and potential profit of statistical multiplexing.

References

[1] N. Anderson, "P2P traffic drops as streaming video grows in popularity", *Ars Technica* [Online]. Available http://arstechnica.com, retrieved 14.01.2013.

[2] C. Labovitz *et al.*, "ATLAS Internet Observatory 2009 Anual Report" [Online]. Available: http://www.nanog.org/meetings/nanog47/presentations/Monday/Labovitz_ObserveReport_N47_Mon.pdf, retrieved 14.01.2013.

[3] "Digital Agenda for Europe: Pillar IV: Fast and ultra-fast Internet access", European Commission [Online]. Available: http://ec.europa.eu/4/en/our-goals/pillar-iv-fast-and-ultra-fast-internet-access, retrieved 6.03.2013.

[4] T. Lakshman, A. Ortega, and A. Reibman, "VBR video: Tradeoffs and potentials", *Proc. of the IEEE*, vol. 86, no. 5, pp. 952–973, 1998.

[5] VQuadHD official Website [Online]. Available: http://www.vquad-hd.info, retrieved 10.10.2013.

[6] Telchemy [Online]. Available: http://www.telchemy.com/appnotes/Understanding%20IP%20Video%20Quality%20Metrics.pdf, retrieved 23.03.2013.

[7] "Subjective video quality assessment for multimedia applications", ITU-T Rec. P.910, 2008.

[8] "Objective perceptual multimedia video quality measurement of HDTV for digital cable television in the presence of a full reference", ITU-T Rec. J.341, 2011.

[9] "Report on the Validation of Video Quality Models for High Definition Video Content", VQEG, 2010.

[10] "Parametric non-intrusive assessment of audiovisual media streaming quality", ITU-T Rec. P.1201, 2012.

[11] T. Uhl, S. Paulsen, and K. Nowicki, "Transport possibility for MPEG-4/AVC and MPEG-2 encoded video data in IPTV: A comparison study", in *Proc. 10th Int. Conf. "Mulimedia w Biznesie i Zarządzaniu"* (*"Multimedia in Business and Management"*), Częstochowa, Poland, 2013, pp. 83–95.

[12] "Advanced video coding for generic audiovisual services", ITU-T Rec. H.264, 2010.

[13] VideoLan organisation [Online]. Available: http://www.videolan.org, retrieved 29.12.2012.

[14] J. Mongay Batalla and P. Krawiec, "Nowe scenariusze biznesowe wykorzystujące możliwosci protokołu IPv6", *Przegląd Telekomunikacyjny + Wiadomości Telekomunikacyjne*, nr 8–9, pp. 1323–1331, 2012 (in Polish).

[15] A. MacAulay, B. Felts, and Y. Fisher, "Whitepaper – IP Streaming of MPEG-4: Native RTP vs MPEG-2 Transport Stream", Envivio, 2005.

[16] Telchemy [Online]. Available: http://www.telchemy.com/vqmon.php, retrieved 23.03.2013.

[17] "Broadband Forum", Tech. Rep. TR-126 Triple-play Services Quality of Experience (QoE) Requirements, 2006.

[18] "Network model for evaluating multimedia transmission performance over Internet Protocol", ITU-T Rec. G.1050, 2011.

Piotr Makowski graduated from Telecommunication at Faculty of Electronics and Information Technology and received M.Sc. in 2009. In 2010 he started Ph.D. studies in video transmission quality domain. Since 2008 he is senior specialist in R&D at Orange Group responsible for researches and tests in xDSL access network domain and architecture of access network and development of new access technologies. His main activities are related to xDSL, video transmission, access network technology and video transmission quality domain. He is author of two articles regarding VDSL2 testing methodology and parameters analysis and a paper describing parametric model of video conference quality. In 2010 he applied for a patent to European Patent Office with invention crosstalk reduction by DPBO parameters determination.
E-mail: p.makowski@tele.pw.edu.pl
Institute of Telecommunications
Faculty of Electronics and Information Technology
Warsaw University of Technology
Nowowiejska st 15/19
00-665 Warsaw, Poland

Paper

Videotoms in Objective and Subjective Quality Tests of Video

Łukasz Trzcianowski

Faculty of Electronics and Information Technology, Warsaw University of Technology, Warsaw, Poland

Abstract—This paper proposes idea of videotoms usage in quality tests of video signals. This concept simplifies parametric model creation for television services such as IPTV (Internet Protocol Television), VoD (Video on Demand) and others. Videotom is simple, well-defined video sequence in the context of video quality tests. Presented idea was used in both objective and subjective tests of influence selected network parameters: jitter of delay, packet loss and packet corrupt on the video quality measured using Mean Square Error (MSE) and Mean Opinion Score (MOS) metrics. Results showed that proposed method is useful especially for subjective tests and it can reduce costs and time for them.

Keywords—Digital Television, IPTV, Quality of Service, Videotoms, VoD.

1. Introduction

In recent years, strong and dynamic evaluation of multimedia services in the telecommunication networks can be observed. In addition to standard terrestrial television occurs IPTV and also others interactive TV services created in broadband networks based on IP protocol usage. Their attractiveness from customer point of view is not only measured by the price but also by the quality. Service provider looks at the quality from the perspective of network parameters, whereas from user side much more important is his satisfaction with the service provided. Defining relationship between those two different approaches to quality is a real challenge. Evidence of this is the fact that amount of work researches carried out by ITU and VQEG have not yet led to creation of parametric model similar to those for telephony and videotelephony (ITU-T recommendation G.107 [1], ITU-T recommendation G.1070 [2]). Nothing surprising, since TV services are very complicated and very difficult in a proper modeling in context of quality assessment.

Most of the studies done so far keep focus on quality tests a few selected "television sequences" varying volatility (high motion, low motion) and level of details. Those video signal representations are used to show the impact of the changes like broadcasting, encoding, transmission or reception conditions on objective or subjective quality. That approach is not without drawbacks and weaknesses, because the same tests for different set of video sequences caused that received results will be significantly different. Identification all possible cases is not possible and the creation of quality model that would be reflected in the actual systems requires a lot of testing and analysis [3]–[7]. For that reason, purposeful is to move research on simplified model in which "television sequences" will be replaced with videotoms – video samples which content is clearly defined. This approach allows on significant simplification not only for costly subjective tests but also for the whole process of analysis relationship between objective and subjective quality.

2. Videotoms Concept and Visual Human Perception

The mechanisms of visual human perception are very complex and their in-depth analysis is still the subject of research engineers, doctors and psychologists. In greatly simplified the process of seeing can be summarized as follows. First, the human eye captures light reflections associated with the observed object and then it is converted and transferred by nerve cells to the brain, which interprets received information and creates final impression. Various properties of that process as well as additional conditions such as emotional state, tiredness, past experiences can influence how the image will be interpreted and in result received. It is also really important how effects are presented as an object of observation. In case of video sequences can say that significant role in their creation process should not be fitting them to TV conditions, but rather adapting the image to the general nature of human perception. Considering that in video samples creation process it's needed to take into account a number of dependencies related to that. Pictures used in this process should have continuous and constant form and structure. Removed should be any excess, irrelevant information that disturbs in unambiguous interpretation, because the human ability to perceive is more limited when the images are abstract or inconsistent. Apart from that there are many other important elements that necessarily need to be taken into account in the process of creating video sequences from pictures such as contrast, brightness, details and diversity. If we add that the knowledge of the picture that we see speeds up interpretation process we can create appropriate test sequences. Presented approach author called the concept of videotoms – creation of simple, well-defined video pictures that are known to user. Videotom name comes from logatom word defined in speech audiometry, but newly introduced concept is related only to video, not audio signals. The definition refers to simple, well-defined video sequences. It's worth

Table 1
Reference video sequences

Name	Blue cube	Green rectangle	Red balls
Description	Spinning blue cube	Moving green rectangle from the left side to right side	Red balls falling down at the different speed
Characteristic	High motion sequence with small number of details	Low motion sequence with small number of details	Average/high motion sequence with large number of details
Duration	10 s		
Codec	MPEG4 AVC		
Resolution	544 × 396 pixels		
Maximum bit rate	1662 kbit/s	158 kbit/s	1885 kbit/s

to noting that videotoms suit perfectly to subjective quality tests, because observer always notice distortion in observed video picture – in case of normal "television sequences" distortions can be unnoticed. The use of such video sequences should allow receiving more reliable results, reducing the number of tests and simplifying analysis process for them.

3. Test Conditions and Reference Samples

To show videotoms usage in both subjective and objective quality tests according to Young-Helmholtz theory of trichromatic color vision and to engage three receptors: short-preferring (blue), middle-preferring (green) and long-preferring in the same way the three video sequences was created as shown in Figs. 1–3.

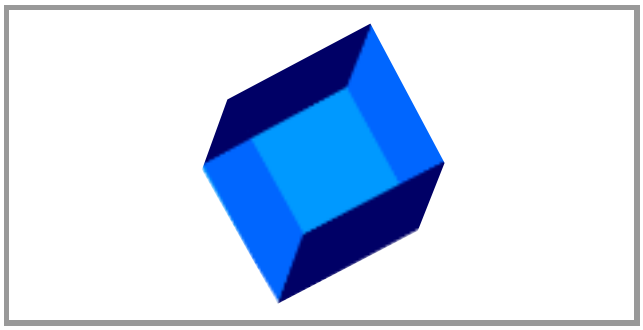

Fig. 1. Video sequence "Blue cube".

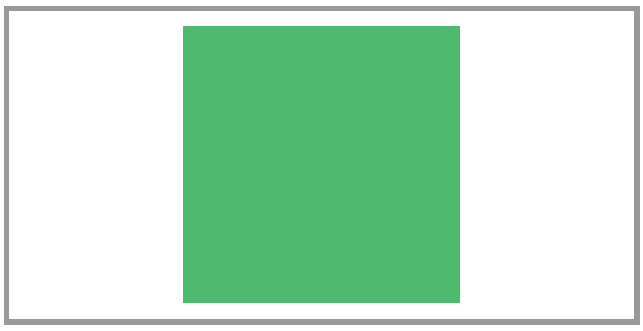

Fig. 2. Video sequence "Green rectangle".

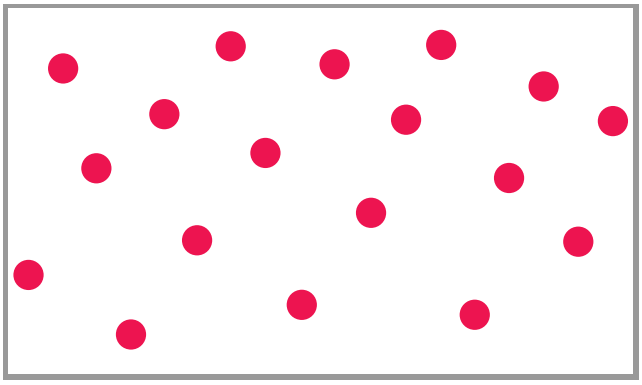

Fig. 3. Video sequence "Red balls".

Reference video sequences presented in Table 1 were created by using Macromedia Flash Professional application and in the next step they were encoded in VirtualDub tool. The main aim of tests done in scope of this work was to verify impact of various network conditions in IP network on the quality. Based on video transmission properties the following parameters were chosen:

- jitter of delay [ms],
- packet loss [%],
- packet corrupt [%].

In objective tests quality metric was Mean Square Error (MSE). It was chosen because from the simplest measures this one best fits to distortions in the video pictures that are caused by network changes. For subjective tests standard MOS factor was used in standard 5th-stage and for measurements purposes Double-Stimulus Impairment Scale (DSIS) method was used [8]. Observers were 34 students (17 laboratory groups). To increase results reliability, they were trained about test procedures, used metrics, tools, etc. In calculation of average value for MOS metric 95% confidence level was chosen. Received results and their analysis allow to determine dependencies between network parameters and chosen quality measures. Presented earlier video

sequences was used as reference probes from which sequences after processing was created. For that purpose the system as shown in Fig. 4 was created.

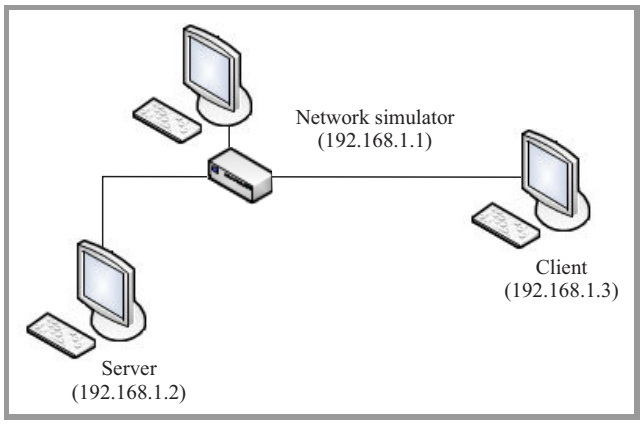

Fig. 4. System created for test probes preparing.

System consist three computers:

- Server (IP: 192.168.1.2) – streaming and sending reference probes to the Client computer,
- Client (IP: 192.168.1.3) – receiving test probes after changes caused by network conditions modification,
- Network Simulator (IP: 192.168.1.1) – modifying network conditions: jitter of delay, packet loss, packet corrupt using NETEM application.

4. Jitter of Delay

Jitter was modified by using NETEM tool. This parameter was changed from 0 to 5 ms with average delay set on 100 ms. Tested measure were MOS and MSE metrics. Figures 5–6 show results for all tested video sequences.

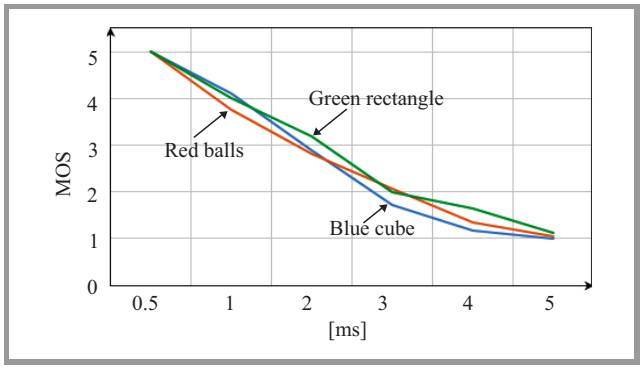

Fig. 5. MOS – jitter of delay (average delay 100 ms).

Tests showed that jitter has significant impact on the perceived quality especially when application buffer is set on small value. The most rushing declines were observed in the range of values from 1 to 3 ms. The charts intentionally omitted confidence intervals to keep it readable. Maximum standard deviations for MSE was 305.2583 where jitter of delay was set on 4 ms (Blue cube sequence). For MOS this statistics parameter gained 0.616945 by 3 ms jitter of delay (Blue cube sequence). Basically most of the distortions in the video pictures were related to blurring or to

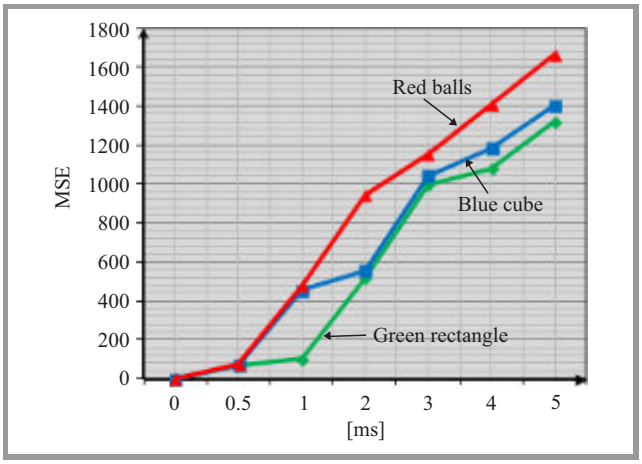

Fig. 6. MSE – jitter of delay (average delay 100 ms).

sharpening effects. Standard deviation for subjective tests was much smaller than in case of standard television sequences [9], but for objective tests results showed no difference. The limit of acceptability for jitter is 1 ms then MOS is above 4.

5. Packet Loss

Percentage of packet loss was modified by using proper mechanisms of NETEM tool from 0 to 10%. Packet were lost random (uniform distribution) without correlation. In this case the following quality metric were used: MOS for subjective (Fig. 7) and MSE for objective measurements (Fig. 8).

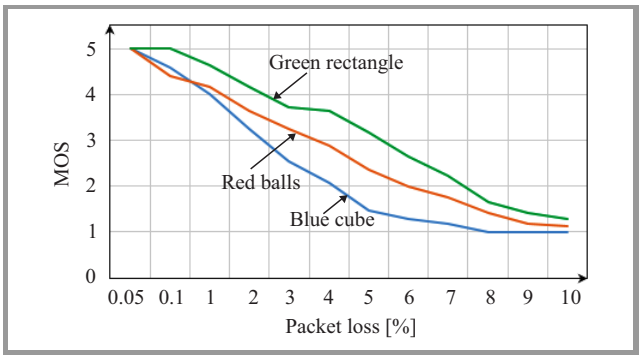

Fig. 7. MOS – packet loss.

Clearly more damaged were high motion videotoms. Degradations was visible from 0.1% value, but they were rare. In this case also to keep charts more readable confidence intervals were omitted. Maximum value of stan-

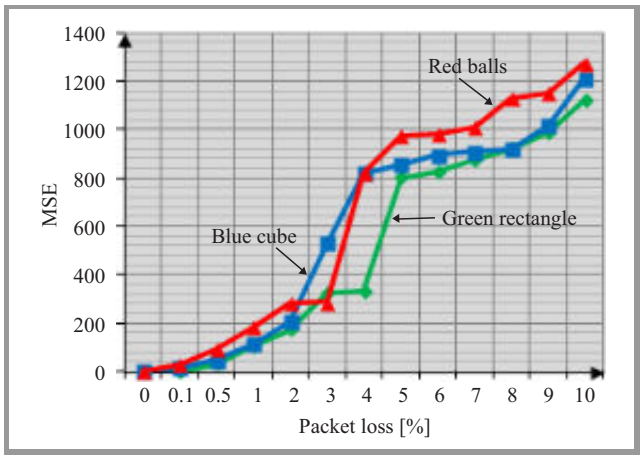

Fig. 8. MSE – packet loss.

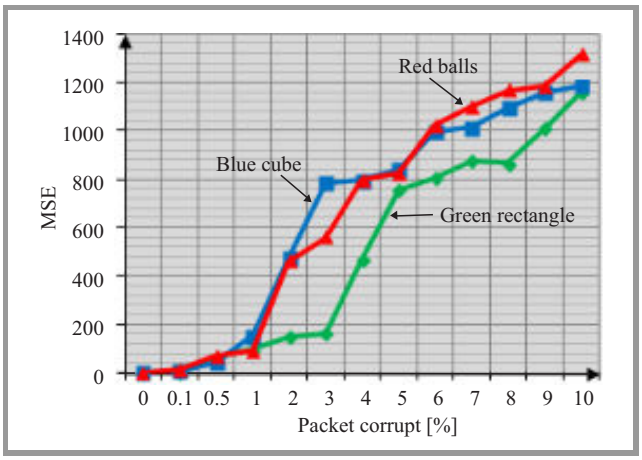

Fig. 10. MSE – packet corrupt.

dard deviation for MOS 0.6960094 occurred when packet loss was set on 4% (Red balls sequence) and for MSE 184.6932 by 6% of packet loss percentage. In this case received results are mainly the same for objective method and much lower than for television sequences for subjective method [9]. The most common distortions are individual artifacts and blurring effects. For larger values of packet loss it is possible to observe freezing effect.

6. Packet Corrupt

Percentage of packet corrupt was modified using NETEM application from 0 to 10%. Packet corrupt was done by introducing bit distortion in the packet body. Distortions were created random (uniform distribution) without any correlation.

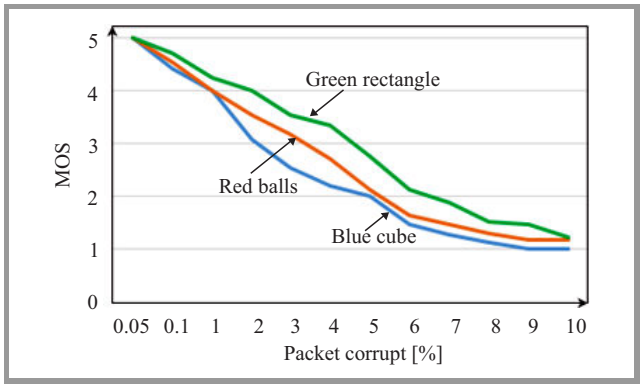

Fig. 9. MOS – packet corrupt.

The most sensitive sequences were Blue cube and Red balls (high motion sequence and sequence with large amount of details – see Figs. 9–10). Video picture deformities for this parameter were mainly the same as for packet loss – artifacts, blurring effects and sharpening effects. In the charter same as earlier confidence intervals were omitted – maximum value of standard deviation for MOS was 0.729981 (Red balls sequence) and for MSE it was 205.9 (Red balls). In comparison to similar tests done for normal television sequences received dispersion of values again are much smaller for subjective tests and mainly the same for objective tests. First distortions were visible when packet loss was set on 0.1%. Tests showed that video quality is acceptable when percentage packet corrupt is not greater than 1% then MOS is still above 4 (Fig. 9).

7. Conclusions

Presented test results showed how network parameters: jitter of delay, packet loss, packet corrupt affect video quality. All of them need to be preserve on proper level in real network in which television services are provided. The most critical parameter was jitter – even small changes in delay variation can have negative impact on quality in received video. Distortions and degradations caused by network parameters are mainly the same and they are associated with artifacts, blurring and sharping effects. Results showed that for objective methods videotoms do not give any special benefits as the results are not much better as for standard television sequences, but for subjective methods they are very useful. Received standard deviations and confidence intervals in each particular case were smaller than for television sequences. Videotoms used instead of television sequences makes it easier to capture distortion in received video pictures. It can reduce costs and effort needed to create quality model for video services.

References

[1] "The E-Model, a computational model for use in transmission planning", ITU-T Rec. G.107, 2005.

[2] Opinion Model for video-telephony applications", ITU-T Rec. G.1070, 2008.

[3] J. Hjelm, *Why IPTV?* Chichester, UK: Willey, 2008.

[4] "Definitions od terms related to quality of service", ITU-T Rec. E.800, 2008.

[5] "Internet protocol data communication service – IP packet transfer and availability performance parameters", ITU-T Rec. Y.1540, 2002.

[6] "Internet protocol data communication service -Quality of service and network performance objectives for IP-based services", ITU-T Rec. Y.1541, 2002.

[7] Network model for evaluating multimedia transmission performance over Internet Protocol, ITU-T Rec. G.1050, 2011.

[8] Parametric non-intrusive assessment of audiovisual media streaming quality, ITU-T Rec. P.1201, 2012.

[9] Ł. Trzcianowski and S. Kula, "Approach to QoS/QoE monitoring and parametric model for IPTV service", *Scient. J. Telecomm. Electron.*, vol. 261, pp. 41–59, 2012.

[10] Subjective video quality assessment for multimedia applications, ITU-T Rec. P.910, 2008.

Łukasz Trzcianowski graduated from the Faculty of Electronics and Information Technology at Warsaw University of Technology (M.Sc., 2012). At present, he continues his work as Ph.D. candidate (Institute of Telecommunications, Warsaw University of Technology). The main focus in his research is given on telecommunication services and parametric models.
Email: ltrzcianowski@tele.pw.edu.pl
Institute of Telecommunication
Warsaw University of Technology
Nowowiejska st. 15/19
00-665 Warsaw, Poland

Paper

Gradient-Based Algorithms in the Brachistochrone Problem Having a Black-Box Represented Mathematical Model

Roman Dębski

Department of Computer Science, AGH University of Science and Technology, Kraków, Poland

Abstract—Trajectory optimization problems with black-box represented objective functions are often solved with the use of some meta-heuristic algorithms. The aim of this paper is to show that gradient-based algorithms, when applied correctly, can be effective for such problems as well. One of the key aspects of successful application is choosing, in the search space, a basis appropriate for the problem. In an experiment to demonstrate this, three simple adaptations of gradient-based algorithms were executed in the forty-dimensional search space to solve the brachistochrone problem having a black-box represented mathematical model. This experiment was repeated for two different bases spanning the search space. The best of the algorithms, despite its very basic implementation, needed only about 100 iterations to find very accurate solutions. 100 iterations means about 2000 objective functional evaluations (simulations). This corresponds to about 20 iterations of a typical evolutionary algorithm, e.g. $ES(\mu,\lambda)$.

Keywords—black-box optimization, brachistochrone problem, optimal control, trajectory optimization.

1. Introduction

The brachistochrone (i.e. the curve of fastest descent) problem was posed by Johann Bernoulli in *Acta Eruditorum* in June 1696. Its original wording was, *"Given two points A and B in a vertical plane, what is the curve traced out by a point acted on only by gravity, which starts at A and reaches B in the shortest time"*. The first who found the solution were: Johann Bernoulli, Johan's brother Jakob, Newton, Leibniz and l'Hôspital [1]. Since then the problem has been studied by mathematicians, physicists and engineers. This is a consequence of the fact that apart form being a classic problem in the calculus of variations it also plays an important role in the trajectory optimization, mainly because some of minimum-time trajectory planning tasks can be reduced to one of generalizations of the brachistochrone problem.

The original problem, which assumes that the particle is falling on a vertical plane in a uniform gravitational field, has an analytical solution, e.g. [2]. So do some of the original problem generalizations – for instance, an introduction of the Coulomb friction force [3]–[6] or the drag force proportional to velocity [5], taking into account a nonuniform gravitational field [7], a motion on surfaces different from a vertical plane [8] or relativistic effects [9]–[11]. Yet many engineering problems (related to trajectory optimization) are too complex to be solved analytically – either by the use of classic calculus of variations methods or, when the problem is put into the optimal control context, the Pontryagin maximum principle [2], [12]–[14]. In such cases other methods have to be used [15]–[19]. At the implementation level, each of these methods is usually based on non-linear programming (the family of gradient/sub-gradient methods [15]), dynamic programming [20] or some meta-heuristics, e.g., evolutionary algorithms, simulated annealing, particle swarm optimization, tabu search.

A special group of trajectory optimization problems consists of those with *black-box represented* objective functions [21], [22]. This is the case, for instance, when values of the objective function (performance measure) are received from simulation. In such situation most of the classic optimization methods cannot be used (at least not directly) and a common practice is to base the optimization process on one of the meta-heuristics[1] [23]–[26]. Although this approach has some drawbacks, e.g. [15], [25], especially when applied to trajectory optimization problems, only a few studies of alternative methods have been carried out, e.g. [27]).

This paper addresses this by showing that gradient-based methods, when applied correctly, can also be effective for trajectory optimization problems having black-box represented mathematical models. An important aspect of the successful application is choosing, in the search space, a basis appropriate for the problem. In an experiment to demonstrate this, three simple adaptations of gradient-based algorithms were executed to solve the brachistochrone problem in search spaces spanned by two different bases. The first one – the natural basis in $\mathbb{R}^n$ – was selected to demonstrate some pitfalls of overly direct application of gradient-based methods to variational problems. This knowledge can be useful both while implementing custom-made trajectory

[1]Because they are usually "derivative-free", i.e. do not use derivatives of the objective function.

optimization software[2] and while using any of the trajectory optimization tools available on the market (MATLAB, OTIS or libraries Trajopt or NTG [28]).

This paper is organized as follows. In Section 2 the optimization problem is presented. Section 3 describes the solution methods proposed – six algorithms derived from non-linear programming. In Section 4 optimization results are discussed. Section 5 contains conclusions of the study. In the last part, which is Appendix, the simulation-based trajectory evaluator used in the experiments is described.

2. Problem Formulation

A black-box optimization occurs when the explicit formula of the objective function (performance measure) is unknown, i.e. it is "opaque" or black-boxed to the optimization routine. A typical example of this situation is when objective function values are taken from a computer simulation. In such problems, derivative-related information is not available and, as a consequence, gradient-based algorithms cannot be applied. What is commonly used instead, is one of the derivative-free (DFO) algorithms (e.g. [22], [27]) or (meta-)heuristics. Another possible approach, which is presented in this paper, is to use approximate values of partial derivatives, e.g. by finite differences in a gradient-based algorithm and, in case of non-convex problems, combine it with a multi-start method.

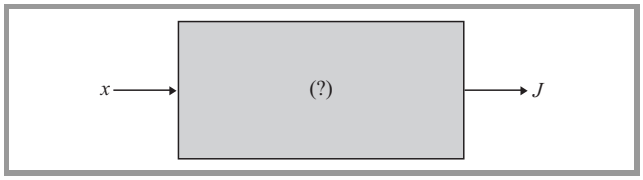

Fig. 1. A black-box functional – the value of J that corresponds to the input can be found only through simulation.

The brachistochrone problem analyzed in this paper covers cases with arbitrarily complex but continuous, black-box represented mathematical models. In this context, the performance measure is expressed by a black-box functional shown in Fig. 1. The input vector $\boldsymbol{x}$ represents a trajectory (encoded in some way) and J – the time of the corresponding displacement. The optimization task is to find x^* corresponding to the minimum value of J, or more formally:

$$\underset{\boldsymbol{x}}{\text{minimize}}\ J(\boldsymbol{x}),\ \text{subject to: } x_0 = A \text{ and } x_{n+1} = B. \qquad (1)$$

A given trajectory represented as a sequence of points

$$(x_0, x_1, \ldots, x_{n+1}) = (P^{(0)}, P^{(1)}, \ldots, P^{(n+1)})$$

in coordinate system $\xi_1 - \xi_2$ is shown in Fig. 2.

[2]It can be necessary e.g. because of some missing functionality in the available tools, their license constrains or the target platform limitations.

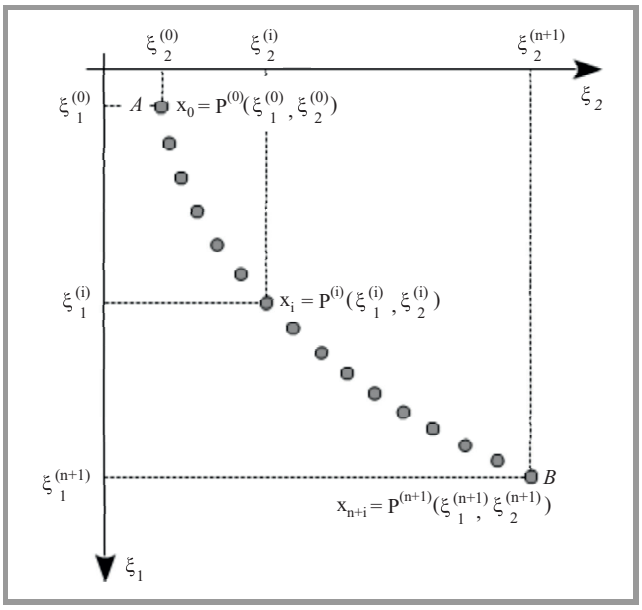

Fig. 2. Trajectory representation.

Note that this representation does not assume anything about the shape of trajectory segments, i.e. $\overset{\frown}{P^{(i-1)}P^{(i)}}, i = 1, \ldots, n+1$.

3. Solution Methods

The optimization algorithms presented in this section are simulation-based. The simulation is represented by function Evaluate, which is shown as Algorithm 1. This function is referenced in the algorithms' pseudo-code.

Algorithm 1 Trajectory evaluation

```
1: function Evaluate(ξ)
2:     //...evaluate (through simulation) ξ, i.e. calc. J(ξ)
3:     return J(ξ)
4: end function
```

The optimization process was based on a series of evaluations of subsequent (admissible) trajectories represented as a series of points (Fig. 2)

$$\boldsymbol{\xi} = \left(\left(\xi_1^{(0)}, \xi_2^{(0)}\right), \left(\xi_1^{(1)}, \xi_2^{(1)}\right), \ldots, \left(\xi_1^{(n+1)}, \xi_2^{(n+1)}\right)\right)^{\top}, \qquad (2)$$

where

$$\left(\xi_1^{(0)}, \xi_2^{(0)}\right) = A\left(\xi_{1A}, \xi_{2A}\right) \qquad (3)$$

and

$$\left(\xi_1^{(n+1)}, \xi_2^{(n+1)}\right) = B\left(\xi_{1B}, \xi_{2B}\right). \qquad (4)$$

The optimization assumed that only ξ_2 components were variated (perturbed) and ξ_1 were fixed in the following regular mesh

$$\xi_1^{(i)} = \xi_{1A} + i\,\frac{\xi_{1B} - \xi_{1A}}{n+1}, \quad i = 0, 1, \ldots, n+1. \qquad (5)$$

Taking into account the boundary conditions and Eqs. 3–4, only points with indexes $1 \ldots n$ were variated (see also Figs. 3–4).

The algorithms discussed in the next subsections contain references to the following symbols:

$\boldsymbol{\xi_0}$ – initial guess trajectory, $\boldsymbol{\xi_0} = \boldsymbol{\xi_{20}} = \left(\xi_2^{(1)}, \ldots, \xi_2^{(n)}\right)^\top$,

e – step size multiplier (assumed to be constant),

δ_0 – stop condition parameter.

In all these algorithms a finite difference based approximation of partial derivatives and gradients was applied. The approximation formulas will be given in each case separately.

3.1. Algorithms in the Search Space Spanned by the Natural Basis

The natural basis in $\mathbb{R}^n$ is usually the first candidate considered in gradient-based optimization tasks. This basis, put into the trajectory optimization context, is shown in Fig. 3 (note the way of representing a n-dimensional space).

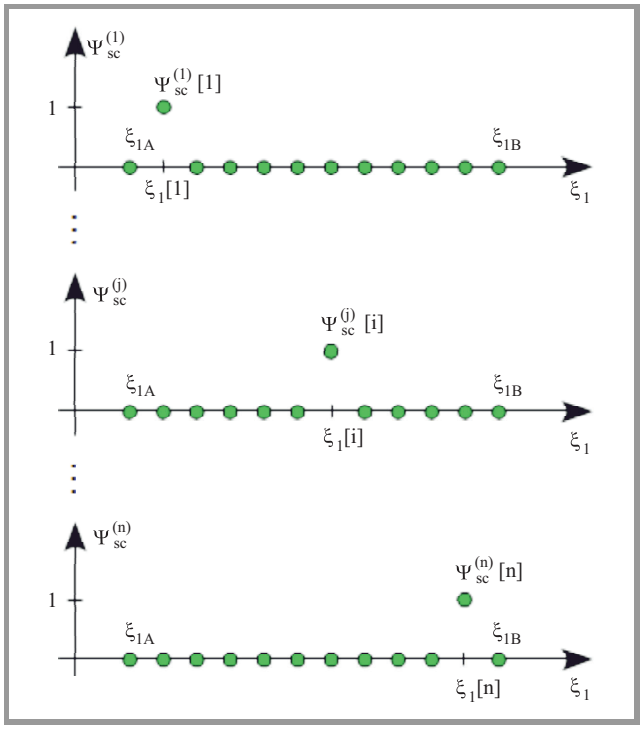

Fig. 3. ψ_{sc}-basis.

In this paper this basis is defined in the following way[3]

$$\left\{\boldsymbol{\psi}_{sc}^{(j)}, \quad j = 1, \ldots, n\right\}, \tag{6}$$

where

$$\boldsymbol{\psi}_{sc}^{(j)}[i] = \delta_{ij} \quad i, j = 1, \ldots, n \tag{7}$$

and δ_{ij} is the Kronecker delta.

In the next part of this section the algorithms defined in this search space are discussed.

[3]Letters $(.)_{sc}$ in the lower index were taken from **s**ingle **c**omponent.

Algorithm SC-FD-SimpGrad

This algorithm uses a forward finite difference (fd) approximation of directional derivative (in the direction of $\boldsymbol{\psi}_{sc}^{(j)}$), expressed in the following way

$$\Delta_{\boldsymbol{\psi}_{sc}^{(j)}}^{(fd)} J = \frac{J\left(\boldsymbol{\xi_2} + \varepsilon \boldsymbol{\psi}_{sc}^{(j)}\right) - J(\boldsymbol{\xi_2})}{\varepsilon}, \quad j = 1, \ldots, n. \tag{8}$$

Having defined the formula for directional derivatives can be calculated the approximation of the gradient vector

$$\hat{\boldsymbol{\nabla}}_{\boldsymbol{\psi}_{sc}}^{(fd)} J = \left(\Delta_{\boldsymbol{\psi}_{sc}^{(1)}}^{(fd)} J, \ldots, \Delta_{\boldsymbol{\psi}_{sc}^{(j)}}^{(fd)} J, \ldots, \Delta_{\boldsymbol{\psi}_{sc}^{(n)}}^{(fd)} J\right)^\top. \tag{9}$$

The algorithm pseudo-code, shown as Algorithm 2, is divided into two parts, with function Grad-Approx being a helper method used to calculate the approximation of the gradient vector.

Algorithm 2 Forward difference based (simple) gradient descent (ψ_{sc}-Basis)

function Grad-Approx($\boldsymbol{\xi}, J_\xi$)
  for $j \leftarrow 1, n$ **do**
    $J_{\xi+\varepsilon} \leftarrow$ Evaluate($\boldsymbol{\xi} + \varepsilon \boldsymbol{\psi}_{sc}^{(j)}$)
    $\hat{\boldsymbol{\nabla}}_{\boldsymbol{\psi}_{sc}}^{(fd)} J[j] \leftarrow \frac{J_{\xi+\varepsilon} - J_\xi}{\varepsilon}$ ▷ see Eq. (8)
  end for
  return $\hat{\boldsymbol{\nabla}}_{\boldsymbol{\psi}_{sc}}^{(fd)} J$
end function

function SC-FD-SimpGrad($\boldsymbol{\xi_0}, e, \delta_0$)
  $J_0 \leftarrow$ Evaluate($\boldsymbol{\xi_0}$)
  $\hat{\boldsymbol{g}}_{\boldsymbol{0}} \leftarrow$ Grad-Approx($\boldsymbol{\xi_0}, J_0$)
  while *true* **do**
    $\boldsymbol{h_0} = -\hat{\boldsymbol{g}}_{\boldsymbol{0}}$
    $\boldsymbol{\xi_1} \leftarrow \boldsymbol{\xi_0} + e\, \boldsymbol{h_0}$
    $J_1 \leftarrow$ Evaluate($\boldsymbol{\xi_1}$)
    $\hat{\boldsymbol{g}}_{\boldsymbol{1}} \leftarrow$ Grad-Approx($\boldsymbol{\xi_1}, J_1$)
    if $J_1 > J_0$ **then** ▷ check stop conditions
      return $(\boldsymbol{\xi_0}, J_0)$
    else if $\frac{|J_0 - J_1|}{J_0} < \delta_0$ **then**
      return $(\boldsymbol{\xi_1}, J_1)$
    end if
    $\boldsymbol{\xi_0} \leftarrow \boldsymbol{\xi_1}$
    $J_0 \leftarrow J_1$
    $\hat{\boldsymbol{g}}_{\boldsymbol{0}} \leftarrow \hat{\boldsymbol{g}}_{\boldsymbol{1}}$
  end while
end function

The algorithm performs $(k+1)(n+1)$ simulations and uses $\Theta(n)$ memory, where k is the total number of iterations in the main optimization routine, and n is the size of the vector representing a trajectory.

Algorithm SC-CD-SimpGrad

This algorithm uses a central finite difference (cd) approximation of directional derivative (in the direction of $\boldsymbol{\psi}_{sc}^{(j)}$), expressed in the following way

$$\Delta_{\boldsymbol{\psi}_{sc}^{(j)}}^{(cd)} J = \frac{J\left(\boldsymbol{\xi}_2 + \varepsilon \boldsymbol{\psi}_{sc}^{(j)}\right) - J\left(\boldsymbol{\xi}_2 - \varepsilon \boldsymbol{\psi}_{sc}^{(j)}\right)}{2\varepsilon}, \quad j = 1, \ldots, n. \tag{10}$$

The approximation of the gradient vector is equal to

$$\hat{\boldsymbol{\nabla}}_{\boldsymbol{\psi}_{sc}}^{(cd)} J = \left(\Delta_{\boldsymbol{\psi}_{sc}^{(1)}}^{(cd)} J, \ldots, \Delta_{\boldsymbol{\psi}_{sc}^{(j)}}^{(cd)} J, \ldots, \Delta_{\boldsymbol{\psi}_{sc}^{(n)}}^{(cd)} J\right)^{\top}. \tag{11}$$

The algorithm pseudo-code, shown as Algorithm 3, is again divided into two parts. The main optimization routine is the same as in Algorithm 2, so is not repeated here.

Algorithm 3 Central difference based (simple) gradient descent (ψ_{sc}-Basis)

```
function Grad-Approx(ξ)
    for j ← 1,n do
        J_{ξ+ε} ← Evaluate(ξ + ε ψ_sc^(j))
        J_{ξ−ε} ← Evaluate(ξ − ε ψ_sc^(j))
        ∇̂^(cd)_{ψ_sc} J[j] ← (J_{ξ+ε} − J_{ξ−ε}) / (2ε)        ▷ see Eq. (10)
    end for
    return ∇̂^(cd)_{ψ_sc} J
end function

function SC-CD-SimpGrad(ξ_0, e, δ_0)
    //...                                                    ▷ see Algorithm 2
end function
```

This algorithm performs $(k+1)(2n+1)$ simulations and uses $\Theta(n)$ memory, where k and n are defined in the same way as in Algorithm 2.

3.2. Algorithms in the Search Space Spanned by the Modified Basis

The basis introduced in this section is more complex and non-orthogonal. It was chosen as an example of a non-standard basis. Its definition[4] is as follows (see Fig. 4, note the way of representing an n-dimensional space)

$$\left\{\boldsymbol{\psi}_{mc}^{(j)}, j = 1, \ldots, n\right\}, \tag{12}$$

where

$$\boldsymbol{\psi}_{mc}^{(j)}[i] = \begin{cases} \frac{\xi_1[i] - \xi_{1A}}{\xi_1[j] - \xi_{1A}}, & 1 \le i \le j, \\ \frac{\xi_{1B} - \xi_1[i]}{\xi_{1B} - \xi_1[j]}, & j < i \le n. \end{cases} \tag{13}$$

In the next paragraphs the algorithms defined in the search space spanned by $\boldsymbol{\psi}_{mc}$ basis are discussed.

[4]Letters $(.)_{mc}$ in the lower index were taken from **m**ulti **c**omponent.

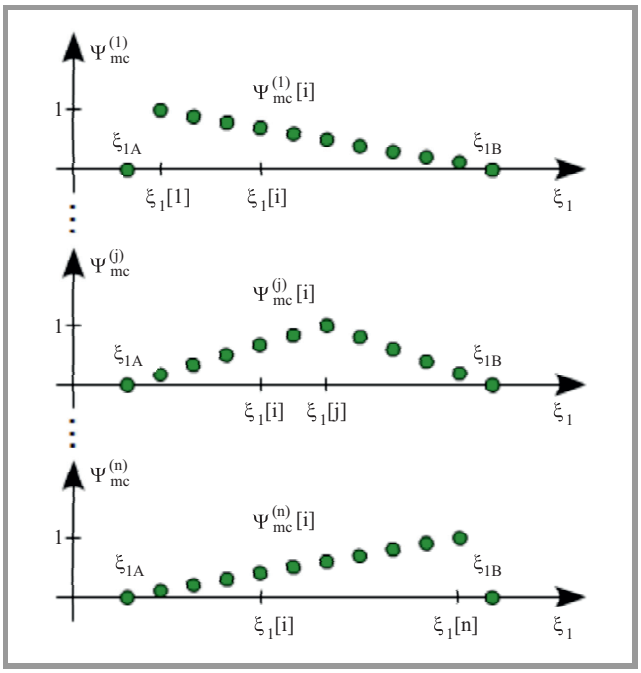

Fig. 4. ψ_{mc}-basis.

Algorithm MC-FD-SimpGrad

In the new basis a forward finite difference (fd) approximation of directional derivative (in the direction of $\boldsymbol{\psi}_{mc}^{(j)}$) is defined as follows

$$\Delta_{\boldsymbol{\psi}_{mc}^{(j)}}^{(fd)} J = \frac{J\left(\boldsymbol{\xi}_2 + \varepsilon \boldsymbol{\psi}_{mc}^{(j)}\right) - J\left(\boldsymbol{\xi}_2\right)}{\varepsilon \|\boldsymbol{\psi}_{mc}^{(j)}\|}, \quad j = 1, \ldots, n, \tag{14}$$

whilst the approximation of the gradient vector is equal to

$$\hat{\boldsymbol{\nabla}}_{\boldsymbol{\psi}_{mc}}^{(fd)} J = \left(\Delta_{\boldsymbol{\psi}_{mc}^{(1)}}^{(fd)} J, \ldots, \Delta_{\boldsymbol{\psi}_{mc}^{(j)}}^{(fd)} J, \ldots, \Delta_{\boldsymbol{\psi}_{mc}^{(n)}}^{(fd)} J\right)^{\top}. \tag{15}$$

Note: $\|.\|$ in the denominator is the L^2-norm.

Algorithm 4 Forward difference based (simple) gradient descent (ψ_{mc}-Basis)

```
function Grad-Approx(ξ, J_ξ)
    for j ← 1,n do
        J_{ξ+ε} ← evaluate(ξ + ε ψ_mc^(j))
        ∇̂^(fd)_{ψ_mc} J[j] ← (J_{ξ+ε} − J_ξ) / (ε ||ψ_mc^(j)||)   ▷ see Eq. (14)
    end for
    return ∇̂^(fd)_{ψ_mc} J
end function

function MC-FD-SimpGrad(ξ_0, e, δ_0)
    //...                                                    ▷ see Algorithm 2
end function
```

MC-FD-SimpGrad algorithm pseudo-code is shown as Algorithm 4 and again, the main optimization routine is the same as in Algorithm 2. This algorithm performs

$(k+1)(n+1)$ simulations and uses $\Theta(n)$ memory, where k and n are defined in the same way as in Algorithm 2.

Central finite difference approximation based algorithms

In the new basis the central finite difference (cd) approximation of directional derivative in the direction of $\psi_{mc}^{(j)}$ can be written as follows:

$$\Delta_{\psi_{mc}^{(j)}}^{(cd)} J = \frac{J\left(\boldsymbol{\xi_2} + \varepsilon \boldsymbol{\psi}_{mc}^{(j)}\right) - J\left(\boldsymbol{\xi_2} - \varepsilon \boldsymbol{\psi}_{mc}^{(j)}\right)}{2\varepsilon \|\boldsymbol{\psi}_{mc}^{(j)}\|}, \quad j = 1, \ldots, n \tag{16}$$

and, as a consequence, the approximation of the gradient vector is equal to

$$\hat{\boldsymbol{\nabla}}_{\psi_{mc}}^{(cd)} J = \left(\Delta_{\psi_{mc}^{(1)}}^{(cd)} J, \ldots, \Delta_{\psi_{mc}^{(j)}}^{(cd)} J, \ldots, \Delta_{\psi_{mc}^{(n)}}^{(cd)} J\right)^{\top}. \tag{17}$$

The above formulas remain the same for the three algorithms presented below.

Algorithm MC-CD-SimpGrad

The algorithm pseudo-code is shown as Algorithm 5 (as before, the main optimization routine is the same as in Algorithm 2). This algorithm performs $(k+1)(2n+1)$ simulations and uses $\Theta(n)$ memory (k and n are defined in the same way as in Algorithm 2).

Algorithm 5 Central difference based (simple) gradient descent (ψ_{mc}-Basis)

```
1: function Grad-Approx(ξ)
2:     for j ← 1,n do
3:         J_{ξ+ε} ← Evaluate(ξ + ε ψ_mc^(j))
4:         J_{ξ−ε} ← Evaluate(ξ − ε ψ_mc^(j))
5:         ∇̂^(cd)_{ψ_mc} J[j] ← (J_{ξ+ε} − J_{ξ−ε}) / (2ε ||ψ_mc^(j)||)   ▷ see Eq. (16)
6:     end for
7:     return ∇̂^(cd)_{ψ_mc} J
8: end function

9: function MC-CD-SimpGrad(ξ_0, e, δ_0)
10:    //...                                                  ▷ see Algorithm 2
11: end function
```

Algorithm MC-CD-SteepDsc

The adaptation of steepest descent algorithm [29] to the brachistochrone problem is shown as Algorithm 6.

This algorithm in each iteration of its main loop performs a minimization along the line

$$\lambda_{min} \leftarrow \underset{\lambda>0}{\operatorname{argmin}} \operatorname{Evaluate}(\boldsymbol{\xi_0} + \lambda \boldsymbol{h_0}) \tag{18}$$

extending from point ξ_0 in the direction of $\boldsymbol{h_0} = -\hat{\boldsymbol{g}}_{\boldsymbol{0}}$ (i.e. minus the local gradient approximate).

Algorithm 6 Central difference based steepest descent (ψ_{mc}-Basis)

```
1: function Grad-Approx(ξ)
2:     //...                                                  ▷ see Algorithm 5
3: end function

4: function MC-CD-SteepDsc(ξ_0, δ_0)
5:     J_0 ← Evaluate(ξ_0)
6:     ĝ_0 ← Grad-Approx(ξ_0)
7:     while true do
8:         h_0 = −ĝ_0
9:         λ_min ← argmin_{λ>0} Evaluate(ξ_0 + λ h_0)
10:        ξ_1 ← ξ_0 + λ_min h_0
11:        J_1 ← Evaluate(ξ_1)
12:        ĝ_1 ← Grad-Approx(ξ_1)
13:        if J_1 > J_0 then                                  ▷ check stop conditions
14:            return (ξ_0, J_0)
15:        else if |J_0 − J_1| / J_0 < δ_0 then
16:            return (ξ_1, J_1)
17:        end if
18:        ξ_0 ← ξ_1
19:        J_0 ← J_1
20:        ĝ_0 ← ĝ_1
21:    end while
22: end function
```

The steepest descent algorithm (see Algorithm 6) performs $(k+1)(2n+1)+l$ simulations and uses $\Theta(n)$ memory, where l is the total number of simulations corresponding to the solution of Eq. (18) and k and n are defined in the same way as in Algorithm 2.

Algorithm MC-CD-ConjGrad

A simple adaptation of the conjugate gradient algorithm [30] to the brachistochrone problem is shown as Algorithm 7. It is one of the most popular and efficient methods in non-linear programming.

The algorithm performs $(1+kn)(1+2n)+l$ simulations and uses $\Theta(n)$ memory, where l, k and n are defined in the same way as in Algorithm 6.

From the simple analysis of Algorithm 7 one can see that the calculation of the approximate gradient is performed at least n times (see the external and internal loops) and therefore this single calculation performs $2n$ simulations. This total number of simulations can seem unexpected, because of the n^2 term, when compared to the previous algorithms, but in the conjugate gradient algorithm k is expected to be very small, often equals 1.

4. Experimental Results

The algorithms discussed in Section 3 were executed using the simulator described in Appendix 1, with combinations of the coefficients μ and k (see Eqs. (20)–(21) in

Algorithm 7 Central difference based conjugated gradient (ψ_{mc}-Basis)

```
1: function Grad-Approx(ξ)
2:     //...                                   ▷ see Algorithm 5
3: end function

4: function MC-CD-ConjGrad(ξ_0, δ_0)           ▷ (see [30])
5:     J_0 ← Evaluate(ξ_0)
6:     ĝ_0 ← Grad-Approx(ξ_0)
7:     while true do
8:         h_0 = −ĝ_0
9:         for j ← 1, n do
10:            λ_min ← argmin_{λ>0} Evaluate(ξ_0 + λ h_0)
11:            ξ_1 ← ξ_0 + λ_min h_0
12:            J_1 ← Evaluate(ξ_1)
13:            ĝ_1 ← Grad-Approx(ξ_1)
14:            if J_1 > J_0 then               ▷ check stop conditions
15:                return (ξ_0, J_0)
16:            else if |J_0 − J_1| / J_0 < δ_0 then
17:                return (ξ_1, J_1)
18:            end if
19:            β ← (ĝ_1 ĝ_1) / (ĝ_0 ĝ_0)
20:            h_1 = −ĝ_1 + β h_0
21:            ξ_0 ← ξ_1
22:            J_0 ← J_1
23:            ĝ_0 ← ĝ_1
24:            h_0 ← h_1
25:        end for
26:    end while
27: end function
```

the Appendix) listed in Table 1. In all cases the initial guess trajectory $\boldsymbol{\xi_0}$ was the straight line between points A and B. The arc AB was approximated by a piecewise-linear function with forty linear segments, so the search space was forty-dimensional. $\xi_1 - \xi_2$ axes were on the surface of the ski slope and the slope angle was assumed to be α. The first experiment setup corresponds to the classic brachistochrone problem. This experiment was performed as a test to check the accuracy of the final solutions obtained from all six algorithms by comparison to the exact solution. These solutions are shown from two perspectives in Figs. 5–6.

Table 1
Experiment setups

Exper. no.	Point A	Point B	α	μ	k
1	(0,0)	(10,10)	15°	**0.00**	**0.00**
2				**0.12**	**0.00**
3				**0.00**	**0.05**
4				**0.12**	**0.05**

Figure 5 shows six trajectories received as a result of the experiment and also, for reference, the straight line AB (as

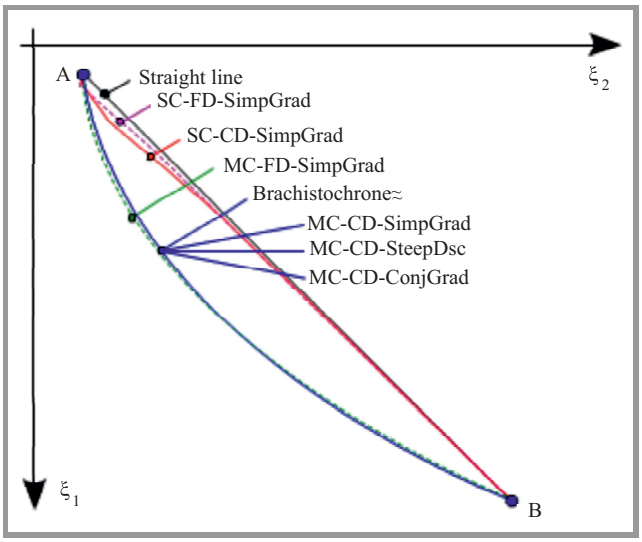

Fig. 5. Simulation results (trajectories) for the classic brachistochrone problem (no friction and no drag, i.e. $\mu = 0.00, k = 0.00$).

the initial guess trajectory, i.e., the start point of each algorithm) and the brachistochrone (i.e. the exact solution). Three results, obtained from MC-CD-SimpGrad, MC-CD-SteepDsc and MC-CD-ConjGrad, were very close to the exact solution. Errors related to the final times were smaller than 0.1% (Fig. 6) and so they are drawn as a single line. On the other hand, the trajectories obtained from SC-FD-SimpGrad and SC-CD-SimpGrad, were very far from the exact solution. The search space for these two algorithms was spanned by $\boldsymbol{\psi}_{sc}$ basis (Fig. 3). These two algorithms will be referenced in this section as sc-algorithms, whilst the other four, defined in the context of ψ_{mc} basis (Fig. 4), as mc-algorithms.

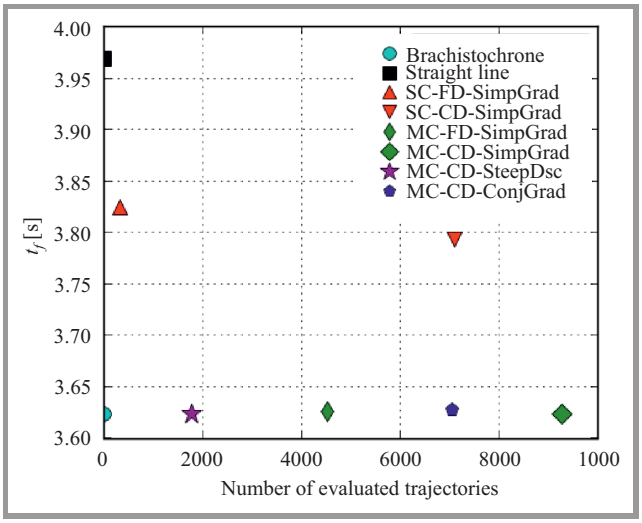

Fig. 6. Simulation results for $\mu = 0.00, k = 0.00$.

Figure 6 shows the experimental results from a different point of view – the algorithms' efficiency and accuracy. Each point represents the final result as a pair of number of evaluated trajectories, and t_f is the final time (to-

tal time of displacement) corresponding to the optimal trajectory. All mc-algorithms performed much better than sc-algorithms. The best of the mc-algorithms was MC-CD-SteepDsc. It needed 1776 evaluations (of different trajectories) to find the solution with the total time of dispacement equal to $t_f = 3.6238$ seconds. The relative error was smaller than 0.01%. MC-CD-ConjGrad performed 7050 evaluations because it did not converge during the first iteration of its external loop as it is often expected to and the algorithm time complexity depends on n^2, see Algorithm 7. Both sc-algorithms performed significantly worse. They were able to improve the initial guess trajectory only by about 3%.

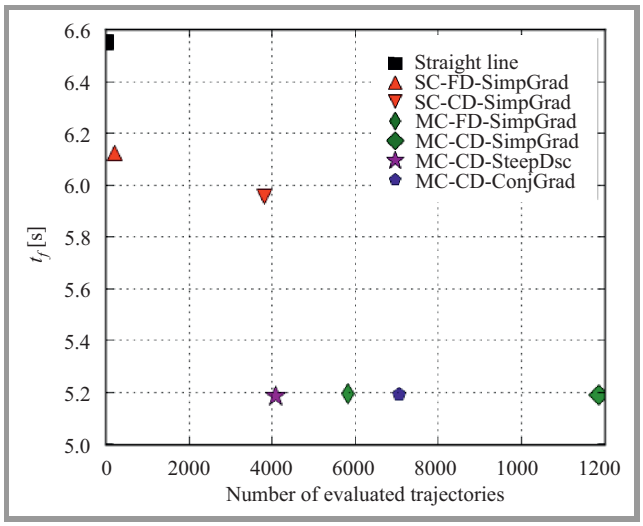

Fig. 7. Simulation results for $\mu = 0.12, k = 0.00$.

Figure 7 presents the results of the second experiment (motion with friction but no drag, i.e. $\mu = 0.12,\ k = 0.00$). Again, the mc-algorithms performed much better than the sc-algorithms and the most efficient was MC-CD-SteepDsc, but this time its advantage was not so significant.

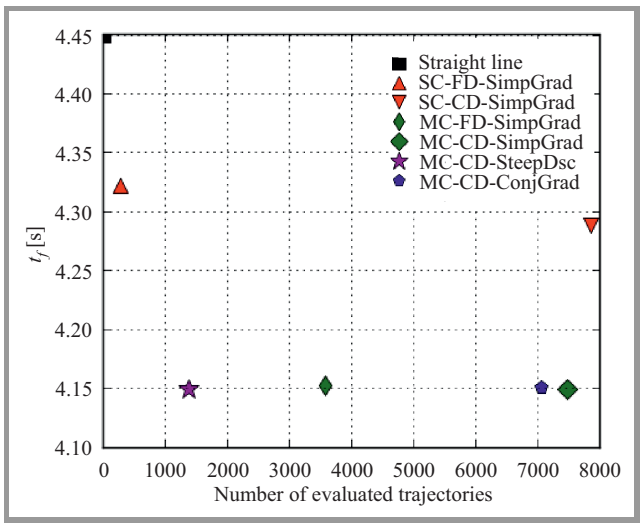

Fig. 8. Simulation results for $\mu = 0.00, k = 0.05$.

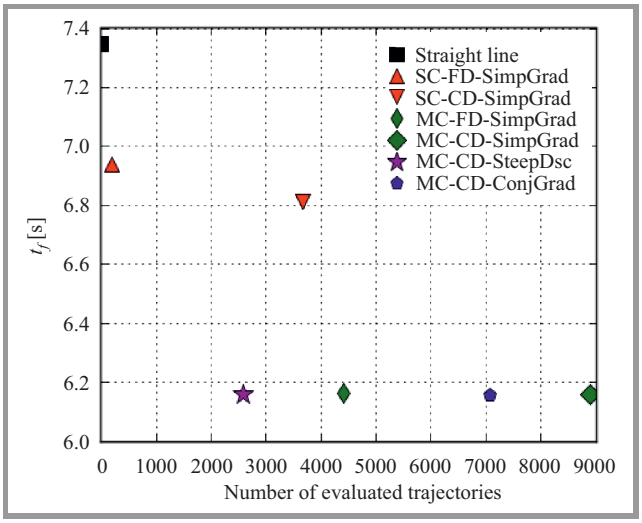

Fig. 9. Simulation results for $\mu = 0.12, k = 0.05$.

Figures 8 and 9 show results from the last two experiments for $\mu = 0.00,\ k = 0.05$ and $\mu = 0.12,\ k = 0.05$. The same pattern can be seen – the most efficient algorithm was again MC-CD-SteepDsc and, in general, the mc-algorithms performed much better than the sc-algorithms.

5. Conclusion

The application of six gradient-based algorithms to the brachistochrone problem having a black-box represented mathematical model has been studied. The main part of this model was a simulation-based trajectory evaluator. As an example of this problem, trajectory optimization in alpine ski racing was chosen.

Each of the six algorithms has been presented in detail (pseudo-code, time and memory complexity). These algorithms were divided into two groups depending on the basis used for spanning their search spaces.

The experimental results have shown that gradient-based algorithms, when applied correctly, can be effective for simulation-based (continuous) trajectory optimization problems. The best of the algorithms, despite its very basic implementation, needed only about 100 iterations corresponding to about 2000 objective function evaluations to find very accurate solutions in a 40-dimensional search space.

Future work could concentrate on experimenting with different bases for the search space. For instance, an orthogonal versus non-orthogonal bases comparison could be carried out. Another area of research could be related to combining the methods presented in this paper with multi-start or memetic algorithms. And finally, the presented algorithms could be verified in an *augmented cloud* environment [31]–[33].

It is worth noting that the presented approach could also be applied to more general variational problems like ”piecewise optimization” of complex trajectories or optimal shape design.

Appendix 1

Simulation-based Trajectory Evaluator (the Black-box Simulator)

Let's consider a skier (modeled as a material point of mass m) going down a slope with angle α from point A to point B. The arc AB is approximated by a piecewise-linear function. This modification simplifies the problem significantly – instead of one (complex) two-dimensional problem, we have a series of (simple) one-dimensional ones. Each of the sub-problems is related to one segment only (Fig.10, note a local coordinate system $\zeta\eta$, set for each segment).

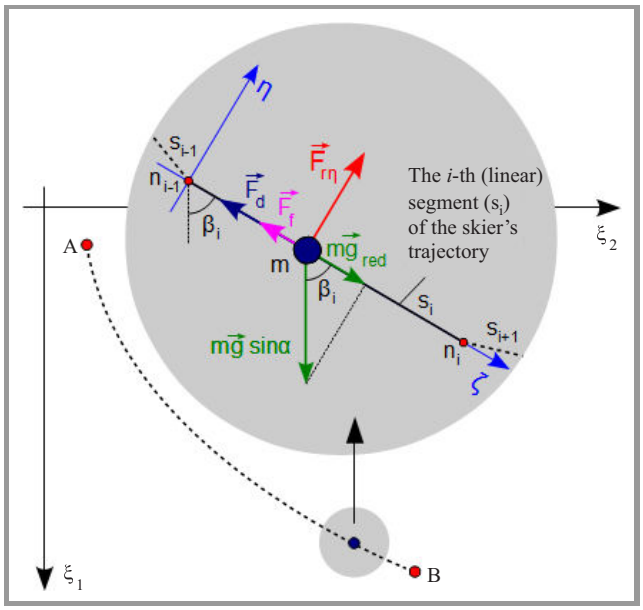

Fig. 10. The forces acting on a skier going down a slope with angle α (one-dimensional approximation model). All forces are reduced to the skier's center of mass and to the surface of the ski slope (i.e. $\xi_1 - \xi_2$).

Equations of motion

The equations of motion for each segment can be written in the following way

$$\begin{cases} m\ddot{\zeta} = mg_{red} - (F_f + F_d) \\ 0 = -F_{r\eta} - mg\sin\alpha\sin\beta \end{cases}, \tag{19}$$

where:

$$F_f = \mu mg\cos\alpha\,, \tag{20}$$

$$F_d = k_1 v^2 = mk\dot{\zeta}^2\,, \tag{21}$$

represent snow resistance (friction) and air resistance (drag), respectively, and

$$g_{red} = g\sin\alpha\cos\beta\,, \tag{22}$$

can be considered as "reduced gravitational acceleration" to the slope plane ($g\sin\alpha$) and to the current linear segment direction ($g\sin\alpha\cos\beta$). Only the first equation is important in the simulation; the second one expresses the condition of equilibrium in the normal direction to the trajectory. After dividing both sides of the first of the Eq. (19) by m and simplifying the expression, for the i^{th} segment we get

$$\ddot{\zeta}_i + k\dot{\zeta}_i^{\,2} = g\,(\sin\alpha\ \cos\beta_i - \mu\cos\alpha)\,. \tag{23}$$

Boundary conditions

The arc $\overset{\frown}{AB}$ is approximated by a piecewise-linear function. We assume that its first segment starts at $A(\xi_{1A}, \xi_{2A})$, and the last one ends at $B(\xi_{1B}, \xi_{2B})$ (Fig. 10). The boundary conditions have to be written now for each segment. An additional assumption has to be introduced into the model – the speed remains constant at the boundary of each pair of subsequent segments, i.e.

$$|\boldsymbol{v}_s^{(i)}| = |\boldsymbol{v}_f^{(i-1)}|, \tag{24}$$

where $\boldsymbol{v}_s^{(i)}$ is the initial speed for the $(i)^{\text{th}}$ segment, and $\boldsymbol{v}_f^{(i-1)}$ is the final speed for the $(i-1)^{\text{th}}$ segment.

Performance measure

In order to find the total time of displacement a series of simulations (one for each segment – s) has to be performed

$$J = t_f = \sum_s t_f^{(s)}. \tag{25}$$

References

[1] J. Babb and J. Currie, "The brachistochrone problem: Mathematics for a broad audience via a large context problem", *The Montana Mathem. Enthus.*, vol. 5, pp. 169–184, 2008.

[2] H. J. Sussmann and J. C. Willems, "300 years of optimal control: from the brachystochrone to the maximum principle", *Control Sys., IEEE*, vol. 17, no. 3, pp. 32–44, 1997.

[3] N. Ashby, W. E. Brittin, W. F. Love, and W. Wyss, "Brachistochrone with coulomb friction", *American J. Phys.*, vol. 43, p. 902, 1975.

[4] J. C. Hayen, "Brachistochrone with coulomb friction", *Int. J. Non-Linear Mechan.*, vol. 40, no. 8, pp. 1057–1075, 2005.

[5] A. S. Parnovsky, "Some generalisations of brachistochrone problem", *Acta Phys. Polonica – Ser. A Gen. Phys.*, vol. 93, pp. 55–64, 1998.

[6] A. M. A. Van der Heijden and J. D. Diepstraten, "On the brachystochrone with dry friction", *In. J. Non-Linear Mechan.*, vol. 10, no. 2, pp. 97–112, 1975.

[7] J. Gemmer, R. Umble, and M. Nolan, "Generalizations of the brachistochrone problem", *arXiv preprint math-ph/0612052*, 2006.

[8] V. Čović and M. Vesković, "Brachistochrone on a surface with coulomb friction", *Int. J. Non-Linear Mechan.*, vol. 43, no. 5, pp. 437–450, 2008.

[9] C. Farina, "Bernoulli's method for relativistic brachistochrones", *J. Phys. A: Mathem. and General*, vol. 20, no. 2, pp. L57–59, 1987.

[10] H. F. Goldstein and C. M. Bender, "Relativistic brachistochrone", *J. Mathem. Phys.*, vol. 27, p. 507, 1986.

[11] G. Mingari Scarpello and D. Ritelli, "Relativistic brachistochrones under electric or gravitational uniform fields", *ZAMM-J. Appl. Mathem. and Mechanics/Zeitschrift für Angewandte Mathematik und Mechanik*, vol. 86, no. 9, pp. 736–743, 2006.

[12] S. M. LaValle, *Planning Algorithms*. Cambridge, U.K: Cambridge University Press, 2006 [Online]. Available: http://planning.cs.uiuc.edu/

[13] L. S. Pontryagin, V. G. Boltyanskii, R. V. Gamkrelidze, and E. F. Mischenko, *The Mathematical Theory of Optimal Processes*. New York-London: Wiley, 1962.

[14] H. J. Sussmann and J. C. Willems, "The brachistochrone problem and modern control theory", in *Contemporary Trends in Nonlinear Geometric Control Theory and its Applications*, A. Anzaldo-Meneses, B. Bonnard, J.-P. Gauthier, and F. Monroy-Perez, Eds. Singapore: World Scientific Publishers, 2002, pp. 113–165.

[15] J. T. Betts, "Survey of numerical methods for trajectory optimization", *J. Guidance Contr. Dynam.*, vol. 21, no. 2, pp. 193–207, 1998.

[16] W. A. Golfetto and S. da Silva Fernandes, "A review of gradient algorithms for numerical computation of optimal trajectories", *J. Aerosp. Technol. Manag.*, vol. 4, no. 2, pp. 131–143, 2012.

[17] A. Jameson and J. Vassberg, "Studies of alternate numerical optimization methods applied to the brachistochrone problem", in *Proc. OptiCON '99 Conf.*, Newport Beach, CA, USA, pp. 281–296, 1999.

[18] E. Olvovsky, "Novel gradient-type optimization algorithms for extremely large-scale nonsmooth convex optimization", PhD thesis, Technion-Israel Institute of Technology, 2005.

[19] A. V. Rao, "A survey of numerical methods for optimal control", *Adv. Astronaut. Sci.*, vol. 135, no. 1, pp. 497–528, 2009.

[20] R. Bellman, "The theory of dynamic programming", Tech. rep., DTIC Document, 1954.

[21] P. Pošik and W. Huyer, "Restarted local search algorithms for continuous black box optimization", *Evolut. Comput.*, vol. 20, no. 4, pp. 575–607, 2012.

[22] P. Pošik, W. Huyer, and L. Pál, "A comparison of global search algorithms for continuous black box optimization", *Evolut. Comput.*, vol. 20, no. 4, pp. 1–32, 2012.

[23] M. Ceriotti and M. Vasile, "MGA trajectory planning with an ACO-inspired algorithm", *Acta Astronautica*, vol. 67, no. 9–10, pp. 1202–1217, 2010.

[24] M. Vasile and M. Locatelli, "A hybrid multiagent approach for global trajectory optimization", *J. Global Optimiz.*, vol. 44, no. 4, pp. 461–479, 2009.

[25] M. Vasile, L. Summerer, and P. De Pascale, "Design of earth–mars transfer trajectories using evolutionary-branching technique", *Acta Astronaut.*, vol. 56, no. 8, pp. 705–720, 2005.

[26] N. Yokoyama, "Trajectory optimization of space plane using genetic algorithm combined with gradient method", in *Proc. 23rd Int. Congr. Aerospace Sciences*, Toronto, Canada, 2002.

[27] D. R. Jones, M. Schonlau, and W. J. Welch, "Efficient global optimization of expensive black-box functions", *J. Global Optimiz.*, vol. 13, no. 4, pp. 455–492, 1998.

[28] M. B. Milam, "Real-time optimal trajectory generation for constrained dynamical systems", PhD thesis, California Institute of Technology, 2003.

[29] A.-L. Cauchy, "Méthode générale pour la résolution des systemes d'équations simultanées", *Comp. Rend. Sci. Paris*, vol. serie A, no. 25, pp. 536–538, 1847.

[30] R. Fletcher and C. M. Reeves, "Function minimization by conjugate gradients", *The Comp. J.*, vol. 7, no. 2, pp. 149–154, 1964.

[31] A. Byrski, R. Dębski, and M. Kisiel-Dorohinicki, "Agent-based computing in an augmented cloud environment", *Comput. Syst. Sci. Eng.*, vol. 21, no. 1, pp. 7–18, 2012.

[32] R. Dębski, A. Byrski, and M. Kisiel-Dorohinicki, "Towards an agent-based augmented cloud", *J. Telecommun. Inform. Technol.*, no. 1, pp. 16–22, 2012.

[33] R. Dębski, T. Krupa, and P. Majewski, ComcuteJS: A web browser based platform for large-scale computations", *Comp. Sci.*, vol. 14, no. 1, pp. 143–152, 2013.

[34] J. Stillwell, "Mathematics and its history", *The Australian Mathem. Soc.*, p. 168, 2002.

[35] G. Galilei, H. Crew, and A. De Salvio, *Dialogues Concerning Two New Sciences*. Charleston: BiblioBazaar, 2010.

Roman Dębski works as an Assistant Professor at the Department of Computer Science at AGH University of Science and Technology. He obtained his M.Sc. in Mechanics (1997) and Computer Science (2002) and Ph.D. specializing in Computational Mechanics (2002). Before joining the University he worked in the IT industry for over 15 years. His current interests include mathematical modeling and computer simulations, parallel processing, heterogeneous computing and trajectory optimization.
E-mail: rdebski@agh.edu.pl
Department of Computer Science
AGH University of Science and Technology
Al. Mickiewicza 30
30-059 Krakow, Poland

Paper

Comparative Study between Several Direction of Arrival Estimation Methods

Youssef Khmou [1], Said Safi [1], and Miloud Frikel [2]

[1] Department of Mathematics and Informatics, Beni Mellal, Morocco
[2] Greyc UMR 6072 CNRS, ENSICAEN, Caen, France

Abstract—In this paper a comparative study, restricted to one-dimensional stationary case, between several Direction of Arrival (DOA) estimation algorithms of narrowband signals is presented. The informative signals are corrupted by an Additive White Gaussian Noise (AWGN), to show the performance of each method by applying directly the algorithms without pre-processing techniques such as forward-backward averaging or spatial smoothing.

Keywords—array processing, Direction of Arrival, geolocalization, propagation, smart antenna, spectral analysis.

1. Introduction

In array signal processing Direction of Arrival estimation (DOA) [1], [2] stands for estimating the angles of arrivals of received signals by an array of antennas. It is considered an important processing step in many sensors systems, i.e., radar, sonar, Measure Electronic Surveillance (MSE), submarine acoustics, geodesic location, optical interferometry, etc.

There are many types of DOA algorithms that have been proposed during the past four decades such as conventional spectral-based, subspace spectral-based and statistical methods. Beamforming techniques [3]–[7] are straightforward and require low computational power but these methods have low resolution [8]. That leads to introduction of subspace-based algorithms [9]–[11] that use the eigendecomposition of output data covariance matrix in order to obtain the so-called signal subspace or noise subspace. However these methods become limited in case of larger number of array sensors, many fast algorithms for DOA have been proposed in recent years such as the propagator method (PM) [12]–[14] without eigendecomposition with low computational load. Unfortunately, this method is only suitable to the presence of white Gaussian noise, and its performance will be degraded in spatial nonuniform colored noise. To overcome this problem, a modified PM algorithm has been proposed with different computation method for the propagation operator [15]. It is only obtained by the partially cross-correlation of array output data which makes it suitable for the case of spatially nonuniform colored noise due to using the off-diagonal elements of array covariance matrix.

This paper presents a comparative study that is restricted to one-dimensional stationary case (azimuth) between several DOA estimation algorithms of narrowband signals [16] that are corrupted by uniform Additive White Gaussian Noise (AWGN). The performance of each method is evaluated by applying directly the algorithms on Uniform Linear Array (ULA) without pre-processing techniques such as forward-backward averaging of the cross correlation of array output data R or spatial smoothing. The authors choose the key factor for this evaluation to be the Signal to Noise Ratio (SNR) of the environment surrounding the ULA and the radiating sources while the number of snapshots constant is maintained.

1.1. Problem Statement

Typical smart antenna architecture of base station can be divided into the following functional blocks as shown in Fig. 1 [16]. Radio signals arriving at the array antennas are conversed from analog to digital form by downconversion and sampling operations, next summation of the digitized signals over all array elements produces single stream output for further processing.

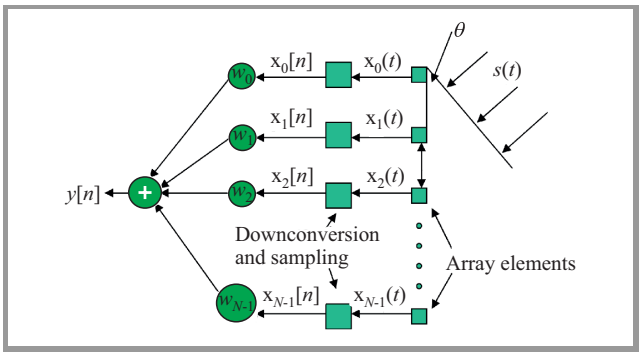

Fig. 1. Typical front-end architecture of base station receiver.

Let's consider an array of N elements receiving P signals such that each element of the array contains zero mean Gaussian noise, the output array is given by:

$$y[t] = \sum_{k=1}^{N} w_k x_k[t], \tag{1}$$

where:

$$x(t) = A(\theta)s(t) + N(t) \tag{2}$$

$x[t] = [x_1(t), \ldots, x_N(t)]^T$, $A(\theta) = [a(\theta_1), \ldots, a(\theta_p)]$ are the received array data and the array manifold matrix respectively, $s(t) = [s_1(t), \ldots, s_p(t)]^T$ and $N(t) = [n_1(t), \ldots, n_N(t)]^T$ stand for the source waveform vector and sensor noise vector, respectively. In Eq. (2)

$$a(\theta_i) = \left[1,\, \mathrm{e}^{\frac{j2\pi d}{\lambda}\sin(\theta_i)}, \ldots, \mathrm{e}^{\frac{j2\pi d(N-1)}{\lambda}\sin(\theta_i)}\right]^T$$

is the steering vector, and d is the distance between elements of the Uniform Linear Array (ULA), λ is the wavelength of the propagating signals, θ_i is the angle of arrival of the i^{th} source and $(.)^T$ denotes the transposition of matrix.

The array signal waveform is considered as stationary process therefore the $N \times N$ correlation matrix can be defined as:

$$R = E\left[(X(t) - m_x(t)).(X(t) - m_x(t))^H\right], \tag{3}$$

where $(.)^H$ denotes the conjugate transposition of matrix.

In this study it is assumed that:

- the signals and the additive Gaussian noise are stationary and ergodic zero mean complex valued random processes,
- the signals sources are not correlated,
- the set of P steering vectors is linearly independent and the P signal sources are statistically independent of each other,
- the number of sources P is known and the number of sensors N satisfies the condition $N \geq 2P+2$.

Under those assumptions the cross correlation matrix is given by:

$$\begin{aligned} R &= E\left[A(\theta)S(t)S^H(t)A^H(\theta)\right] + E\left[(N(t)).N^H(t)\right] \\ &= A(\theta)R_{ss}A^H(\theta) + \sigma^2 I_N, \end{aligned} \tag{4}$$

where $R_{ss} = E\left[S(t)S^H(t)\right]$ is $P \times P$ source signal covariance matrix, σ^2 is the noise variance and I_N stands for an $N \times N$ identity matrix.

In practice, the exact covariance matrix R is unavailable and must be estimated from the received data. The forward-only estimate of covariance matrix is given by:

$$\hat{R}_{xx} = \frac{1}{K}\sum_{k=1}^{K} XX^H. \tag{5}$$

In the Section 2 different algorithms for DOA estimation are presented.

2. DOA Algorithms

2.1. Beamforming Techniques

The beamforming techniques are based on scanning all possible angles in the range $[-\frac{\pi}{2}, \frac{\pi}{2}]$ and measuring the output power of the array such that the power spectrum has peak when the given angle is the direction of arrival of one of the incoming signal. The output signal $y(t)$ is computed using a weight vector w with the received data x:

$$y(t) = w^H x(t). \tag{6}$$

Given N spanshots, the total output power of an array is:

$$\begin{aligned} P(w) = \frac{1}{N}\sum_{n=1}^{N}|y(t_n)|^2 &= \frac{1}{N}\sum_{n=1}^{N} w^H x(t_n)x^H(t_n)w \\ &= w^H \hat{R}_{xx} w. \end{aligned} \tag{7}$$

Based on the Eq. (7) two main techniques have been developed.

2.2. Bartlett Method

Also known as method of averaged periodograms [3], Bartlett method computes the power spectrum as follows. Let $w = a(\theta)$ be the steering vector with arbitrary scanning angle:

$$a(\theta) = \left[1,\, \mathrm{e}^{j\mu}, \ldots, \mathrm{e}^{j(N-1)\mu}\right],$$

$$\mu = \frac{-2\pi f_c}{c} d \sin\theta,$$

where f_c is the carrier frequency of the incoming narrowband signals, c is the speed propagation of the wave signals and d stands for distance between array sensors.

The weight vector is normalized as the following:

$$w = \frac{a(\theta)}{\sqrt{a^H(\theta)a(\theta)}}, \tag{8}$$

and the spatial spectrum is then given by:

$$P(\theta) = P_{bart}(\theta) = \frac{a^H(\theta)\hat{R}_{xx}a(\theta)}{a^H(\theta)a(\theta)}. \tag{9}$$

The weight vector w can be considered as spatial filter, which has been matched to the incoming signal, the array weighting equalizes the delays experienced by the signal on various sensors to combine their respective contributions.

2.3. Capon Beamformer

Capon beamformer is an enhanced version of the Bartlett method, when the sources to be located are closer than the beamwidth, The Bartlett method fails in separating the sources, for this purpose Capon in [4] proposed the maximum likelihood method to solve the for Minimum Variance

Distortion Response (MVDR) of an array such that it maximizes the signal to interference ratio:

$$\min\left(P(w)\right) \qquad \text{subject to} \qquad w^H a(\theta) = 1\,.$$

The resulting weight vector is given by:

$$w = w_{Capon} = \frac{\hat{R}_{xx}^{-1} a(\theta)}{a^H(\theta)\hat{R}_{xx}^{-1} a(\theta)} \tag{10}$$

Replacing the weight vector w in the Eq. (7) yields to the power spectrum:

$$P(\theta) = P_{Capon}(\theta) = \frac{1}{a^H(\theta)\hat{R}_{xx}^{-1} a(\theta)}\,. \tag{11}$$

2.4. Linear Prediction

The linear prediction method [5] is widely used in spectral analysis and speech processing. It is based on the concept of minimizing the mean output signal power of the array elements subject to constraint that the weight on a selected element in ULA is unity. The array weight vector is given by:

$$w = \frac{\hat{R}_{xx}^{-1} u}{u^H \hat{R}_{xx}^{-1} u}\,,$$

where u is the m^{th} column vector of the identity matrix I_{NxN} such that the index m represents the m^{th} element of the ULA. No optimized criterion is proposed for the choice of this element.

The power spectrum can be computed as:

$$P(\theta) = P_{LP}(\theta) = \frac{u^H \hat{R}_{xx}^{-1} u}{|u^H \hat{R}_{xx}^{-1} a(\theta)|^2}\,. \tag{12}$$

The choice of the m^{th} element affects the resolution capability of this method which is dependent on the SNR, and the minimum angle separating the sources.

2.5. Maximum Entropy

Maximum entropy technique [9] is an improvement of the beamforming approach, based on extrapolation the covariance matrix. The extrapolation should be selected with maximized signal entropy where its maximum is achieved by searching for the coefficients of an auto-regressive (AR) model that minimize the expected prediction error:

$$a = \arg\min\left\{a^H \hat{R}_{xx}\right\},$$

subject to the constraint that the first AR coefficient satisfies $a^H e_1 = 1$ where $a = [a_1, a_2, \ldots, a_N]^T$ and e_1 is the first column of the identity matrix I_N. Applying the Lagrange multiplier technique yields to

$$a = \frac{\hat{R}_{xx}^{-1} e_1}{e_1^T \hat{R}_{xx}^{-1} e_1}\,.$$

Next the spatial spectrum can be computed as

$$P(\theta) = P_{ME}(\theta) = \frac{1}{|a(\theta)^H C_j|^2}\,, \tag{13}$$

where C_j represents the j^{th} column of the inverse cross correlation matrix $\hat{R}_{xx}^{-1}$.

The quality of the resolution of the maximum entropy method depends on the choice of column C_j.

2.6. Pisarenko Harmonic Decomposition

Pisarenko harmonic decomposition method [9] minimizes the Mean Square Error (MSE) of the array output under the constraint that the norm weight vector to be equal to unity. The eigenvector that minimizes the MSE corresponds to the smallest eigenvalue of the cross-correlation of array output data, the output power is given by:

$$P(\theta) = P_{PHD}(\theta) = \frac{1}{|a(\theta)^H \bar{e}_1|^2}\,, \tag{14}$$

where $\bar{e}_1$ is the eigenvector associated with the smallest eigenvalue σ_1.

2.7. Minimum Norm

The minimum norm technique [1], [9] is generally considered to be a high-resolution method which assumes a ULA structure.

The algorithm is described as the following. After estimating the cross correlation matrix $\hat{R}_{xx}$, a Singular Value Decomposition (SVD) is performed to extract the matrices U, S and V such that $\hat{R}_{xx} = USV'$. Next, a noise subspace is constructed by selecting the set of vectors $E_N = U(:, P+1:N)$ where P and N denotes the number of radiating sources and the number of elements in the ULA respectively. Constructing the spectrum is based on minimum norm vector lying in the noise subspace whose first element equals 1 and having minimum norm, this condition is satisfied by using the first column of the identity matrix $u = [1\ 0\ 0\ \ldots\ 0]^T$ to compute the following spatial spectrum:

$$P_{MN}(\theta) = \frac{1}{|a(\theta) E_N E_N^H u|^2}\,, \tag{15}$$

where $a(\theta)$ is the array steering vector and E_N is the noise subspace with columns representing the eigenvectors $[e_1, e_2, \ldots, , e_{N-P}]$.

2.8. MUSIC Algorithm

Multiple Signal Classification (MUSIC) method [10] is widely used in signal processing applications for estimating and tracking the frequency and emitter location.

This method is considered as a generalization of the Pisarenko's one [9]. It is based on spectral estimation which exploits the orthogonality of the noise subspace with the signal subspace.

Assume that $\hat{R}_{xx}$ is NxN matrix with rank P, therefore it has $N-P$ eigenvectors corresponding to the zeros/smallest eigenvalues in the absence/presence of noise. The eigendecomposition of $\hat{R}_{xx}$ is given by:

$$\hat{R}_{xx} = \sum_{i=1}^{N} \lambda_i q_i q_i^H = Q_s \Delta_s Q_s^H + Q_n \Delta_n Q_n^H \,, \tag{16}$$

where

$$\Delta_s = diag[\lambda_1, \lambda_2, \ldots, \lambda_P] \,,$$

$$\Delta_n = diag[\lambda_{P+1}, \lambda_{P+2}, \ldots, \lambda_N] \,,$$

$$\lambda_1 \geqslant \lambda_2 \geqslant \ldots \geqslant \lambda_P > \lambda_{P+1} = \lambda_{P+2} = \ldots = \sigma_N^2 \,,$$

$Q_s = [q_1, q_2, \ldots, q_P,]$ is the signal subspace corresponding to Δ_s and $Q_n = [q_{P+1}, q_{P+2}, \ldots, q_N]$ is the noise subspace corresponding to Δ_n.
The MUSIC spectrum is given by:

$$P_{MUSIC}(\theta) = \frac{1}{a^H(\theta) Q_n Q_n^H a(\theta)} \,. \tag{17}$$

When scanning the angles in range $[-\frac{\pi}{2}, \frac{\pi}{2}]$, if θ is DOA of one of signals, so $a(\theta) \perp Q_n$ the denominator is identically zero and the spectrum identifies the angle as a peak.

2.9. Propagator Method

Unlike the MUSIC algorithm, the propagator method [12]–[14] is computationally low complex because it does not need eigendecomposition of the covariance matrix, but it uses the whole of it, to obtain the propagation operator. Therefore, this algorithm is only suitable to the presence of white Gaussian noise and its performance will be degraded in spatial non-uniform colored noise. The propagator is constructed as the following. The covariance matrix can defined as:

$$\hat{R}_{xx} = \begin{bmatrix} R_1 & R_2 \end{bmatrix}^T \,,$$

where R_1 and R_2 are PxN, $(N-P)xN$ matrices respectively.

In noiseless system:

$$R_2 = P^H R_1 \,. \tag{18}$$

In noisy environment the least mean squares technique (LMS) is used to estimate P that minimizes the Frobenius norm $||R_2 - P^H R_1||$:

$$P^H = R_2 (R_1^H R_1)^{-1} R_1^H \,. \tag{19}$$

Next, the matrix Q is constructed, such that:

$$Q^H = \begin{bmatrix} P^H & -I_{N-P} \end{bmatrix} \,. \tag{20}$$

The spectrum is given by:

$$P(\theta) = P_{propag}(\theta) = \frac{1}{||Q^H a(\theta)||^2} \,. \tag{21}$$

2.10. Partial Covariance Matrix

Partial covariance matrix technique [15] is an enhanced version of the propagator method, where no eigendecomposition is needed. The different approach for computing the propagation operator is based on using three submatrices of the estimated cross-correlation matrix $\hat{R}_{xx}$. The array manifold matrix can be portioned as:

$$A = \begin{bmatrix} A_1^T, A_2^T, A_3^T \end{bmatrix} \,, \tag{22}$$

where A_i, $i = 1,2,3$ is matrix with dimensions $P \times P$, $P \times P$ and $(N-2P) \times P$ respectively.
The following partial cross-correlation matrices of the array output are defined as :

$$R_{12} = E\left[X(1:P,:)X(P+1:2P,:)^H\right] = A_1 R_{ss} A_2^H \,, \tag{23}$$

$$R_{31} = E\left[X(2P+1:N,:)X(1:P,:)^H\right] = A_3 R_{ss} A_1^H \,, \tag{24}$$

$$R_{32} = E\left[X(2P+1:N,:)X(P+1:2P,:)^H\right] = A_3 R_{ss} A_2^H \,. \tag{25}$$

Based on these sub-matrices, the matrix Q is:

$$Q^H = \begin{bmatrix} R_{32} R_{12}^{-1} & R_{31} R_{21}^{-1} & -2I_{N-2P} \end{bmatrix}$$

Multiplying Q with the steering matrix yields to:

$$Q^H A = 0, Q^H a(\theta_k) = 0 \quad (k = 1,2 \ldots, p) \,. \tag{26}$$

The spectrum is then, similarly to the propagator method, given by:

$$P(\theta) = P_{partial}(\theta) = \frac{1}{||Q^H a(\theta)||^2} \,. \tag{27}$$

3. Simulation Results

A comparative study [17] has been made between 7 algorithms for DOA, using 4 elements and 2 sources with fixed SNR = 10 dB and the 2 sources were separated by $d = 80°$. This study focused on the performance of the algorithms based on the number of snapshots by simulating the first time with L1 = 10 then with L2 = 100 snapshots.
In this paper, real life scenario is simulated by studying the performance of each method based on the noise environment by testing with SNR1 = 1 dB (high noise level) and SNR2 = 20 dB (low noise level). To evaluate the Rayleigh angle resolution limit, for example the second and the third radiating sources were chosen to be separated by 6° while the number of snapshots was fixed.
The authors consider Uniform Linear Array (ULA) composed of $N = 10$ identical sensors with half wavelength inter-element spacing and $P = 4$ almost equally powered emitting sources with carrier frequency $fc = 1$ GHz. The distance between two sensors is $d = 15$ cm so the total distance of the array is 135 cm and $K = 200$ snapshots.
For simulation on evaluating each method the Monte-Carlo method was used such as each result is an average of $L = 100$ runs.

The sources are non-coherent as given by the normalized cross-correlation matrix R_{ss}:

$$R_{ss} = \begin{pmatrix} 1.00 & 0.00 & 0.00 & 0.04 \\ 0.00 & 1.00 & 0.05 & -0.05 \\ 0.00 & 0.05 & 1.00 & 0.08 \\ -0.04 & -0.05 & 0.08 & 1.00 \end{pmatrix}.$$

In Table 1 the configuration of the described sources is presented.

Table 1
Sources characteristics

Sources	S1	S2	S3	S4
DOAS [°]	–24	15	21	70
Power [W]	1.20	1.30	1.44	1.50

Figure 2 shows the results of the Bartlett spectrum, apparently the maximum resolution for this method is more than 6°, which makes inappropriate for this case. In the previous studies [17], the authors show that ideal resolution of this algorithm is 20°.

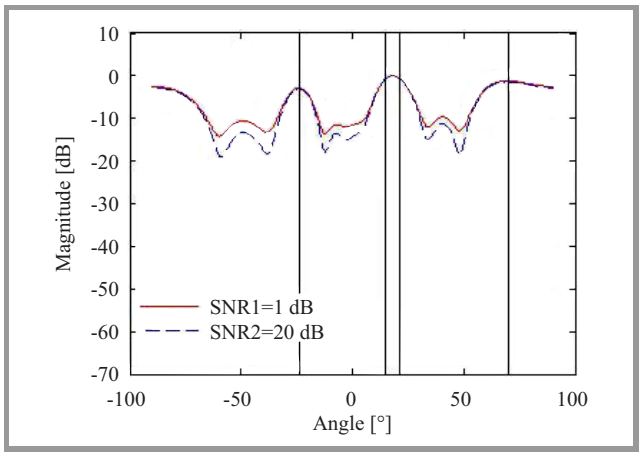

Fig. 2. Bartlett spectrum.

Figure 3 represents the Capon beamformer spectrum which is better performing than the Bartlett method, at SNR = 20 dB the algorithm detects well the sources, but

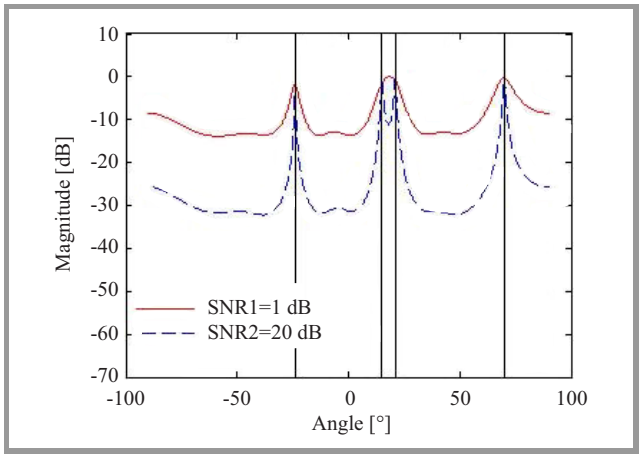

Fig. 3. Capon beamformer spectrum.

in high-level noise it fails to separate the second and the third sources located at (15°, 21°). The numerical tests at SNR = 1 dB showed that the algorithm can separate the sources with minimal difference of 9°.

Figure 4 shows the result of Linear Prediction algorithm, by choosing the fifth element as the vector u, in the Eq. (12), from the identity matrix $I_{10\times10}$

$$u = \begin{bmatrix} 0 & 0 & 0 & 0 & 1 & 0 & 0 & 0 & 0 & 0 \end{bmatrix}^T$$

This algorithms performs better than the two previous techniques, it separates well the closed sources at low SNR.

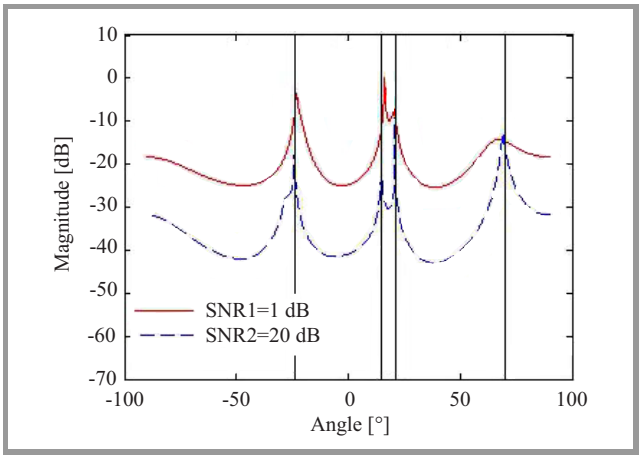

Fig. 4. Linear prediction spectrum.

Figure 5 shows the result of the maximum entropy DOA estimate, by choosing the vector $\bar{C}_j$ as the first column of the inverse cross-correlation matrix $\hat{R}_{xx}^{-1}$ in the Eq. (13).

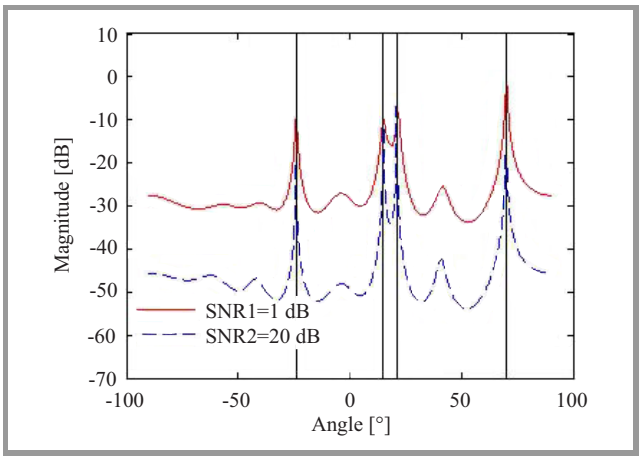

Fig. 5. Maximum entropy spectrum.

This technique performs well by separating the sources at both noise levels which makes it better than Bartlett, Capon and linear prediction methods, however the choice of the column $\bar{C}_j$ influences the performance. As in [17], the j^{th} column was chosen to be in the center of the cross correlation matrix, but in this study the first column was chosen which gives also good results.

In Fig. 6, the application of the Pisarenko harmonic decomposition, at SNR = 20 dB, gives almost the same spectrum

of the maximum entropy method, while at SNR = 1 dB, the spectrum detected well the first source at $-20°$, could not separate the second and the third angles while the last source is detected at 67°, which makes this technique non convenient in low SNR condition.

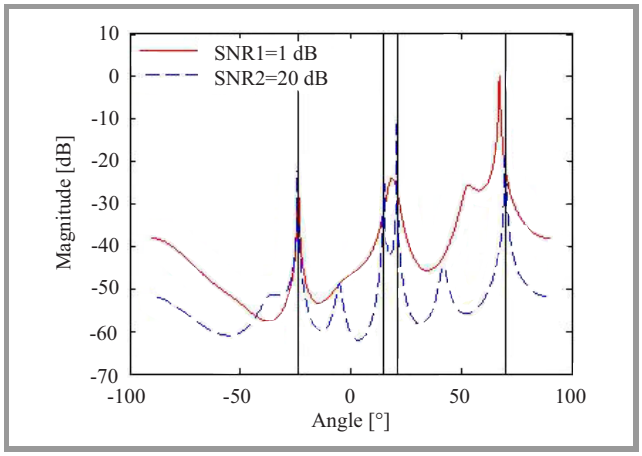

Fig. 6. Pisarenko harmonic decomposition spectrum.

Figure 7 illustrates the minimum norm spectrum which is almost identical with maximum entropy method but with higher number of floating point operations.

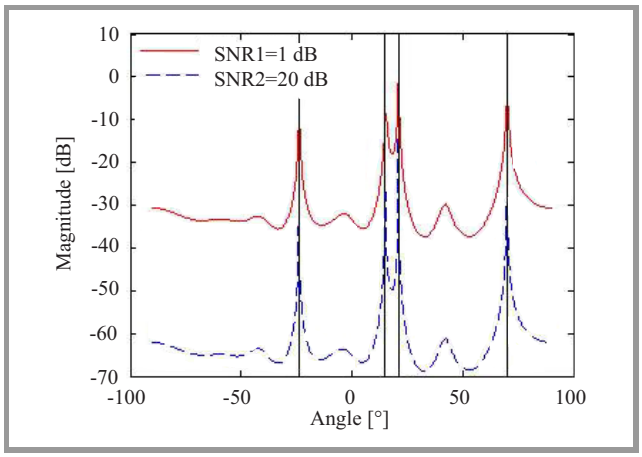

Fig. 7. Minimum norm spectrum.

It should be noted that all the methods are computed using MATLAB and the results are plotted in decibel using the formula

$$P(dB) = 10\log_{10}\left(\frac{spectrum}{Max[spectrum]}\right),$$

to produce a unique frame for comparison [18].

The MUSIC algorithm gives the best result compared to the previous algorithms, as illustrated in Fig. 8, because it detects well all the sources in any noise level and its spectrum does not contain side lobes unlike other techniques.

Note that in high level noise, the spectrum has minimum magnitude of –50 dB while the minimum norm presents a minimum at –60 dB.

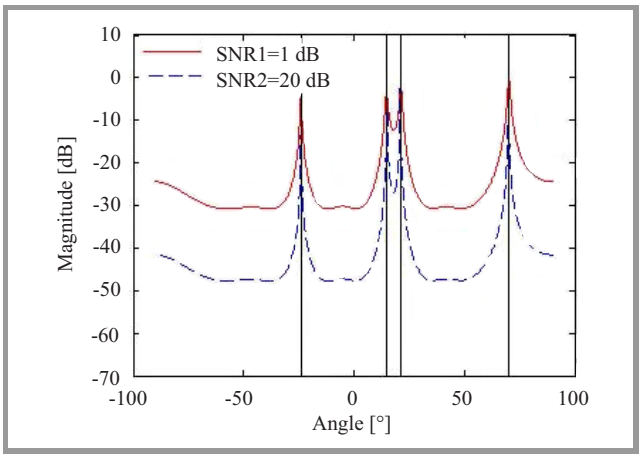

Fig. 8. MUSIC spectrum.

Although, the MUSIC algorithm may fail to resolve the high correlated sources which makes preprocessing techniques like the forward backward averaging or spatial smoothing mandatory to decorrelate the sources.

The propagator method, shown in Fig. 9, has identical performance in both noise levels with minimum apparition of side lobes.

The main advantage of the propagator method is that the constructed matrix Q in Eq. (20) does not need any eigendecomposition, hence the complexity is reduced to $NPK + O(P^3)$ [9].

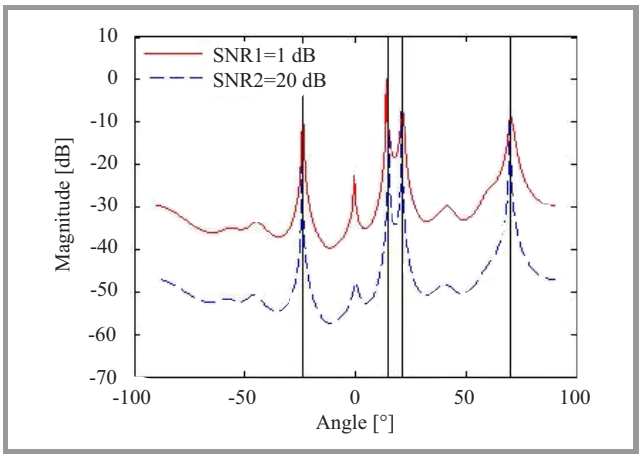

Fig. 9. Propagator spectrum.

Finally, the partial covariance matrix algorithm (without eigendecomposition) is shown in Fig. 10. The results are almost identical with the propagator method, except a noticeable increase in the two side lobes. What makes this technique better than that of the PM method is that the complexity [15] is reduced to $(N-P)PK + O(P^3)$ and takes only partial cross correlation matrices to compute the spectrum. Therefore it is effective in the case of nonuniform colored noise.

The second simulation is based on the average Root Mean Square Error (RMSE) over K = 100 runs between the true DOAs and the nine normalized spectrums, with chrono-

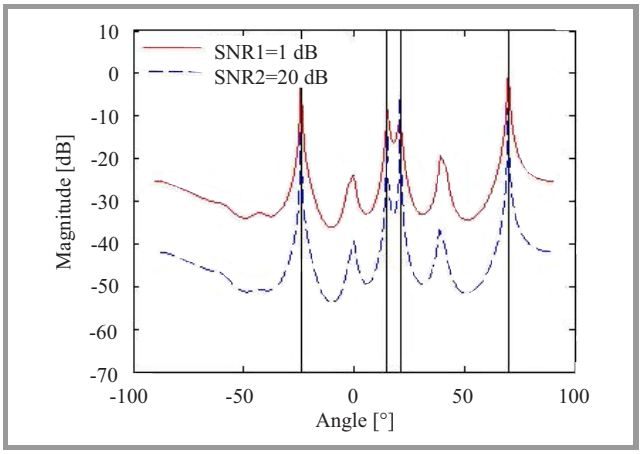

Fig. 10. Partial covariance spectrum.

logical order as described in this paper, computed for two values of SNR:

$$RMSE(\hat{P}(\theta),P(\theta)) = \sqrt{\frac{1}{N}\sum_{n=1}^{N}(\hat{P}(\theta_n)-P(\theta_n))^2}\,.$$

Figures 11–12 represent the RMSE between each method and the true spectrum for SNR = 1 dB and SNR = 20 dB respectively.

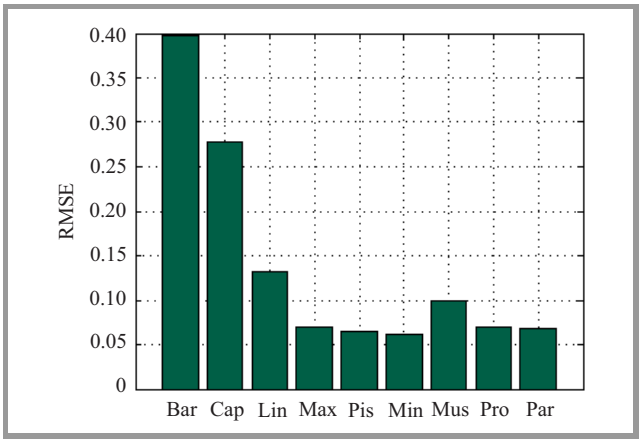

Fig. 11. RMSE, SNR = 1 dB.

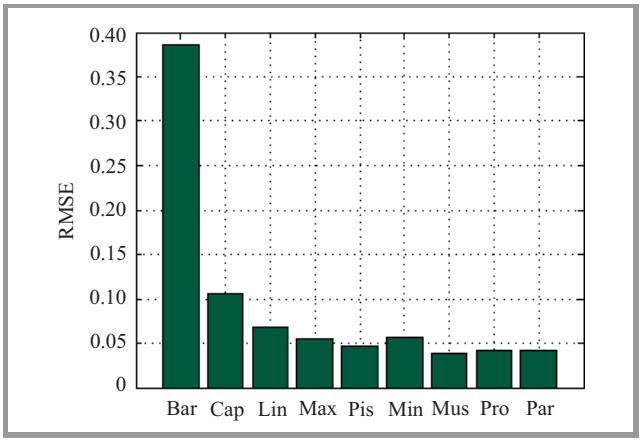

Fig. 12. RMSE SNR = 20 dB.

4. Conclusions

In this paper, some algorithms for one dimensional narrowband direction of arrival (DOA) estimation in stationary case for smart antennas, and for spatially uniform AWGN was compared, starting with the Bartlett method to the recent algorithm which is the partial covariance. In order to evaluate its performance four non-correlated and almost equally powered emitting sources was considered such that two of the sources are separated of 6°, the SNR of 1 dB and 20 dB was the key factor for evaluation. The results showed that in high-level noise, the minimum norm algorithm performs well while in the low-level noise the MUSIC, propagator and partial covariance matrix methods are almost the same and give good results.

In the perspective study, the authors will try to evaluate the partial covariance matrix algorithm in the case of two dimensional wideband sources.

References

[1] Z. Chen, G. Gokeda, and Y. Yu, *Introduction to Direction-of-Arrival Estimation*. Boston, USA: Artech House, 2010.

[2] H. Krim and M. Viberg, "Two decades of array signal processing research", *IEEES Signal Proces. Mag.*, vol. 13, pp. 67–94, 1996.

[3] M. S. Bartlett, "Periodogram analysis and Continuous spectra", Biometrika, vol. 37, no. 1–2, pp. 1–16, 1950.

[4] J. Capon, "High resolution frequency-wave number spectral analysis", *Proc. IEEE*, vol. 57, pp. 1408–1518, 1969.

[5] J. Makhoul, "Linear prediction: A tutorial review", *Proc. IEEE*, vol. 63, no. 4, pp. 561–580, 1975.

[6] W. Min and W. Shunjun, "A time domain beamforming method of UWB pulse array", in *Proc. IEEE In. Radar Conf.*, Arlington, VA, USA, 2005, pp. 697–702.

[7] R. Sanudin *et al.*, "Capon-like DOA estimation algorithm for directional antenna arrays", in *Proc. Loughborough Anten. Propag. Conf. LAPC 2011*, Loughborough, UK, 2011, pp. 1–4.

[8] S. Ejaz and M. A. Shafiq, "Comparison of spectral and subspace algorithms for Fm source estimation", *Progr. Electromag. Res. C*, vol. 14, pp. 11–21, 2010.

[9] L. C. Godora, "Application of antenna arrays to mobile communications. beamforming and direction-of-arrival considerations", *Proc. IEEE*, vol. 85, no. 8, pp. 1195–1245, 1997.

[10] R. O. Schimd, "Multiple emitter location and signal parameter estimation", *IEEE Trans. Anten. Propag.*, vol. 34, no. 3, pp. 276–280, 1086.

[11] J. Xin and A. Sano, "Computationally efficient subspace based method for direction of arrival estimation without eigendecomposition", *IEEE Trans. Sig. Proces.*, vol. 52, no. 4, pp. 876–893, 2004.

[12] J. Munier and G. Y. Delisle, "Spatial analysis using new properties of the cross-spectral matrix", *IEEE Trans. Sig. Proces.*, vol. 39, no. 3, pp. 746–749, 1991.

[13] S. Marcos, A. Marsal, and M. Benidir, "The propagator method for source bearing estimation", *Sig. Proces.*, vol. 42, no. 2, pp. 121–138, 1995.

[14] M. Frikel, "Localization of sources radiating on a large antenna", in *Proc. 13th Eur. Sig. Proces. Conf. EUSIPCO 2005*, Antalya, Turkey, 2005.

[15] J. Chen, Y. Wu, H. Cao, and H. Wang, "Fast algorithm for DOA estimation with partial covariance matrix and without eigendecomposition", *J. Sig. Inform. Proces.*, vol. 2, no. 4, pp. 266–259, 2011.

[16] J. Foutz, A. Spanias, and M. K. Banavar, *Narrowband Direction of Arrival Estimation for Antenna Arrays*. San Rafael, USA: Morgan and Claypool, 2008.

[17] Md. Bakhar, R. M. Vani, and P. V. Hunagund, "Comparative studies of direction of arrival algorithms for smart antenna systems", *World J. Sci. Technol.*, vol. 1, no. 8, pp. 20–25, 2011.

[18] X. WU and T. Guo, "Direction of arrival parametric estimation and simulation based on MATLAB", *J. Comput. Inform. Syst.*, vol. 6, no. 14, pp. 4723–4731, 2010.

[19] Q. Yuan, Q. Chen, and K. Sawaya, "Accurate DOA estimation using array antenna with arbitrary geometry", *IEEE Trans. Anten. Propag.*, vol. 53, no. 4, pp. 1352–1357, 2005.

[20] M. Frikel, B. Targui, S. Safi, and M. M'saad, "Bearing detection of noised wideband sources for geolocation", in *Proc. 18th Mediter. Conf. Control Autom. MED*, Marrakech, Morocco, 2010, pp. 1650–1653.

[21] X. Zhang, Y. Bai, and W. Zhang, "DOA estimation for wideband signals based on arbitrary group delay", in *Proc. World Congr. Engin. Comp. Sci. WCECS 2009*, San Francisco, USA, 2009, vol. 2, pp. 1298–1300.

Youssef Khmou obtained the B.Sc. degree in Physics and M.Sc. degree from poly disciplinary faculty, in 2010 and from Faculty of Science and Technics Beni Mellal, Morocco, in 2012, respectively. Now he is Ph.D. student and his research interests include statistical signal and array processing and statistical physics.

Email: khmou.y@gmail.com
Department of Mathematics and Informatics
Beni Mellal, Morocco

Said Safi received the B.Sc. degree in Physics (option Electronics) from Cadi Ayyad University, Marrakech, Morocco in 1995, M.Sc. degree from Chouaib Doukkali University and Cadi Ayyad Universrsity, in 1997 and 2002, respectively. He has been a Professor of information theory and telecommunication systems at the National School for applied Sciences, Tangier, Morocco, from 2003 to 2005. Since 2006, he is a Professor of applied mathematics and programming at the Faculty of Science and Technics, Beni Mellal, Morocco. In 2008 he received the Ph.D. degree in Telecommunication and Informatics from the Cadi Ayyad University. His general interests span the areas of communications and signal processing, estimation, time-series analysis, and system identification – subjects on which he has published 14 journal papers and more than 60 conference papers. Current research topics focus on transmitter and receiver diversity techniques for single- and multi-user fading communication channels, and wide-band wireless communication systems.

E-mail: safi.said@gmail.com
Department of Mathematics and Informatics
Beni Mellal, Morocco

Miloud Frikel received his Ph.D. degree from the center of mathematics and scientific computation CNRS URA 2053, France, in array processing. Currently, he is with the GREYC laboratory (CNRS URA 6072) and the ENSI-CAEN as Assistant Professor. From 1998 to 2003, Dr. Frikel was with the Signal Processing Lab, Institute for Systems and Robotics, Institute Superior Tecnico, Lisbon, as a researcher in the field of wireless location and statistical array processing, after been a research engineer in a software company in Munich, Germany. He worked in the Institute for Circuit and Signal Processing of the Technical University of Munich. His research interests span several areas, including statistical signal and array processing, cellular geolocation (wireless location), space-time coding, direction finding and source localization, blind channel identification for wireless communication systems, and MC-CDMA systems.

E-mail: mfrikel@greyc.ensicaen.fr
GREYC UMR 6072 CNRS
Ecole Nationale Supérieure d'Ingénieurs
de Caen (ENSICAEN)
6, B. Maréchal Juin" 14050 Caen, France

Paper

Transmit Diversity in the Downlink for the TETRA-TEDS System

Dominik A. Rutkowski[1] and Sławomir Możdżonek

[1] Faculty of Electronics, Telecommunications and Informatics, Gdańsk University of Technology, Gdańsk, Poland

Abstract—In the paper a proposal for the improvement of performance for the TETRA Enhanced Data System (TEDS) employing transmit diversity based on two antennas in the downlink is described. The key idea of the considerations relies on using the space-frequency coding algorithm. The proposal described required some relatively simple changes to the existing TEDS's Single Input Single Output (SISO) interface but the original number of payload and signaling symbols in the normal downlink burst is preserved. The simulation results obtained indicate a significant improvement in performance. The Eb/No parameter could be reduced from 5 to 8 dB with respect to Frame Error Rate (FER), compared to a single antenna transmission for the same FER = 10^{-3}.

Keywords—multiple input multiple output (MIMO), TETRA Enhanced Data System.

1. Introduction

For more than two decades worldwide huge development in mobile digital communication systems with continually improving performance can be observed, increasing throughput and an enlarging pool of services available for users. One of the known techniques employed in this progress is Multiple Input Multiple Output (MIMO) due to its ability to form different routes for the transmission of signals over the radio fading channel.

The TETRA Enhanced Data System (TEDS) [1]–[3] with its radio interface based on filtered multitone modulation (FMT) [4] is suitable for the implementation of MIMO. However, due to the relatively small dimensions of a mobile terminal, the simple version of MIMO – called Multiple Input Single Output (MISO) – is reasonable for TEDS with two transmit antennas at the base station and a single receive antenna at the mobile terminal.

Furthermore, such a MISO technique is simple and does not require significant changes in the radio interface.

2. Implementation of MISO in the TEDS Radio Interface

In the following, the implementation of MISO based on the Alamouti algorithm [5], [6], for the TEDS radio interface, is described. With FMT modulation the baseband time-continuous signal in TEDS is given by [1], [2]:

$$s(t) = \sum_{n=0}^{N-1} \sum_{k=0}^{K-1} a_n^{(k)} g(t - nT) e^{j(2\pi/T)nk\zeta t}, \qquad (1)$$

where n is the generic symbol within the burst, k is the index of the subcarrier, and K and N are the number of subcarriers and the transmitted (multicarrier) symbols, respectively.

Moreover, the impulse response of the square-root raised cosine filter has roll-off $\alpha = 0.2$, the signaling interval is $T = 1/2400$ s and the subcarrier spacing is $\Delta f = \zeta/T = 2700$ Hz, Thus, $\zeta = \Delta f \cdot T = 1.125$ is the measure of interference between neighboring subcarriers. This means that the frequency occupancy of each subcarrier is $(1+\alpha)/T = 2880$ s. As is known, the TEDS interface can be used for channels having the bandwidths: 25 kHz, 50 kHz, 100 kHz and 150 kHz. In order to explain the Double Input Single Output (DISO) for the downlink in the TEDS interface, the structure of Normal Downlink Burst (NDB), for each of the channels should be considered. As an example, in the following the NDB with $K = 16$ subcarriers (50 kHz channel) is described (see Fig. 1a). The burst contains the payload symbols (D marks), the header symbols (H marks), the pilot symbols (P marks) and the synchronization symbols (S marks).

To allow for the reception of signals transmitted by two antennas it is necessary to adequately locate the payload, pilot and synchronization symbols in the two symbol streams. Now, the pilot symbols should enable the receiver to carry out the estimation of channel characteristics for each of the symbol streams, and the synchronization symbols should provide efficient receiver synchronization. Of course, the number of payload and signaling symbols in the DISO and SISO schemes must remain identical.

Thus, it is not an easy task to comply with these requirements. A proposal for NDB burst adapted for DISO in the downlink is shown in Fig. 1b [7]. The pilot and synchronization symbols transmitted by the first and second antenna are marked by R and L, respectively. In the original Alamouti algorithm two symbols representing a pair are transmitted in two consecutive symbol times. Since the symbol time is small compared to the coherence time of the channel, the authors assume that, in practice, the channel characteristics are almost the same for both symbols.

Of course, in the multicarrier system the channel characteristic is a function of time and frequency [8]. However, if the channel characteristic is quasi-stationary in the small time interval (for two symbols), it is also quasi-stationary in the small frequency spacing concerning two neighboring subcarriers. As a result, a pair of symbols in the Alamouti algorithm may be represented either in frequency or time domain. The Alamouti algorithm in the proposal consid-

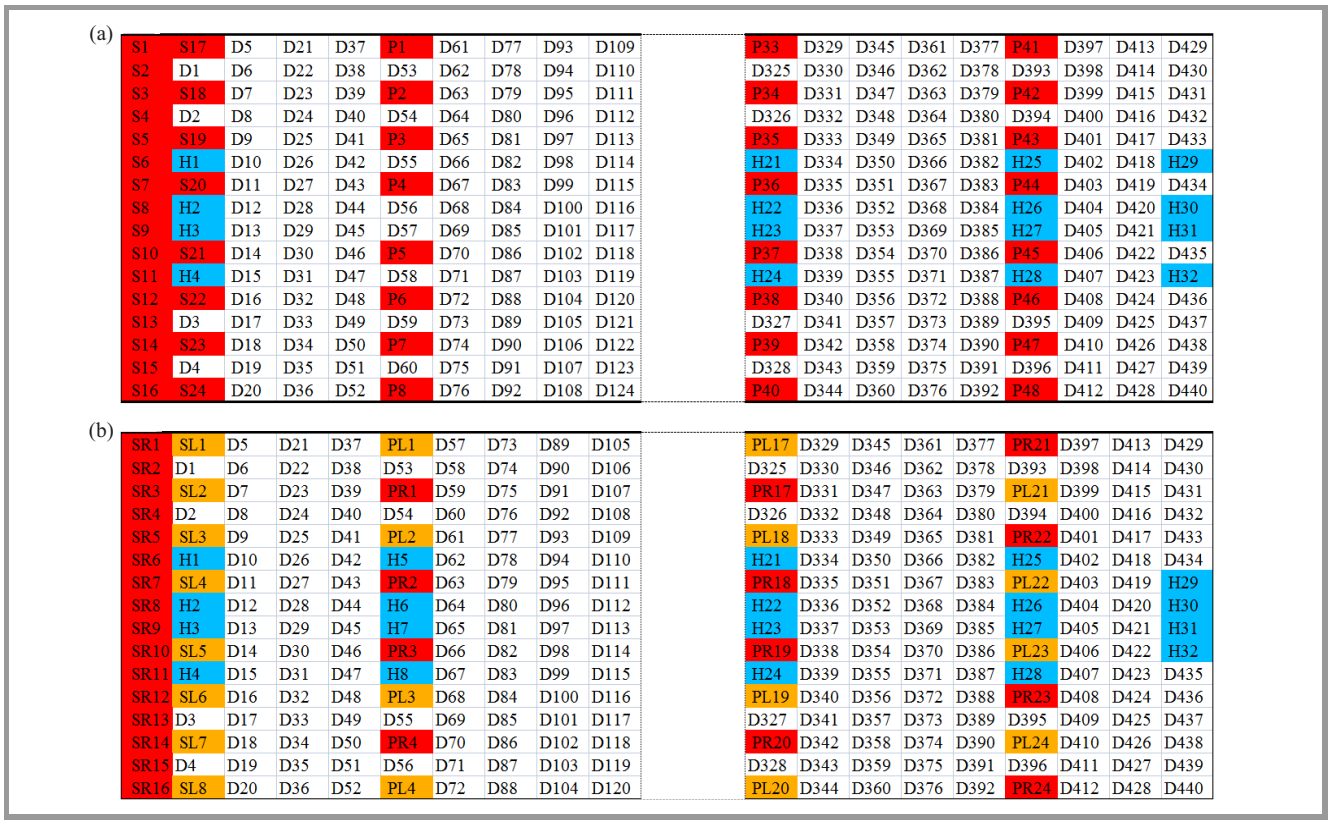

(a)

S1	S17	D5	D21	D37	P1	D61	D77	D93	D109
S2	D1	D6	D22	D38	D53	D62	D78	D94	D110
S3	S18	D7	D23	D39	P2	D63	D79	D95	D111
S4	D2	D8	D24	D40	D54	D64	D80	D96	D112
S5	S19	D9	D25	D41	P3	D65	D81	D97	D113
S6	H1	D10	D26	D42	D55	D66	D82	D98	D114
S7	S20	D11	D27	D43	P4	D67	D83	D99	D115
S8	H2	D12	D28	D44	D56	D68	D84	D100	D116
S9	H3	D13	D29	D45	D57	D69	D85	D101	D117
S10	S21	D14	D30	D46	P5	D70	D86	D102	D118
S11	H4	D15	D31	D47	D58	D71	D87	D103	D119
S12	S22	D16	D32	D48	P6	D72	D88	D104	D120
S13	D3	D17	D33	D49	D59	D73	D89	D105	D121
S14	S23	D18	D34	D50	P7	D74	D90	D106	D122
S15	D4	D19	D35	D51	D60	D75	D91	D107	D123
S16	S24	D20	D36	D52	P8	D76	D92	D108	D124

P33	D329	D345	D361	D377	P41	D397	D413	D429
D325	D330	D346	D362	D378	D393	D398	D414	D430
P34	D331	D347	D363	D379	P42	D399	D415	D431
D326	D332	D348	D364	D380	D394	D400	D416	D432
P35	D333	D349	D365	D381	P43	D401	D417	D433
H21	D334	D350	D366	D382	H25	D402	D418	H29
P36	D335	D351	D367	D383	P44	D403	D419	D434
H22	D336	D352	D368	D384	H26	D404	D420	H30
H23	D337	D353	D369	D385	H27	D405	D421	H31
P37	D338	D354	D370	D386	P45	D406	D422	D435
H24	D339	D355	D371	D387	H28	D407	D423	H32
P38	D340	D356	D372	D388	P46	D408	D424	D436
D327	D341	D357	D373	D389	D395	D409	D425	D437
P39	D342	D358	D374	D390	P47	D410	D426	D438
D328	D343	D359	D375	D391	D396	D411	D427	D439
P40	D344	D360	D376	D392	P48	D412	D428	D440

(b)

SR1	SL1	D5	D21	D37	PL1	D57	D73	D89	D105
SR2	D1	D6	D22	D38	D53	D58	D74	D90	D106
SR3	SL2	D7	D23	D39	PR1	D59	D75	D91	D107
SR4	D2	D8	D24	D40	D54	D60	D76	D92	D108
SR5	SL3	D9	D25	D41	PL2	D61	D77	D93	D109
SR6	H1	D10	D26	D42	H5	D62	D78	D94	D110
SR7	SL4	D11	D27	D43	PR2	D63	D79	D95	D111
SR8	H2	D12	D28	D44	H6	D64	D80	D96	D112
SR9	H3	D13	D29	D45	H7	D65	D81	D97	D113
SR10	SL5	D14	D30	D46	PR3	D66	D82	D98	D114
SR11	H4	D15	D31	D47	H8	D67	D83	D99	D115
SR12	SL6	D16	D32	D48	PL3	D68	D84	D100	D116
SR13	D3	D17	D33	D49	D55	D69	D85	D101	D117
SR14	SL7	D18	D34	D50	PR4	D70	D86	D102	D118
SR15	D4	D19	D35	D51	D56	D71	D87	D103	D119
SR16	SL8	D20	D36	D52	PL4	D72	D88	D104	D120

PL17	D329	D345	D361	D377	PR21	D397	D413	D429
D325	D330	D346	D362	D378	D393	D398	D414	D430
PR17	D331	D347	D363	D379	PL21	D399	D415	D431
D326	D332	D348	D364	D380	D394	D400	D416	D432
PL18	D333	D349	D365	D381	PR22	D401	D417	D433
H21	D334	D350	D366	D382	H25	D402	D418	D434
PR18	D335	D351	D367	D383	PL22	D403	D419	H29
H22	D336	D352	D368	D384	H26	D404	D420	H30
H23	D337	D353	D369	D385	H27	D405	D421	H31
PR19	D338	D354	D370	D386	PL23	D406	D422	H32
H24	D339	D355	D371	D387	H28	D407	D423	D435
PL19	D340	D356	D372	D388	PR23	D408	D424	D436
D327	D341	D357	D373	D389	D395	D409	D425	D437
PR20	D342	D358	D374	D390	PL24	D410	D426	D438
D328	D343	D359	D375	D391	D396	D411	D427	D439
PL20	D344	D360	D376	D392	PR24	D412	D428	D440

Fig. 1. Burst structures in the downlink for: (a) SISO and (b) DISO.

ered has been adapted to the format of the transmitted signal in such way that the time-dependent variable in the original algorithm has been replaced with frequency-dependent variable. In this way a space-frequency coding has been achieved and the dependence on the speed of changes in channel characteristics has been minimized. Figure 2 shows the fragment of the burst in which the data symbols $a_n^{(k)}$ presented in Eq. (1) are assigned to the suitable antennas and subcarriers [7].

As can be seen in Fig. 2, it is possible to separate $\left(a_n^{(k)}, a_{n+1}^{(k+1)}\right)$, $\left(a_{n+2}^{(k+2)}, a_{n+3}^{(k+3)}\right)$ etc., which appear in both

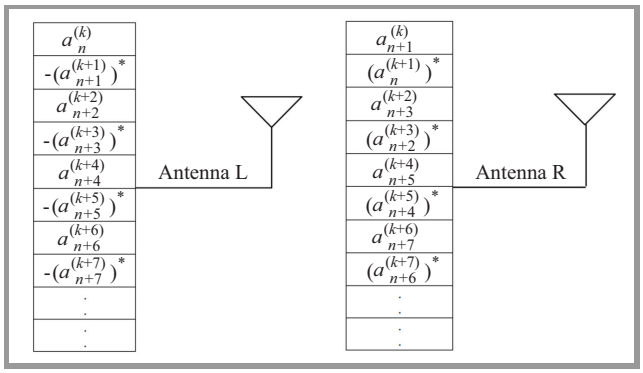

Fig. 2. Assignment of successive data symbols (indicated by the subscripts) in the burst to the subcarriers (indicated by the superscripts) and antennas, where symbol $()^*$ is the complex conjugate of the argument.

channels on the subcarriers having the same index. Furthermore, the symbols in each pair are assigned to neighboring subcarriers. Since the frequency spacing between the neighboring subcarriers is small, one can assume that each channel associated with a given antenna produces almost the same effect on both symbols of a pair.

The received pair of symbols can be written as the sum of transmitted symbols multiplied by the corresponding channels' frequency responses (channel coefficients) and the noise samples:

$$\begin{aligned} r_{n,n+1}^{(k)} &= H_L^{(k,k+1)} a_n^{(k)} + H_R^{(k,k+1)} a_{n+1}^{(k)} + z_1 \\ r_{n,n+1}^{(k+1)} &= -H_L^{(k,k+1)} \left(a_{n+1}^{(k)}\right)^* + H_R^{(k,k+1)} \left(a_n^{(k)}\right)^* + z_2 \end{aligned}, \quad (2)$$

where $r_{n,n+1}^{(k)}$, $r_{n,n+1}^{(k+1)}$ represent the combination of both symbols n and $n+1$ received on the subcarriers k and $k+1$, respectively, while $H_L^{(k,k+1)}$ and $H_R^{(k,k+1)}$ are the channels' coefficients associated with the first and second antenna and evaluated jointly for both neighboring subcarriers, whereas z_1 and z_2 are the noise samples. The symbols are evaluated as mean values separately for a real part and an imaginary part of each of the channel coefficients on both neighboring subcarriers.

However, as can be seen in Fig. 1b, some payload symbols do not appear on neighboring subcarriers and they are separated by synchronization or pilot symbols. In such cases the authors assume a channel coefficient for a pair of symbols corresponding to the synchronization or pilot

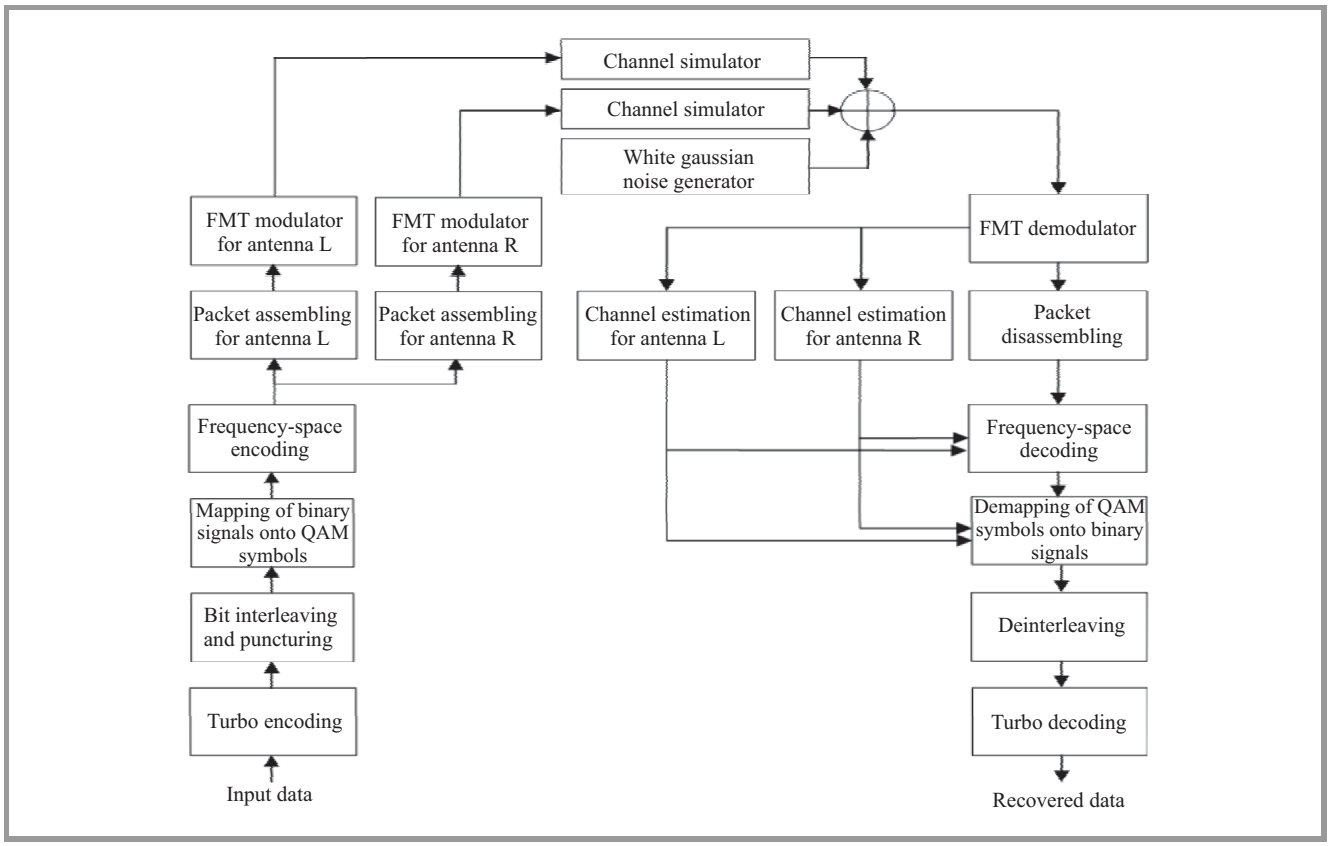

Fig. 3. Block schematic of the simulated system.

symbol. To improve the reception performance, the number of these events is reduced by the adequate distribution of payload, pilot and synchronization symbols within the burst.

The reception rule is based on Maximum-Ratio-Combining (MRC) [5], [6]:

$$\begin{aligned} \widehat{r}_n^{(k)} &= \left(H_L^{(k,k+1)}\right)^* r_{n,n+1}^{(k)} + H_R^{(k,k+1)} r_{n,n+1}^{(k+1)} \\ \widehat{r}_{n+1}^{(k+1)} &= \left(H_R^{(k,k+1)}\right)^* r_{n,n+1}^{(k)} - H_L^{(k,k+1)} r_{n,n+1}^{(k+1)} \end{aligned}, \quad (3)$$

In the Eqs. given by (3), a soft value for each received bit $b_{\widehat{r}}$ of each symbol is calculated provided that a given bit b was transmitted. To obtain the likelihood of this bit such symbol $a_i^{b^{(m)}=x}$, $x \in \{0,1\}$, must be found in the constellation of symbols for QAM modulation which takes on the value x in the m-th position of a group of bits representing that symbol and minimizes the function

$$-\log\left(p(b_{\widehat{r}} \mid b^{(m)} = x)\right) \approx \min_i \left(\widehat{r}_n^{(k)} - \left(\left|\widehat{H}_R^{k,k+1}\right|^2 + \left|\widehat{H}_L^{k,k+1}\right|^2\right) a_i^{b^{(m)}=x}\right)^2. \quad (4)$$

This approach is employed for each bit of each symbol in the received sequence of symbols.

3. Simulator for the Transmit Diversity of the TEDS Interface and Simulation Results

To investigate the performance of the above described transmit diversity method in the downlink the simulator shown in Fig. 3 has been developed [7]. The FMT modulator and demodulator used in the investigations are based on the overlap-add algorithm [9]. The rate 1/3 turbo encoder is formed by two recursive systematic convolutional encoders with 8 states each, separated by an interleaver [10]. The code rates 1/2 or 2/3 can be obtained by adequately puncturing the turbo code sequence. In the iterative turbo decoder the Max-Log-Map algorithm [6], [11] was used and the number of iterations is 10.

The selected results of simulations are shown in Figs. 4–7. They represent the relationships between FER and Eb/No for the system identified by: 16 subcarriers (50 kHz bandwidth), 1/2 code rate, 4QAM modulation on each subcarrier, the downlink transmission on 400 MHz in the typical urban (TU) and hilly terrain (HT) propagation profiles [3] and terminal speed of 50 km/h and 200 km/h, respectively.

The curves in the figures denoted by *TD* represent the results obtained when transmit diversity is employed, and the curves with that denotation missing correspond to the SISO operation. It can be seen from the figures that

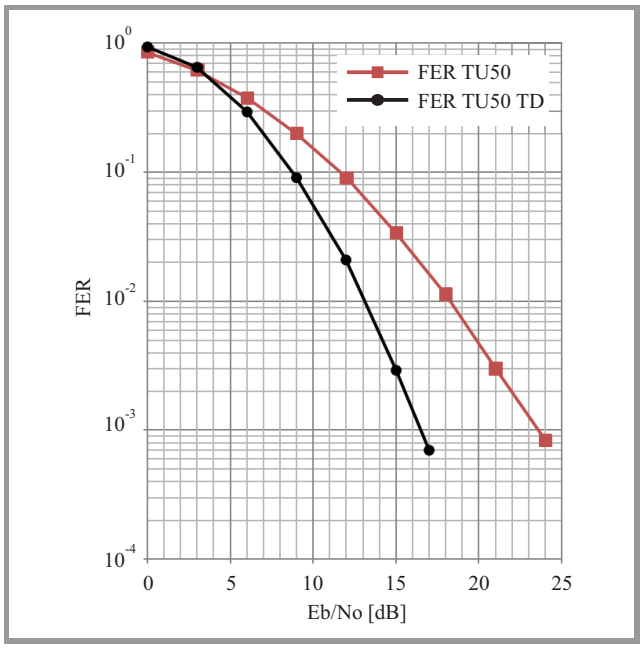

Fig. 4. Curves of FER versus Eb/No in the downlink over TU50 with 4QAM.

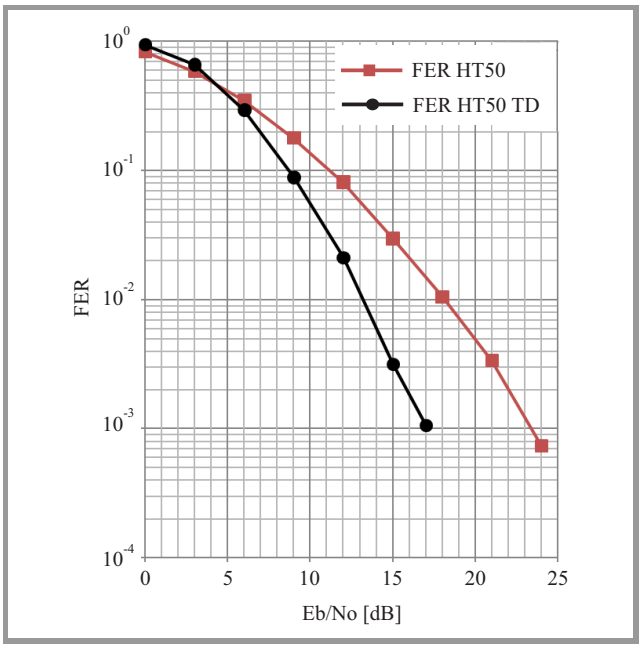

Fig. 6. Curves of FER versus Eb/No in the downlink over HT50 with 4QAM.

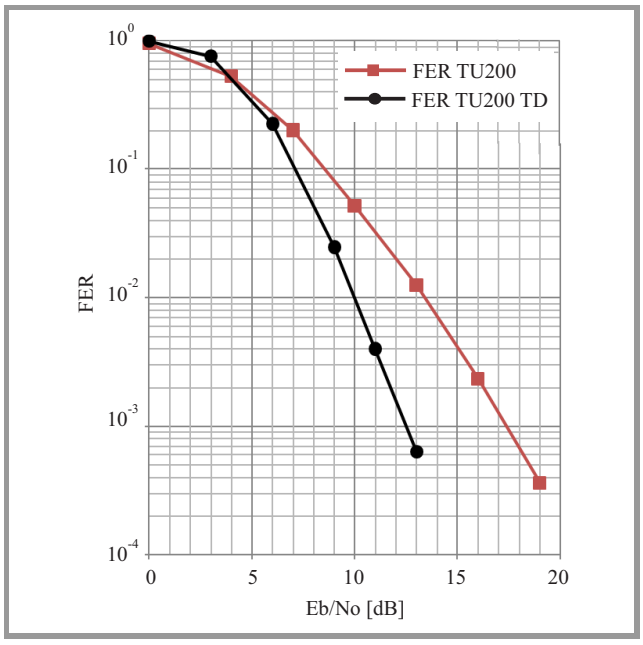

Fig. 5. Curves of FER versus Eb/No in the downlink over TU200 with 4QAM.

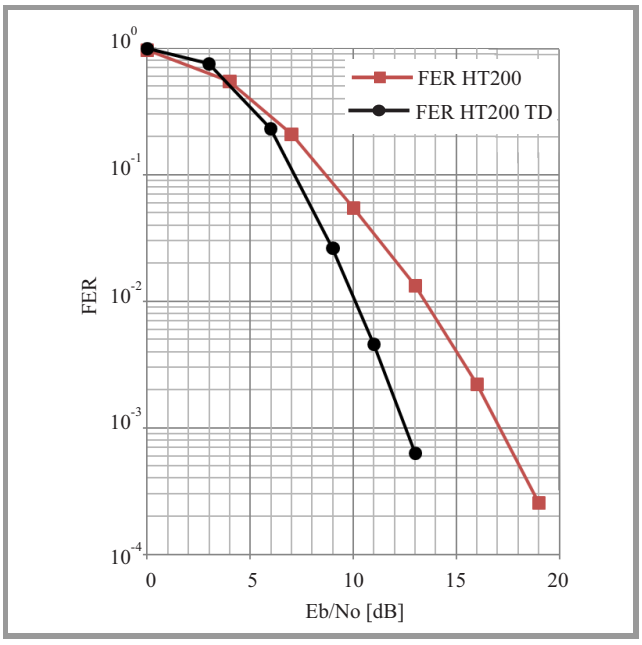

Fig. 7. Curves of FER versus Eb/No in the downlink over HT200 with 4QAM.

the proposed method provides a significant advantage. The Eb/No for the DISO configuration is reduced by 5–8 dB for FER = 10^{-3} as compared to the SISO. This transmit diversity gain is achieved irrespective of the propagation profile (TU or HT). Moreover, in both cases (with and without *TD*) one can notice that performance improves when terminal speed increases. This effect is obtained due to the decreased correlation time of fading, particularly as packet interleaving is not used. The results of the investigations also show that halving the number of symbols used for estimation of each channel characteristic with *TD*, provides sufficiently accurate channel characteristics. However, the transmit diversity gain was reduced to 5 dB for high terminal speed where the fluctuations in channel characteristics are greater. One of the reasons for this reduced gain is the reduced number of symbols used for the estimation of channel characteristics. Nevertheless, the proposed transmit diversity provides a significant improvement in system performance at the cost of an acceptable increase in complexity.

The approach presented in this paper can easily be employed for channels with other bandwidths of the TEDS radio interface.

References

[1] M. Nouri *et al.*, "TEDS: A high-speed digital mobile communication air interface for professional users – Part I: Overview of physical layer", in *Proc. 65th IEEE Veh. Technol. Conf. VTC Spring 2007*, Dublin, Ireland, 2007.

[2] M. Nouri *et al.*, "TEDS: A high-speed digital mobile communication air interface for professional users", *IEEE Veh. Techn. Mag.*, vol. 1, no. 4, pp. 32–42, 2006.

[3] "TETRA System Specification: ETSI EN 300 392-2 V3.1.1", Sept. 2006.

[4] G. Cherubini, E. Eleftherou, and S. Olcer, "Filtered multitone modulation for high-speed digital subscriber lines", *IEEE J. Selec. Areas Commun.*, vol. 20, no. 5, pp. 1016–1028, 2002.

[5] S. M. Alamouti, "A simple transmit diversity technique for wireless communications", *IEEE J. Selec. Areas Commun.*, vol. 16, no. 8, pp. 1451–1458, 1998.

[6] T. K. Moon, Error Correction Coding. Mathematical Methods and Algorithms. Hoboken, USA: Wiley, 2005.

[7] S. Możdżonek, "Adaptive reception and assessment of its quality for the next generation of TETRA system", Ph.D. thesis, Gdańsk University of Technology, Gdańsk, 2012.

[8] B. Sklar, "Rayleigh fading channels in mobile digital communication systems, Part I: Characterization", *IEEE Commun. Mag.*, vol. 35, no. 7, pp. 90–100, 1997.

[9] R. E. Crochiere and L. R. Rabiner, *Multirate Digital Signal Processing.* Upper Sadle River: Prentice Hall, 1983.

[10] O. Y. Takeshita and D. J. Costello, "New deterministic interleaver designs for turbo codes", *IEEE Trans. Infor. Theory*, vol. 46, no. 6, pp. 1988–2006, 2000.

[11] J. P. Woodard and L. Hanzo, "Comparative study of turbo decoding techniques: An overview", *IEEE Trans. Veh. Technol.*, vol. 49, no. 6, pp. 2208–2233, 2000.

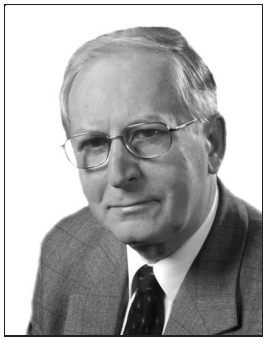

Dominik A. Rutkowski received M.Sc., Ph.D. and D.Sc. degrees in Electronic Engineering from Gdańsk University of Technology (GUT), Gdańsk, Poland, in 1963, 1968 and 1975, respectively. He has been with GUT since 1963, first lecturing in Automatic Control Systems and later in Communications Systems. His activities were focused initially on the problems of automatic control systems and, in particular, on the optimal identification of control plants and adaptive systems. Since 1975, he has been Associate Professor in the Institute of Communications Systems. In 1975–1976 he was awarded a yearlong Fulbright – Hays Fellowship and was engaged in research into computer networks, and also in education at the Department of Electrical Engineering and Computer Science, Columbia University, New York. After 1983 his scientific interests focused on digital radio communications systems. In 1989 he obtained the position of Full Professor at GUT in Radio Communications Systems. In 1990 he became a Full Professor in Digital Communications Systems at the Department of Electronic Systems, Aalborg University, Denmark, and his research concentrated on the development of spread spectrum systems. In 1993, he continued at GUT and for the next 20 years his research focused on the performance and capacity evaluation of the 2nd, 3rd and 4th generation of cellular systems, wireless systems and the digital trunked radio system TETRA. He has published more than 180 papers in scientific journals and conference proceedings, and he is the author of 5 books.
E-mail: nick@eti.pg.gda.pl
Faculty of Electronics, Telecommunications and Informatics
Gdańsk University of Technology
Gabriela Narutowicza st 11/12
80-233 Gdańsk, Poland

Sławomir Możdżonek received M.Sc. degree in Telecommunications from Gdańsk University of Technology in 2004 and the Ph.D. degree in Telecommunications from the same university in 2012. Since October 2004, he has been working at Samsung Electronics Poland as a software engineer. He has published several papers in scientific journals and conference proceedings. His main research interests include adaptive receivers, channel estimation methods, space-time coding and multicarrier techniques.
E-mail: s.mozdzonek@gmail.com

Paper

Normalized Gaussian Approach to Statistical Modeling of OFDM Signals

Adam Rudziński

SKA Polska Sp. z o.o., Warsaw, Poland

Abstract—This article concerns modeling of statistical properties of OFDM signals with the help of "normalized Gaussian" model, proposed by Kotzer *et al.* In this paper there is provided an extended formulation of the model, supplemented by an expression for probability density, extending possible applications of the model in theoretical works. Numerical results for verification of the model are provided and a more accurate alternative is suggested.

Keywords—M-PSK, OFDM, sample value distribution, statistical model.

1. Introduction

In nowadays world there exists a demand for novel technical solutions introducing new qualities and functionalities into everyday life. The recent 10–20 years have led to an enormous technical progress, in particular in the field of electronics and telecommunications – global computer network or mobile telephony are good examples of developments which had a great impact on the way of living. Still, the pursuit of new technical solutions and higher performance continues.

The development in telecommunications was to large extent related to practical implementation of Orthogonal Frequency Division Multiplexing (OFDM) technique. It was first proposed and examined over 40 years ago [1]–[3], but it was impossible to use it without fast digital signal processing circuits available today. Currently this technique is used in, e.g., wireless LAN networks, terrestrial digital television and optical fibre communications, so the possibility of increasing data throughput depends largely on adaptation of devices for operation with larger numbers of subcarriers (increased bandwidth) and higher-order modulation schemes, i.e., with more densely populated constellations. A relevant example is the new DVB-T2 standard, including 256-QAM modulation, in contrast to the older DVB-T, limited to 64-QAM. Such advancement requires the understanding and proper modeling of phenomena occurring in signal transmission. In particular, this can be achieved by construction of analytic models, which explicitly reveal fundamental properties and relations in the system.

The conventional way of modeling statistical properties of the OFDM signal is to invoke the Central Limit Theorem and assume for the signal value x a zero-mean Gaussian probability distribution

$$G_\sigma(x) = \frac{1}{\sqrt{2\pi\sigma^2}} \exp\left(-\frac{x^2}{2\sigma^2}\right), \tag{1}$$

with variance σ^2 equal to the mean power of the signal. This approach usually leads to sufficiently accurate results, especially if a large number of subcarriers is in application. Still, this model is obviously an approximation, since it does not limit the signal value. It predicts non-zero probability even for nonphysically large x (in the so-called distribution tails). As such, it tends to become inaccurate in some cases, where suppressing of the distribution tails is of high importance, for example, in calculation of clipping noise when the clipping is small. Clearly, advanced modeling should be based on a model better resembling properties of the signal, but such models, if known at all, are very rarely found in the literature.

As an attempt to overcome the problem of unlimited values, Kotzer, Har-Nevo, Sodin and Litsyn have proposed another statistical model, which they have called "normalized Gaussian" model [4]. It is applicable to OFDM signal with subcarriers modulated according to a constant amplitude constellation (e.g. M-PSK). This model is based on such modification of the Gaussian distribution given by Eq. (1), which explicitly limits the values and assures preservation of energy in the whole OFDM symbol, resulting in inherent confinement of signal values within a finite range. Hence, it offers a potentially advantageous alternative to conventional Gaussian model. However, the original formulation of the normalized Gaussian model makes it suitable only for problems of specific kind, with limited usability for analytic derivations. These issues are addressed in this work, the aim of which is to extend or modify the formulation of the model and examine its most important properties.

This paper is organized as follows. Section 2 defines the notation and introduces the concept of the normalized Gaussian model according to formulation by Kotzer *et al.* [4]. Next, the model is reformulated in a more general and analytic way in Section 3. In Section 4 there is provided a numerical verification of the model. Section 5 proposes an improved model, obtained as a combination of the conventional and the normalized Gaussian models. An example of

application and comparison of all these models is presented in Section 6, and Section 7 concludes the paper.

2. OFDM Signal and the Normalized Gaussian Model

In a modern communication device, transmitted data are mapped onto points ζ_m of a constellation, i.e. set

$$\Omega = \{\zeta_m \in \mathbb{C}; m = 1, \ldots, \|\Omega\|\}, \tag{2}$$

where $\|\Omega\|$ denotes the number of elements in Ω. A signal with Orthogonal Frequency Division Multiplexing (OFDM) is generated by Inverse Discrete Fourier Transformation (IDFT) of a vector $\boldsymbol{A} = \left[A_1 e^{j\phi_1} \ldots A_K e^{j\phi_K}\right] \in \Omega^K$ containing K complex values representing spectral components of the signal (subcarriers), with amplitudes $A_k > 0$ and phases $\phi_k \in [0; 2\pi)$, where $k = 1, \ldots, K$. The result of the transformation constitutes the time-domain representation of the signal. In general, this signal is complex, but for physical processing, e.g., for digital-to-analog conversion, it is split into two real signals, given by its real and imaginary parts, and each of them is processed at least in a part separately. Here it is assumed, that these two signals have the same statistical properties and further only the real part of the complex time-domain signal is considered. It can be represented as a sequence of N_S samples

$$x_i \equiv x(iT), \quad i = 0, 1, \ldots, N_S - 1, \tag{3}$$

of the continuous time-domain signal

$$x(t) = \sum_{k=1}^{K} A_k \cos(\omega_k t + \phi_k), \tag{4}$$

where T is the sampling period and ω_k denotes angular frequency of the k-th subcarrier. The signal is divided into symbols of duration T_S (in practical applications extended by guard interval, which is not relevant here and therefore ignored), so to preserve orthogonality of subcarriers their angular frequencies are chosen as

$$\omega_k = k\omega_1, \quad \text{with } \omega_1 = \frac{2\pi}{T_S}. \tag{5}$$

In general, for consideration of statistical properties of the signal, amplitudes A_k are represented by a random variable A with the probability distribution

$$f_A(A) = \frac{1}{\|\Omega\|} \sum_{m \in \Omega} \delta(A - |\zeta_m|), \tag{6}$$

and phases ϕ_k are treated as independent random variables, distributed uniformly on a subset of the interval $[0; 2\pi)$. The mean power of the OFDM symbol defined by Eqs. (3) or (4) is equal to

$$\sigma^2 = K\frac{\langle A^2 \rangle}{2}. \tag{7}$$

Here, for consideration of only M-PSK constellations, it is assumed that each $|\zeta_m| = \frac{1}{K}$. With this choice the signal is scaled to obtain values from the range $[-1; 1]$ and its mean power becomes $\sigma^2 = \frac{1}{2K}$.

The limitation of signal values is violated in the conventional model based on the Central Limit Theorem and Gaussian probability distribution, what, as mentioned above, may cause this model to be inadequate for modeling of certain phenomena or in some cases. The problem of non-physically large values is alleviated by proposition of Kotzer *et al.*, who have suggested to introduce normalization of the Gaussian-distributed estimate, which would explicitly impose the preservation of energy of the whole OFDM symbol [4]. According to this approach, assuming $K = N_S$, the absolute value of the i-th sample of the complex signal obtained by the IDFT is a random variable defined as

$$r_i = \frac{|g_i|}{\sqrt{\sum_{k=0}^{N_S-1} |g_k|^2}}, \quad i = 0, 1, \ldots, N_S - 1, \tag{8}$$

where g_k are independent and identically distributed random variables with complex Gaussian distribution, $g_k \sim \mathcal{CN}(0, \sigma^2)$. This way, for each sample the value of r_i remains within the range from 0 to 1. Such formulated model has been called the normalized Gaussian model. It is applicable to OFDM signals obtained for subcarriers modulated according to a constant amplitude modulation scheme, e.g. M-PSK.

In [4] it has been shown, that the normalized Gaussian model reproduces the properties of the signal very well. Thus, it may be advantageous to use this model instead of the conventional Gaussian-based. However, the model as formulated by Kotzer *et al.* in [4] relates to absolute values of complex signal samples, therefore is applicable only to severely limited range of problems, not including, for example, digital-to-analog conversion, performed separately for real and imaginary parts. It is not defined in terms of probability distribution for r_i, hence impractical for analytic derivations. The model assumes the number of samples to be equal to the number of subcarriers and as such it concerns only signal at the Nyquist limit for the highest frequency subcarrier, i.e. without any oversampling, always present in practical applications. Therefore, for wider application, the model needs to be generalized to describe signed values of samples, it should be reformulated in terms of probability density function and apply to the cases in which the signal is oversampled.

3. Modification of the Normalized Gaussian Model

The absolute value of a complex OFDM signal (i.e. IDFT output) does not depend on the phases of subcarriers per se, but on their differences. Thus, one of the phases can be considered to be the global phase of the signal. Hence,

variable $r_i e^{j\phi_i}$ can be identified with the complex value of the i-th sample. However, the random phase ϕ_i can be also identified with the phase of the complex variable g_i, and therefore the variable corresponding to one of the real-valued signals, that can be fed to a digital-to-analog converter or other processing device, is

$$\mathrm{Re}\left\{r_i e^{j\phi_i}\right\} = \frac{\mathrm{Re}\{g_i\}}{\sqrt{\sum_{k=0}^{N_S-1}|g_k|^2}}. \tag{9}$$

The Eq. (9) can be used for generation of random vectors of samples for simulation, since it imposes the correct mean signal power for a group of samples by using a common normalization factor, explicitly related to individual samples of the whole vector. Obviously, $|g_k|^2 = \mathrm{Re}\{g_k\}^2 + \mathrm{Im}\{g_k\}^2$ and both real and imaginary part of g_k can be considered to be independent random variables with real-valued normal distribution, $\mathrm{Re}\{g_k\}, \mathrm{Im}\{g_k\} \sim \mathcal{N}(0,\sigma^2)$. Therefore, for each sample, the sum in the nominator comprises: the square of the variable $\mathrm{Re}\{g_i\}^2$, and other $2N_S - 1$ independent random variables with the same Gaussian distribution. Because statistical properties are the same for each sample, at least to large extent the properties of the signal can be characterized by properties of a single sample. Focusing on just a single sample one can treat all the samples as statistically independent, and then the sum in nominator of Eq. (9) can be expressed as

$$\sum_{k=0}^{N_S-1}|g_k|^2 = \mathrm{Re}\{g_i\}^2 + \sigma^2 Q_{2N_S-1}, \tag{10}$$

where $Q_n \in [0;\infty)$ is defined as sum of n squares of independent and identically distributed random variables with standard normal distribution $\mathcal{N}(0,1)$. It is well known that such Q_n is distributed according to the chi-squared distribution with n degrees of freedom, $Q_n \sim \chi_n^2$, with the probability density function

$$\chi_n^2(q) = \frac{q^{\frac{n}{2}-1}e^{-\frac{q}{2}}}{2^{\frac{n}{2}}\Gamma\left(\frac{n}{2}\right)}\theta(q), \tag{11}$$

where $\Gamma(x)$ denotes the gamma function and $\theta(q)$ is the Heaviside step function. The random variable defined by Eq. (9) can be further subjected to the following:

- substitution $v = \mathrm{Re}\{g_i\}/\sigma \sim \mathcal{N}(0,1)$,
- relating the mean power to the number of subcarriers K, by using in sum (10) a random variable Q_{2K-1} instead of Q_{2N_S-1}.

This way, each sample of considered signal is represented by random variable

$$\xi = \frac{v}{\sqrt{v^2 + Q_{2K-1}}} \in [-1;1]. \tag{12}$$

Because the random variables v and Q_{2K-1} are independent, the probability density function $f_\xi(\xi)$ for variable ξ can be calculated using the formula (with $q \equiv Q_{2K-1}$ for brevity):

$$f_\xi(\xi) = \int_0^\infty \mathrm{d}q\, \chi^2_{2K-1}(q)\, G_1(v(q,\xi))\left|\frac{\partial v}{\partial \xi}\right|. \tag{13}$$

The variable v in function of q and ξ is given by

$$v(q,\xi) = \xi\sqrt{\frac{q}{1-\xi^2}}. \tag{14}$$

Thus, remembering that

$$\int_0^\infty \mathrm{d}q\, q^n e^{-aq} = \frac{\Gamma(n+1)}{a^{n+1}}, \quad \text{where } a>0,\ n>-1, \tag{15}$$

$\Gamma(n+1) = n\Gamma(n)$ and $\Gamma\left(\frac{1}{2}\right) = \sqrt{\pi}$, one obtains:

$$f_\xi(\xi) = \frac{1}{2}\binom{K-1}{\frac{1}{2}}\left(1-\xi^2\right)^{K-\frac{3}{2}}\theta(1-|\xi|), \tag{16}$$

with the generalized binomial for $\alpha,\beta \in \mathbb{R}$ defined as

$$\binom{\alpha}{\beta} = \frac{\Gamma(\alpha+1)}{\Gamma(\beta+1)\Gamma(\alpha-\beta+1)}. \tag{17}$$

To check that this distribution is in fact normalized to 1 it is convenient to change the integration variable to $u = \xi^2$ and make use of the identity

$$\int_0^1 \mathrm{d}u\, u^\alpha (1-u)^\beta = \frac{\Gamma(\alpha+1)\Gamma(\beta+1)}{\Gamma(\alpha+\beta+2)}. \tag{18}$$

Similarly, one can easily calculate various absolute moments of this distribution

$$\langle|\xi|^n\rangle = \frac{1}{\sqrt{\pi}}\frac{\Gamma(K)\Gamma\left(\frac{n+1}{2}\right)}{\Gamma\left(K+\frac{n}{2}\right)}, \tag{19}$$

in particular the mean square value $\langle\xi^2\rangle = \frac{1}{2K}$, reproducing correctly the mean power of the signal. It is interesting to

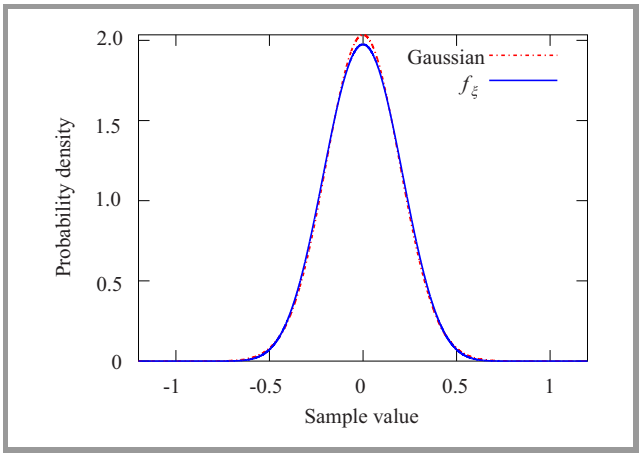

Fig. 1. Comparison of Gaussian probability distribution and the distribution f_ξ, for $K = 13$.

note, that the expression $f_\xi(\xi)$ for one subcarrier, $K = 1$, leads to the arcsine distribution, what is the correct result for a single harmonic function (sine or cosine) of a uniformly distributed variable.

The plot of the distribution f_ξ in comparison to Gaussian is presented in Fig. 1. Both distributions are very similar in the central portion. The Gaussian distribution has a little higher value near 0, on the slopes is a little below f_ξ and again becomes higher at the tails. The most important difference is that the distribution f_ξ has a compact support, and is zero outside the range of allowed values of the signal. It will be seen on the next plots, which are drawn in the logarithmic scale.

4. Numerical Verification

The correctness of the derived probability distribution f_ξ has been verified by numerical simulation performed in Octave [7]. Each numerical estimate has been obtained as a normalized histogram of values of samples for 1 million randomly generated discrete OFDM symbols with specified constellation, number of subcarriers K and number of samples per symbol N_S. For calculation of the histogram, full range of signal samples (i.e. $[-1;1]$) has been divided into 101 "bins" of equal width, but in the presented plots, this range has been narrowed down to the range of values observed in the simulation (apparently, the other values occur with probabilities too small to have been observed).

First, it was checked that the expression (16) for f_ξ correctly reproduces the probabilities of observation of sample values $\mathrm{Re}\{r_i e^{j\phi_i}\}$ defined by Eq. (9). Exemplary comparisons of the derived and numerical results are shown in Fig. 2. The plots in the figure illustrate that the expression (16) in fact defines the correct probability distribution for the normalized Gaussian model.

Next, the derived probability distribution f_ξ has been compared with numerical results for various OFDM signals and with conventional Gaussian distribution $G_{1/\sqrt{2K}}$ with the same variance. For each case, discrete symbols according to expressions (3) and (4) have been generated with the help of IDFT. The results are presented in Fig. 3 for QPSK constellation and in Fig. 4 for other constant amplitude constellations (8-PSK and 32-PSK). As it can be seen, both analytic models give similar results, in general reproducing the numerical results well. However, neither of them predicts, that the signal samples tend to group at particular values, especially for lower order constellations with a low number of subcarriers K. This effect becomes smaller with increased oversampling (the ratio N_S/K) or the order of constellation. It can be alleviated by introduction of a random global phase shift in constellation for each symbol separately, what causes "smoothing" of the numerical results – for example, see the plot shown in Fig. 5.

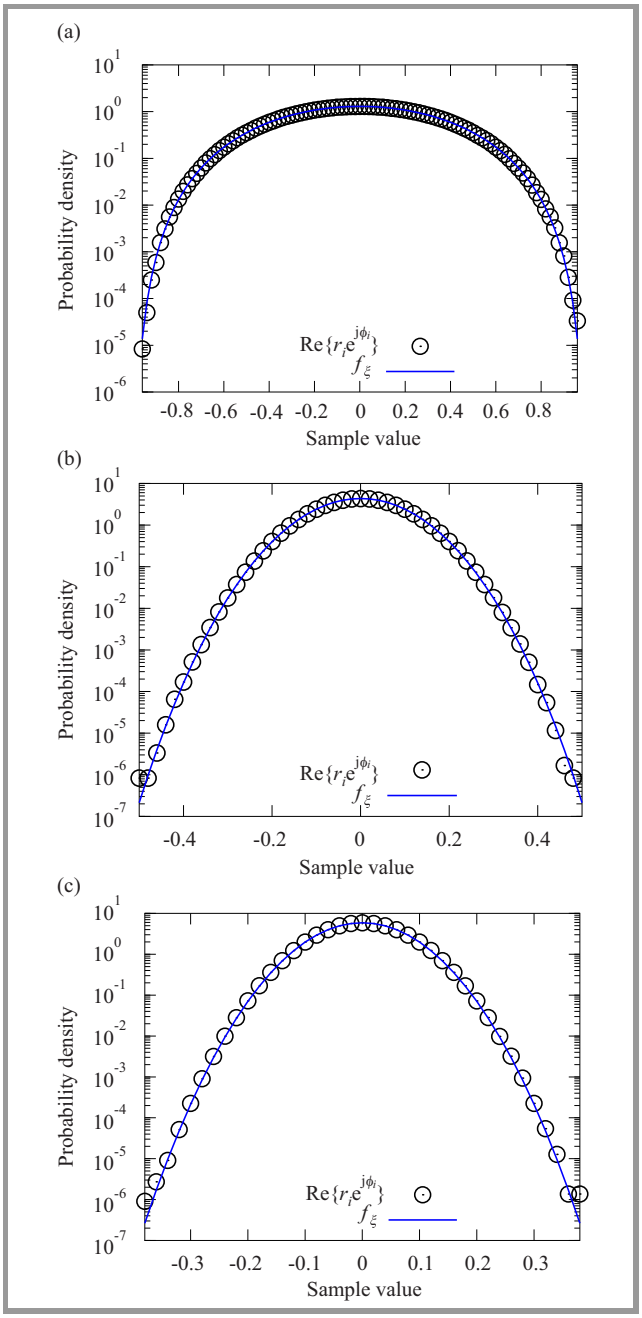

Fig. 2. Comparison of numerically estimated probability distribution of $\mathrm{Re}\{r_i e^{j\phi_i}\}$ and the derived expression f_ξ for OFDM symbols: (a) $K = 6$ and $N_S = 16$, (b) $K = 60$ and $N_S = 256$, (c) $K = 110$ and $N_S = 256$.

5. Geometrically Averaged Model

From the plots presented in Section 4 it is apparent that the conventional Gaussian model overestimates the tail distribution, while the distribution f_ξ underestimates it. Therefore, an obvious attempt to increase the accuracy of the modeling is to use the geometrical average of the probability distributions in these two models, i.e.

$$h_\xi(\xi) = N_h H_\xi(\xi), \tag{20}$$

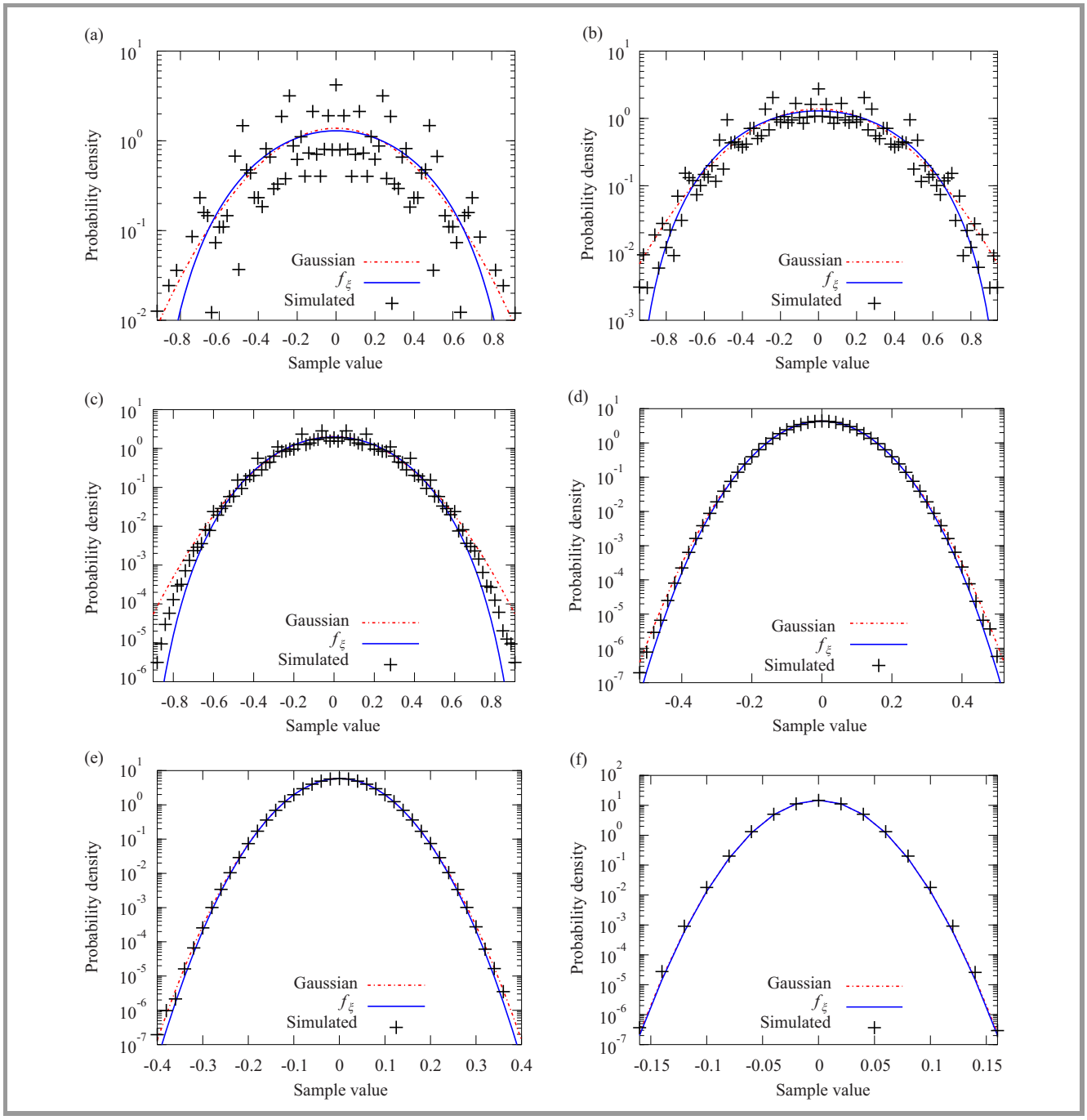

Fig. 3. Exemplary results for verification of distribution f_ξ for QPSK constellation: (a) $K = 6$ and $N_S = 16$, (b) $K = 6$ and $N_S = 32$, (c) $K = 13$ and $N_S = 32$, (d) $K = 60$ and $N_S = 256$, (e) $K = 110$ and $N_S = 256$, (f) $K = 700$ and $N_S = 2048$.

where dependence on ξ is given by

$$H_\xi(\xi) = \sqrt{G_{1/\sqrt{2K}}(\xi) f_\xi(\xi)}, \tag{21}$$

and the normalization constant

$$N_h = \left(\int_{-1}^{1} \mathrm{d}\xi \, H_\xi(\xi) \right)^{-1}. \tag{22}$$

The comparison of such defined probability distribution with numerical results presented above is shown in Fig. 6. It can be seen, that both results fit each other very well, thus the distribution h_ξ could be used for better accuracy. However, it seems that analytic expression for h_ξ is rather complicated and it will not be derived here any further.

6. Clipping Noise

A commonly known problem in which tails of the probability distribution used for modeling of the signal

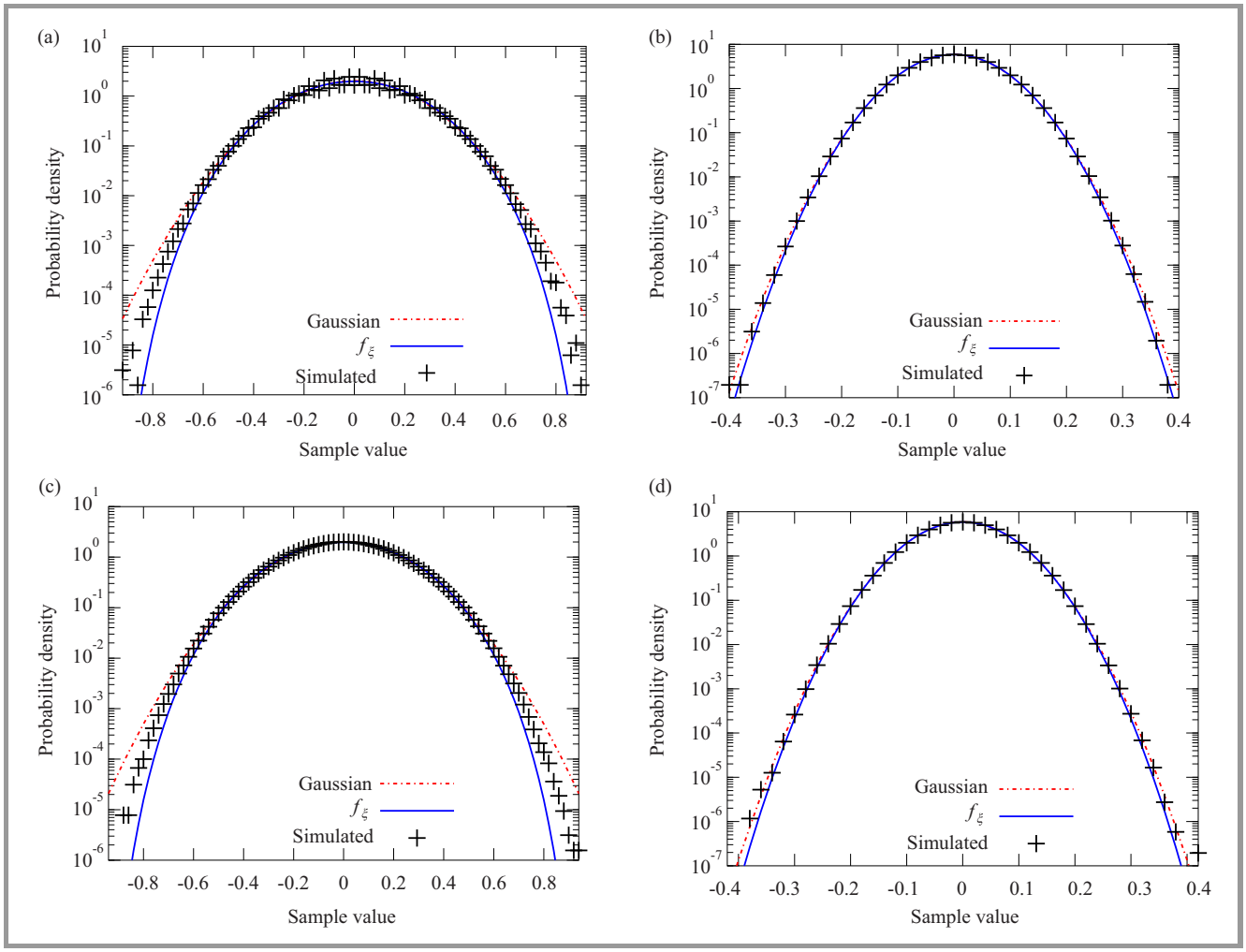

Fig. 4. Exemplary results for verification of distribution f_ξ for M-PSK constellations: (a) 8-PSK, $K = 13$, $N_S = 32$, (b) 8-PSK, $K = 110$, $N_S = 256$, (c) 32-PSK, $K = 13$, $N_S = 32$, (d) 32-PSK, $K = 110$, $N_S = 256$.

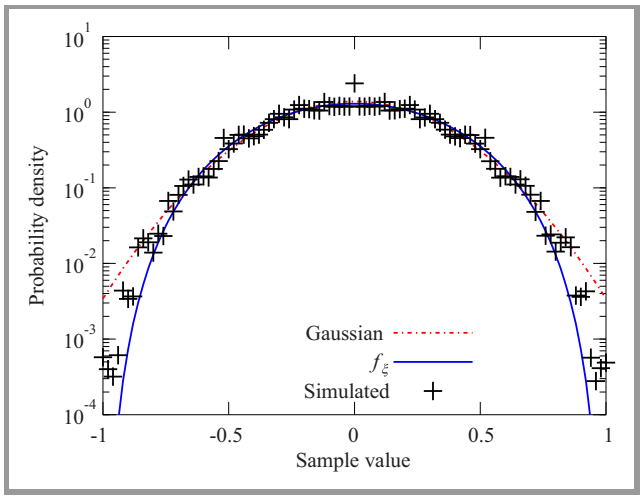

Fig. 5. Exemplary result of simulation with random global phase shift for QPSK, $K = 6$, $N_S = 16$.

have a significant impact is the calculation of clipping noise [5], [6]. This noise usually is considered for digital-to-analog or analog-to-digital converters and amplifiers. Clipping occurs when a device limits the absolute value of the output signal to a certain level A_{clip}. It is convenient to define this level in terms of a clipping factor

$$\gamma = \frac{A_{\text{clip}}}{\sigma}, \tag{23}$$

so that the signal is constrained to $\pm\gamma\sigma$. The clipped portion of the signal is a distortion contributing to the total noise. Following the simplest derivation signal with uncorrelated time-domain values or samples [5], the power of the clipping noise is

$$\sigma_c^2(\gamma) = 2\int_{\gamma\sigma}^{\infty} \mathrm{d}\xi\, (\xi - \gamma\sigma)^2\, p(\xi), \tag{24}$$

where $p(\xi)$ denotes the probability distribution assumed for the signal value ξ. Obviously, if the signal is already limited below $\gamma\sigma$ no clipping occurs and any model allowing the signal to have arbitrarily large values (like the conventional Gaussian model) will lead to incorrect results. Assuming the Gaussian model, i.e $p(\xi) = G_\sigma(\xi)$,

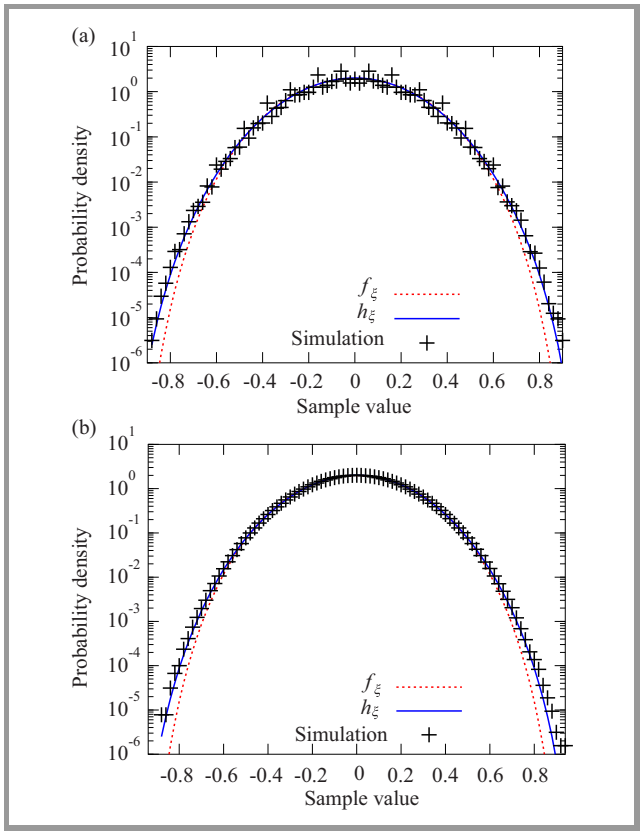

Fig. 6. Exemplary results for verification of distribution h_ξ for M-PSK constellations: (a) QPSK, $K = 13$, $N_S = 32$, (b) 32-PSK, $K = 13$, $N_S = 32$.

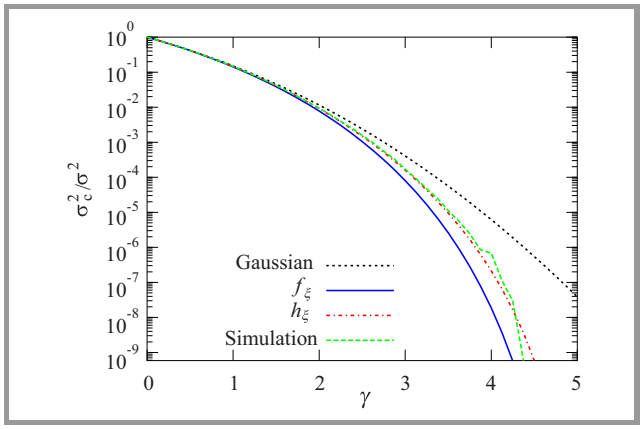

Fig. 7. Clipping noise to signal power ratio obtained with various signal models in comparison to results of simulation for QPSK, $K = 13$ and $N_S = 32$.

the clipping noise to signal power ratio is given by the following expression:

$$\left(\frac{\sigma_c^2(\gamma)}{\sigma^2}\right)_G = (1+\gamma^2)\,\mathrm{erfc}\left(\frac{\gamma}{\sqrt{2}}\right) - \sqrt{\frac{2\gamma^2}{\pi}}\,\mathrm{e}^{-\frac{\gamma^2}{2}}, \quad (25)$$

wherein the complementary error function

$$\mathrm{erfc}(x) = \frac{2}{\sqrt{\pi}}\int_x^\infty \mathrm{d}t\,\mathrm{e}^{-t^2}. \quad (26)$$

Similar results for $p(\xi) = f_\xi(\xi)$ and $p(\xi) = h_\xi(\xi)$ are here calculated numerically and a comparison of these three results with simulation is presented in Fig. 7. In addition to being time-consuming, the simulation becomes inaccurate for higher values of γ, since the probability of observing sample value high enough to be clipped becomes too small for occurrence of clipping within a given number of random signal symbols (here 100,000). In particular, this relates to clipping at value of $\gamma \approx 4$, which is of practical interest. It can be seen, that, as could be predicted from previous results presented here, the Gaussian model overestimates the clipping noise, at $\gamma \approx 4$ significantly, while the normalized Gaussian model, based on expression for f_ξ, underestimates it, and using h_ξ, the geometrical average of the Gaussian distribution and f_ξ, reproduces the clipping noise very well. This illustrates well an advantage of using proper analytic models, allowing to obtain accurate results very quickly, except of providing a much better insight into the physical phenomenon.

7. Conclusions

In this paper there is provided an extension, with slight modification, of a statistical model of OFDM signal, so-called normalized Gaussian model, originally proposed by Kotzer *et al.* [4]. Treating the signal sample values as independent random variables allows to derive their probability distribution f_ξ given by expression (16). It has been shown, that this expression correctly reproduces statistical properties of the original model. The predictions of the extended model have been compared to results of numerical simulations and on their basis a more accurate model, combining both conventional Gaussian model and the normalized Gaussian model by means of a geometrical average, was proposed. As an example of application, the models were used for calculation of clipping noise.

The probability distribution f_ξ turns out to be accurate to the same degree as the conventionally used Gaussian distribution, with the difference, that while Gaussian overestimates the probability of occurrence of the higher values, the distribution f_ξ tends to underestimate it. Being expressed by a relatively simple function, distribution f_ξ allows to calculate and obtain closed-form results for numerous parameters of the signal, thus it may be particularly useful for theoretical research. The proposed here "geometrically averaged" distribution h_ξ, although providing the most accurate results of all three, seems to be more complicated and might lead to more cumbersome expressions. However, even such formulation as presented offers the benefit of quickly obtained results by simple numerical calculation.

Concluding, the expressions obtained in this paper provide alternatives to conventional Gaussian model and might contribute to theoretical characterization and development of telecommunication devices, especially those using susceptible to noise higher-order modulation schemes.

References

[1] R. W. Chang, "High-speed multichannel data transmission with bandlimited orthogonal signals", *Bell Sys. Tech. J.*, vol. 45, pp. 1775–1796, 1966.

[2] B. R. Saltzberg, "Performance of an efficient parallel data transmission system", *IEEE T. Commun. Technol.*, vol. 15, pp. 805–811, 1967.

[3] S. B. Weinstein and P. M. Ebert, "Data transmission by frequency-division multiplexing using the discrete Fourier transform", *IEEE T. Commun. Technol.*, vol. 19, pp. 628–634, 1971.

[4] I. Kotzer, S. Har-Nevo, S. Sodin, and S. Litsyn, "A model for OFDM signals with applications", in *Proc. 18th Eur. Wirel. Conf.,* Poznań, Poland, 2012.

[5] D. J. G. Mestdagh, P. M. P. Spruyt, and B. Biran, "Effect of amplitude clipping in DMT-ADSL transceivers", *Electron. Lett.*, vol. 29, pp. 1354–1355, 1993.

[6] R. Gross and D. Veeneman, "SNR and spectral properties for a clipped DMT ADSL signal", in *Proc. 1994 IEEE ICC Conf. Rec.*, vol. 2, New Orleans, USA, 1994, pp. 843–847.

[7] Octave [Online]. Available: http://octave.org/

Adam Rudziński received the M.Sc. and Ph.D. degrees in Electronics from Warsaw University of Technology, Poland, in 2004 and 2010, respectively, and M.Sc. degree in Theoretical Physics from Warsaw University, Poland, in 2009. His scientific interests include: modeling of electronic devices and signals, construction of electronic devices , interaction of electromagnetic waves with matter, quantum optics. Currently, he is employed at SKA Polska Sp. z o.o. as an electronics designer.

E-mail: a.rudzinski@ska-polska.pl

SKA Polska Sp. z o.o.

Al. Jerozolimskie 125/127, lok. 406

02-017 Warsaw, Poland

Paper

Subcarrier Gain Based Power Allocation in Multicarrier Systems

Mohammed Abd-Elnaby[1], Germien G. Sedhom[1], Nagy W. Messiha[1], Fathi E. Abd El-Samie[1], and Xu Zhu[2]

[1] *Faculty of Electronic Engineering, Menoufia University, Menouf, Egypt*
[2] *Department of Electrical Engineering and Electronics, The University of Liverpool, Liverpool, UK*

Abstract—The Orthogonal Frequency Division Multiplexing (OFDM) transmission is the optimum version of the multicarrier transmission scheme, which has the capability to achieve high data rate. The key issue of OFDM system is the allocation of bits and power over a number of subcarriers. In this paper, a new power allocation algorithm based on subcarrier gain is proposed to maximize the bit rate. For OFDM systems, the Subcarrier Gain Based Power Allocation (SGPA) algorithm is addressed and compared with the standard Greedy Power Allocation (GPA). The authors demonstrate by analysis and simulation that the proposed algorithm reduces the computational complexity and achieves a near optimal performance in maximizing the bit rate over a number of subcarrier.

Keywords—GPA, OFDM, QAM, SNR.

1. Introduction

Orthogonal Frequency Division Multiplexing (OFDM) is a flexible and bandwidth-efficient modulation technique, which has the capability to combat Inter-Symbol-Interference (ISI) [1]. OFDM systems divide the channel into many orthogonal and tightly allocated subcarriers, which differ in signal-to-noise ratio (SNR). Resource allocation (bit and power) to the subcarriers is a fundamental aspect in the design of multicarrier system. This includes the achievement of maximum bit rate and minimum total transmit power (margin maximization) to the subcarriers and this achievement depends on the channel gain of each subcarrier. This problem has been studied in many recent researches.

The minimum power allocation for increasing the bit rate is a fundamental problem, which has a well known closed form solution called waterfilling [2], [3]. This resource allocation strategy is not practical, since the channel with best gain allocates more power than the other channel so a lot of users will not be given a chance to transmit data at all subcarriers. This problem was addressed in [4], [5], which each user is able to transmit at minimum rate and the objective was to maximize the minimum the data rate of users. In [6] a block waterfilling algorithm is proposed, which enhances the throughput (bit rate) but it gives low amount of additional computational complexity. In [7] an asymptotic Network Utility Maximization (NUM) is proposed, which maximizes network utility over the long-term throughput region by gradient-based scheduler. In [8] a novel joint bit and power allocation algorithm is proposed, which operates in fading environments and used to maximize the throughput and minimize the total transmit power, subject to a constraint on the average Bit Error Rate (BER). In [9] a dual methods based on Lagrangian relaxation are proposed, which are used to solve multiuser multicarrier resource allocation problem.

Optimal greedy power allocation already yields optimal solution for this problem [10], which can maximize the overall bit rate with the set of constraints at the expense of computational complexity [11]. Such constraints include total available power budget, number of subcarriers, target BER and QAM modulation orders. The solutions proposed in [13]–[16] are modified from the greedy algorithm, which reduce computational complexity.

In this article a new optimal Subcarrier Gain Based Power Allocation (SGPA) algorithm is introduced. This solution can decrease computational complexity and allows to achieve maximum bit rate over number of subcarriers with the same set of constraints. SGPA distributed the power among the subcarriers according to its gain. The excess (unused) power after the subcarrier gain allocation is redistributed again to reach maximum bit rate.

The rest of the paper is organized as follows. In Section 2, the standard greedy power allocation is reviewed. The proposed algorithms are presented in Section 3 and computational complexity is evaluated in Section 4. Simulation results are discussed in Section 5 and conclusions are drawn in Section 6.

2. The Greedy Algorithm

The OFDM system is characterized by an ISI channel H. The i-th subcarrier can be characterized by different gains $|H_i|,\ i = 1 \ldots N$, where N is number of subcarriers used to transmit number of bits equal b_i bits per symbol. The maximization of the sum bit rate can be defined by

$$\max \sum_{i=1}^{N} b_i . \tag{1}$$

Subjected to the constraint

$$\sum_{i=1}^{N} P_i \le P_{budget},\ \rho_{b,i} = \rho_b^{target},\ \text{and}\ \ b_i \le b^{\max},\ \forall i, \tag{2}$$

where P_i is the amount of power allocated to the i-th subcarrier, P_{budget} is the total power budget, $\rho_{b,i}$ is achievable BER of i-th subcarrier, which assume to be equal to target BER (ρ_b^{target}) and $b^{\max}$ is the maximum number of permissible bits allocated to a subcarrier. The carrier to noise ratio of the i-th subcarrier is given by

$$CNR_i = \frac{|H_i|^2}{N_0}, \tag{3}$$

where N_0 is the total power noise at receiver. The SNR of this subcarrier is

$$\gamma_i = P_i \times CNR_i. \tag{4}$$

Assume M-ary QAM modulation of order by M_k and $1 \le k \le K$ are the QAM levels, which is given by [11]

$$M_k = 2^{b_k} \quad \text{for} \quad 1 \le k \le K, \quad \text{and} \quad M_k = 0 \quad \text{for} \quad k = 0. \tag{5}$$

The BER of this QAM modulation is [12]

$$\rho_b = \frac{1 - \left[1 - 2\left(1 - \frac{1}{\sqrt{M_k}}\right) Q\left(\sqrt{\left(\frac{3\gamma_i}{M_k - 1}\right)^2}\right)\right]}{\log_2 M_k}, \tag{6}$$

which Q is the well-known Q function and its inverse is Q^{-1}.

To achieve a throughput $b_k = \log_2 M_k$ with BER of ρ_b^{target} minimum SNR is required as

$$\gamma_k^{QAM} = \frac{M_k - 1}{3}\left[Q^{-1}\left(\frac{1 - \sqrt{1 - \rho_b^{target}\log_2 M_k}}{2\left(1 - \frac{1}{\sqrt{M_k}}\right)}\right)\right], \tag{7}$$

To perform greedy power allocation, Uniform Power Allocation algorithm (UPA) must be performed at first, which can be summarized as follows [11], [13], [14]:

- Allocate the power budget equally among all subcarrier. The SNR of subcarriers γ_i in Eq. (4) is given by
$$\gamma_i = P_i \times CNR_i = \frac{P_{budget}}{N} \times CNR_i; \tag{8}$$
- Calculate SNR of QAM levels γ_k^{QAM} for all M_k, $0 \le k \le K$ by using Eq. (7);
- Redistribute subcarriers according to their SNRs γ_i into QAM groups G_k, $0 \le k \le K$ bounded by QAM levels γ_k^{QAM} and γ_{k+1}^{QAM} such as
$$\gamma_i \ge \gamma_k^{QAM} \quad \text{and} \quad \gamma_i \le \gamma_{k+1}^{QAM}, \tag{9}$$
with $\gamma_0^{QAM} = 0$ and $\gamma_{k+1}^{QAM} = \infty$;
- Load all subcarrier with QAM orders M_k according to their γ_i in Eq. (4) then compute total allocated bits to all groups
$$B_u = \sum_{i=1}^{N} b_i^u = \sum_{i=1}^{N} \log_2 M_{ki}, \tag{10}$$
where the sub-index u represents UPA.

Then there would be some unused (excess) power

$$P_{ex}^u = \sum_{i=1}^{N} \frac{\gamma_i - \gamma_i^{QAM}}{CNR_i} = P_{budget} - \sum_{i=1}^{N} \frac{\gamma_i^{QAM}}{CNR_i}, \tag{11}$$

and the power used in UPA is

$$P_{used}^u = P_{budget} - P_{ex}^u. \tag{12}$$

After this step GPA can be applied [11], [13]–[19], which performs an iterative redistribution of the excess power of UPA on all subcarriers. At each iteration, the Algorithm 1 tries to increase bit rate by upgrading the subcarrier of the least require power to the next higher QAM level [11], [13]. It stops when the remaining power of excess power cannot raise any subcarrier to the next level.

Algorithm 1: GPA

Initialization:

Initiate power for GPA to $P^{gpa} = P_{ex}^u$ in (11)
For each subcarrier i do the following:
Set $b_i^{gpa} = b_i^u$ in (10) and $k_i = k$ in (9)
Calculate the minimum required upgrade power:
$P_i^{up} = \frac{\gamma_{k_i+1}^{QAM} - \gamma_{k_i}^{QAM}}{CNR_i}$

Recursion:

While $P^{gpa} \ge \min(P_i^{up})$ and $\min(k_i) \le K$, $1 \le i \le N$
  $j = \arg\min_{1 \le i \le N}(P_i^{up})$
  $k_j = k_j + 1$, $P^{gpa} = P^{gpa} - P_j^{up}$
 If $k_j = 1$
  $b_j^{gpa} = \log_2 M_1$, $P_j^{up} = \frac{\gamma_2^{QAM} - \gamma_1^{QAM}}{CNR_i}$
 else if $k_j < K$
  $b_j^{gpa} = b_j^{gpa} + \log_2\left(\frac{M_{k_j}}{M_{k_j}-1}\right)$, $P_j^{up} = \frac{\gamma_{k_j+1}^{QAM} - \gamma_{k_j}^{QAM}}{CNR_i}$
 else
  $b_j^{gpa} = b_j^{gpa} + \log_2\left(\frac{M_{k_j}}{M_{k_j}-1}\right)$, $P_j^{up} = +\infty$
 end
end
Evaluate $B_{gpa} = \sum_{i=1}^{N} b_j^{gpa}$

3. The Proposed Algorithm

The proposed solution is referred to as Subcarrier Gain Based Power Allocation (SGPA) algorithm. It distributes the power according to subcarrier gain such that the higher gain subcarrier allocated higher power than the lower gain subcarriers. The total excess (unused) power that remains unallocated after that is redistributed to maximize the bit rate. The subcarrier gain based allocation is performed by the following procedure:

- Calculate the weight factor according to subcarrier gain

$$w_i = \frac{|H|}{\sum_{i=1}^{N} |H_i|}. \tag{13}$$

- Calculate the power of each subcarrier, which is given by

$$P_i = P_{budget} \cdot w_i. \tag{14}$$

- The SNR of subcarrier in Eq. (4) is

$$\gamma_i = P_i \cdot CNR_i = P_{budget} \cdot w_i \cdot CNR_i. \tag{15}$$

- Reside subcarriers according to their SNR γ_i into QAM groups G_k, then total allocated bits according to Eq. (10) is

$$B_w = \sum_{i=1}^{N} b_i^w = \sum_{i=1}^{N} \log_2 M_{ki}, \tag{16}$$

where sub-index w represent allocating power according to weight factor.

The unused (excess) power according to Eq. (11) is

$$P_{ex}^w = \sum_{i=1}^{N} \frac{\gamma_i - \gamma_i^{QAM}}{CNR_i} = P_{budget} - \sum_{i=1}^{N} \frac{\gamma_i^{QAM}}{CNR_i}. \tag{17}$$

The used power for SGPA algorithm is given by

$$P_w^{used} = P_{budget} - P_{ex}^w. \tag{18}$$

3.1. Excess Power Redistribution Mechanisms of SGPA Algorithm

This algorithm is simpler than GPA, which can reduce the complexity. It redistributes the excess power P_{ex}^w after subcarrier gain allocation to raise each subcarrier power to reach the next higher QAM level (upgrade each subcarrier one level up). This process performed over number of iteration (cycles) and stops when the remaining power of excess power cannot raise any subcarrier one level up. This solution is shown in pseudocode as Algorithm 2 and the resulting system throughput (total allocating bits) B_{SGPA} is

$$B_{SGPA} = \sum_{i=1}^{N} b_j^{SGPA}. \tag{19}$$

4. Complexity Evaluation

The main objective of this work is to present a new algorithm, which can significantly reduce complexity compared to GPA. The computational complexities of both GPA and SGPA algorithms are presented in Table 1. The proposed SGPA algorithm upgrade each one of N-subcarriers one level up (N level upgrade for N subcarriers) in each do-while loops. Assumed that the two algorithms

Algorithm 2: SGPA

Initialization:

1 Initiate power for SGPA to $P^{SGPA} = P_{ex}^w$ in (17)
2 Initiate $b_i^{SGPA} = b_i^w$ in (16) and $k_i = k$ in (9)
3 Calculate $P_i^{up} = \frac{\gamma_{k_j+1}^{QAM} - \gamma_{k_j}^{QAM}}{CNR_i}$

Recursion:

4 While $P^{SGPA} \geq \min(P_i^{up})$ and $\min(k_i) < K$, $1 \leq i \leq N$
5 For $j = 1 : N$
6 if $P^{SGPA} > P_j^{up}$
7 $P^{SGPA} = P^{SGPA} - P_j^{up}$, $k_j = k_j + 1$
8 if $k_j = 1$
9 $b_j^{SGPA} = \log_2 M_1$, $P_j^{up} = \frac{\gamma_2^{QAM} - \gamma_1^{QAM}}{CNR_i}$
10 else if $k_j < K$
11 $b_j^{SGPA} = \log_2\left(M(k_j)\right)$, $P_j^{up} = \frac{\gamma_{k_j+1}^{QAM} - \gamma_{k_j}^{QAM}}{CNR_i}$
else
12 $b_j^{SGPA} = \log_2\left(M(k_j)\right)$, $P_j^{up} = +\infty$
end
end
end
end

Evaluate $B_{SGPA} = \sum_{i=1}^{N} b_j^{SGPA}$

GPA and SGPA will perform the same number of one level upgrade L_1 then the quantity L_1 denote the average number of iterations of one do-while loop for the GPA (one level power upgrade in each loop) and $L_2 = int\left(\frac{L_1}{N}\right)$ is the average number of iterations of one loop for the SGPA. In each loop, the SGPA algorithm will perform N one level power upgrade (one level upgrade for N subcarrier) but, the GPA algorithm will perform one level power upgrade for one subcarrier. In addition, the SGPA algorithm will actually require lower average number of iteration of the loop to efficiently redistribute the excess power but, the GPA algorithm require larger average number of iteration of while loop to efficiently redistribute the excess power. The redistribution of the excess power can be performed with subcarrier ordering according to subcarrier gain such that the power upgrade process start with higher gain subcarrier first. The SGPA algorithm leads to reduce the computational complexity than GPA algorithm as shown in Table 1.

From Algorithm 2, the number of operation of the SGPA algorithm that shown in Table 1, can be calculated as:

At Line 1 one operation is performed. At Line 2 2N-operations are performed and at Line 3 N-operation is performed. So the number of instruction before starting loop equals $(3N+1)$. While loop at Line 4 has two 2N-operation conditions. At step (5) there is for-loop, which all the operations inside it, from step (6) to step (12) is repeated N-times. In step (6) there is if condition which perform one operation and if it true, step (7) can be performed

Table 1
Computation complexity for both GPA and SGPA

Algorithm	Number of while loop	Number of operation
GPA	L_1	$L_1(2N+7)+4N+1$
SGPA (no order)	$L_2 \approx int\left(\frac{L_1}{N}\right)$	$L_2(9N)+4N+1 \approx int\left(\frac{L_1(9N)}{N}\right)+4N+1$
SGPA (order)	$L_2 \approx int\left(\frac{L_1}{N}\right)$	$L_2(9N+1)+4N+1 \approx int\left(\frac{L_1(9N+1)}{N}\right)+4N+1$

with two instructions. In step (8) there is if condition which perform one operation and if it is true step (9) can be performed with two instructions. Else, steps (10) (one instruction) and step (11) (two operations) can be performed or step (12) (two operations) can be performed. So the number of operations inside for-loop, from step (6) to (12) equals 7 most. In addition to 2N-operations in step (4), so the of operations inside do-while loop equals $2N+7N=9N$. At step (13), N-operations are performed. So the number of operations for the SGPA (no order) equals $(L_2(9N)+4N+1)$ and for the SGPA (order) equals $(L_2(9N+1)+4N+1)$, which add one operation inside do-while loop because of ordering the subcarriers according to its gain.

5. Simulation Results

Assume that a 32-subcarrier OFDM system is characterized by an ISI channel H where the entries of H are complex Gaussian random variables with zero mean and unit-variance. Fixed QAM modulation orders of $\{2^1, 2^2, \ldots, 2^{b_{\max}}\}$ where $b_{\max}=8$ bit are considered and target BER = 10^{-3}. The overall system throughput (total allocating bits) is studied and shown in Fig. 1 which shows that the performance of GPA and SGPA (order) are identical at low SNR (0 to 8 dB) which provide the same throughput but SGPA (no order) provides slightly lower throughput. At medium SNR (15 to 35 dB) GPA provides slightly higher throughput than SGPA (order and no order) by approximately 10 bits. At high SNR (>38 dB), both the GPA, and SGPA algorithms provide the same throughput and achieve the maximum throughput of 256 bits/symbol (32 subcarriers $\cdot$ 8 bits) as the SNR become greater than 45 dB.

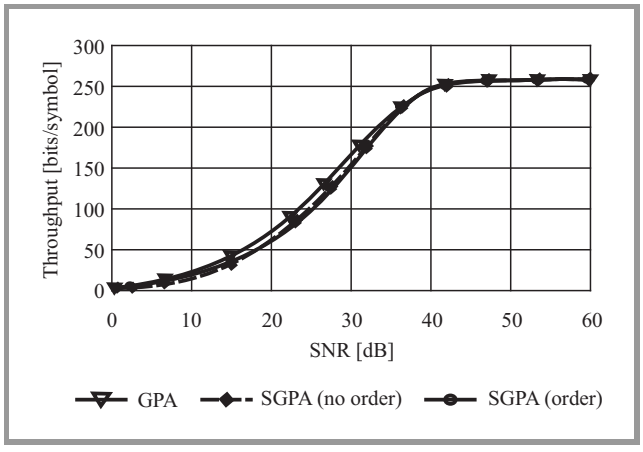

Fig. 1. Throughput for 32 subcarriers OFDM system with varying SNR and $\rho_b^{target}=10^{-3}$.

To demonstrate efficiency of the proposed scheme, the average run time of both GPA and SGPA algorithms for a 1024 subcarrier at different SNRs values is calculated, which is illustrated in Table 2. These algorithms were run on Intel Core i3 2 GHz PC with Windows 7 and MATLAB program 7.8.0. It is clear that GPA run time significantly increase with SNR and allocated power together with the number of operation (for each while loop upgrade one subcarrier one level up). On the other hand SGPA run time slightly increase due to reduced complexity (for each while loop approximately upgrade N-subcarrier N-level up).

Table 2
Calculation of average run time for both GPA and SGPA algorithms

	Average run time [μs]		
Algorithm	SNR = 15	SNR = 30	SNR = 45
GPA	2.79	20.6	23.6
SGPA (no order)	0.064	0.090	0.112
SGPA (order)	1.93	2.03	2.41

Figure 2 shows the average number of times to get into the while loops to perform the process of excess power redistribution that used in SGPA algorithm compared to the standard GPA for 32 and 256 subcarriers with varying SNR. The getting into while loop stops when the remaining excess power can't raise any subcarrier on level up. In addition, the average number of while loop for the standard GPA algorithm proportionally increases with the number of subcarriers because within the one while loop, GPA raise one subcarriers one level up. On the other hand the average number of while loop for the SGPA algorithm is approximately independent on the number of subcarriers because within the one while loop, SGPA can raise all the N-subcarriers one level up. The SGPA algorithm

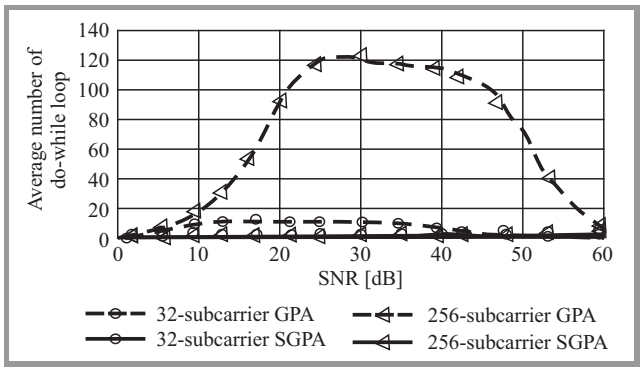

Fig. 2. Counting the average number of times of getting into do-while loop in GPA and SGPA for 32 and 256 subcarriers OFDM system with varying SNR.

has a significantly smaller average number of while loop for different number of subcarriers compared to the standard GPA algorithm. From all, the SGPA algorithm provides optimal performance in bit rate maximization and lower computational efficiency for different SNR values than GPA algorithm.

6. Conclusions

The optimum solution of maximum bit rate with minimum power is provided by greedy algorithm. However, it requires a high computational complexity. Therefore, SGPA algorithm is proposed which provides optimal performance in bit rate maximization and considerably reduces the computational efficiency compared to GPA solution.

References

[1] A. Falahati and M.-R. Ardestani, "Adaptive subcarrier assignment and power distribution in multiuser OFDM systems with proportional data rate requirement", *Iranian J. Electrical & Electronic Engin.*, vol. 4, no. 1 & 2, pp. 10–16, 2008.

[2] T. M. Cover and J. A. Thomas, *Elements of Information Theory*. Wiley, 2006.

[3] H. Al-Shatri and T. Weber, "Fair power allocation for sum-rate maximization in multiuser OFDMA", in *Proc. Int. ITG Worksh. Smart Antennas WSA 2010*, Bremen, Germany, 2010, pp. 350–354.

[4] H. Yin and H. Liu, "An efficient multiuser loading algorithm for OFDM-based broadband wireless systems", in *Proc. IEEE Global Telecommun. Conf. GLOBECOM 2000*, San Francisco, CA, USA, 2000, vol. 1, pp. 103–107.

[5] W. Rhee and J. M. Cioffi, "Increase in capacity of multiuser ofdm system using dynamic subchannel allocation", in *Proc. 51st IEEE Vehicular Technol. Conf. VTC 2000-Spring*, Tokyo, Japan, pp. 1085-1089, 2000.

[6] S. W. Ko, and S. L. Kim, "Block waterfilling with power borrowing for multicarrier communications", in *Proc. 68th IEEE Vehicular Technol. Conf.*, Calgary, Canada, 2008, pp. 1–5.

[7] H. W. Lee and S. Chong, "Downlink resource allocation in multicarrier systems: Frequency-selective vs. equal power allocation", *IEEE Trans. Wirel. Commun.*, vol. 7, no. 10, pp. 3738–3747, 2008.

[8] E. Bedeer, O. A. Dobre, M. H. Ahmed, and K. E. Baddour, "Joint optimization of bit and power allocation for multicarrier systems with average BER constraint", in *Proc. 76th IEEE Vehicular Technol. Conf. VTC Fall 2012*, Quebec, Canada, 2012.

[9] S. Gortzen and A. Schmeink, "Optimality of dual methods for discrete multiuser multicarrier resource allocation problems", *IEEE Trans. Wirel. Commun.*, vol. 11, no. 10, pp. 3810–3817, 2012.

[10] M. Bohge and J. Gross, "Dynamic resource allocation in OFDM systems: an overview of cross-layer optimization principles and technique", *Network*, *IEEE*, vol. 21 no. 1, pp. 53–59, 2007.

[11] W. Al-Hanafy, M. N. Hussin, and S. Weiss, "Incremental rate maximization power loading with BER improvements", in *Proc. 18th Eur. Sig. Proces. Conf. EUSIPCO 2010*, Aalborg, Denmark, 2010, pp. 382–386.

[12] A. Goldsmith, *Wireless Comunication*. Cambridge University Press, 2005.

[13] W. Al-Hanafy and S. Weiss, "Reduced complexity schemes to greedy power allocation for multicarrier systems", in *Proc. 18th Int. Conf. Microw. Radar Wirel. commun. MIKON 2010*, Vilnius, Lithuania, 2010, pp. 1–4.

[14] N. A. Odhah, M. I. Dessouky, W. AI-Hanafy, and F. E. Abd EI-Samie, "An improved adaptive transmission scheme for high speed communication systems", in *Proc. Int. Computer Engin. Conf. ICENCO 2010*, Giza, Egypt, 2010, pp. 29–33.

[15] N. A. Odhah, M. I. Dessouky, W. AI-Hanafy, and F. E. Abd EI-Samie, "Low complexity precoded greedy power allocation algorithm for OFDM communication systems", *J. Sig. Inform. Proces.*, vol. 3, no. 2, pp. 185–191, 2012.

[16] N. A. Odhah, M. I. Dessouky, W. AI-Hanafy, and F. E. Abd EI-Samie, "Low complexity greedy power allocation algorithm for proportional resource allocation in multi-user OFDM systems", *J. Telecommun. Inform. Technol.*, no. 4, pp. 38–45, 2012.

[17] J. Campello, "Optimal Discrete Bit Loading for Multicarrier Modulation Systems", in *Proc. IEEE Int. Symp. Inform. Theory*, Cambridge, MA, USA, 1998, p. 193.

[18] J. Campello, "Practical bit loading for DMT", in *Proc. IEEE Int. Conf. Commun. ICC'99*, Vancouver, Canada, 1999, vol. 2, pp. 801–805.

[19] N. Papandreou and T. Antonakopoulos, "Bit and power allocation in constrained multicarrier systems: the single-user case", *EURASIP J. Adv. Sig. Proces.*, vol. 2008, pp. 1–14, 2008.

Mohammed Abd-Elnaby received the B.S.(Hons.), M.S., and Ph.D. degrees in Electronic Engineering from Menoufia University, Menouf, Egypt in 2000, 2004 and 2010, respectively. Currently, he is working as lecturer at the Department of Electronics and Electrical Communication, Faculty of Electronic Engineering, Menoufia University, Menouf, Egypt. His research interests include wireless networks, wireless resource management, MAC protocols, cognitive radio, and cooperative communication.

E-mail: moh_naby@yahoo.com
Faculty of Electronic Engineering
Menoufia University
Menouf, 32952, Egypt

Germien G. Sedhom received the B.Sc. from the Faculty of Electronic Engineering, Menoufia University, Menouf, Egypt in 2009. She is currently working towards the M.Sc. degree. Currently, she is working as a demonstrator in the Department of Communications in Delta Higher Institute for Engineering and Technology, Delta Academy, Mansoura, Egypt. Her research area of interest includes Dynamic Resource Allocation in Multicarrier Systems.

E-mail: germien_ggs@yahoo.com
Faculty of Electronic Engineering
Menoufia University
Menouf, 32952, Egypt

Fathi E. Abd El-Samie received the B.Sc.(Hons.), M.Sc., and Ph.D. degrees from Menoufia University, Menouf, Egypt, in 1998, 2001, and 2005, respectively. Since 2005, he has been a Teaching Staff Member with the Department of Electronics and Electrical Communications, Faculty of Electronic Engineering, Menoufia University. He is currently a researcher at KACST-TIC in Radio Frequency and Photonics for the e-Society (RFTONICs). He is a co-author of about 200 papers in international conference proceedings and journals, and four textbooks. His current research interests include image enhancement, image restoration, image interpolation, super-resolution reconstruction of images, data hiding, multimedia communications, medical image processing, optical signal processing, and digital communications.

E-mail: fathi_sayed@yahoo.com
Faculty of Electronic Engineering
Menoufia University
Menouf, 32952, Egypt

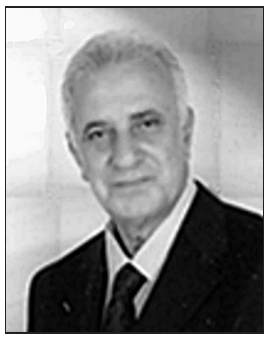

Nagy Wadie Messiha received the Ph.D. degree in Electrical Engineering from the Institute of Switching and Data Techniques, Stuttgart University, Germany, in 1981. He is a co-author of about 40 papers in national and international conference proceedings and journals. Now he is a Professor in the department of Electronics and Electrical Communication Eng., Faculty of Electronic Eng. His research interest includes computer communication networks and developments of security over wireless communications networks, and encryption algorithms.

E-mail: Dr.nagy_wadie@hotmail.com
Faculty of Electronic Engineering
Menoufia University
Menouf, 32952, Egypt

Xu Zhu received the B.Eng. degree (with first class honors) in Electronics and Information Engineering from Huazhong University of Science and Technology, Wuhan, China, in 1999, and the PhD degree in Electrical and Electronic Engineering from the Hong Kong University of Science and Technology, Hong Kong, in 2003. Since May 2003, she has been with the Department of Electrical Engineering and Electronics, the University of Liverpool, Liverpool, UK, where she is currently a senior lecturer. Dr. Zhu has over 100 peer-reviewed publications in highly ranked international journals and conference proceedings in communications and signal processing. She is an associate editor for the IEEE Transactions on Wireless Communications, and has served as a guest editor for three international journals such as Computer Science and Information Systems. She was vice chair of the 2006 and 2008 ICARN International Workshops, Program Chair of the ICSAI 2012, and Publication Chair of the IEEE IUCC-2012. Her research interests include wireless MIMO systems, equalization, OFDM techniques, resource allocation, cooperative communications, cross-layer design, cognitive radio, smart grid communications etc.

E-mail: xuzhu@liverpool.ac.uk
Department of Electrical Engineering and Electronics
The University of Liverpool
Merseyside L69 3GJ, Liverpool, UK

Paper

Gyrotron Technology

Mariusz Hruszowiec, Wojciech Czarczyński, Edward F. Pliński, and Tadeusz Więckowski

Terahertz Technology Center, Wrocław University of Technology, Wrocław, Poland

Abstract—The article presents a microwave vacuum tube called gyrotron. Its applications, construction and principle of operation are briefly described. It is also discussed the issue of an appropriate electron beam generation and formation.

Keywords—beam gun, gyrotron, interaction of electrons with fast wave, microwaves.

1. Introduction

Microwave vacuum tubes are devices used for generation or amplification of the microwaves [1]–[13]. Microwaves cover a large part of the electromagnetic spectrum, and at the same time there are only a few kinds of devices operating in this frequency band, capable of operating with high power. This group includes amplifying devices, such as traveling-wave tubes (TWT), klystrons, gyro-TWTs, gyro-klystrons and other. The generators are magnetrons, backward wave tubes (BWO), gyrotrons and other. Currently, the microwave vacuum devices are almost exclusively designed for amplification and generation of large and very large RF signals. While the range of centimetre waves and average power are dominated almost entirely by semiconductor devices, the high-output power ones, especially in the millimetre range, are still the domain of vacuum devices. Another advantage of vacuum tubes over semiconductor equipment is high efficiency, as yet unavailable for semiconductors.

History of the microwave tubes dates back more than a century, but it was during the Second World War when their role has become so important. Magnetrons and klystrons were used to build the radars. The traveling-wave tube, which was invented during the war, has been applied mainly in may military and communication systems.

The development of semiconductor technology has slowed down the development of microwave tubes. It was thought (70s of the 20th century), that vacuum tubes would be completely replaced by solid-state devices. Unexpectedly, this trend has changed in the beginning of the 90s, when it turned out that in satellite communication the TWT tubes are better than semiconductor devices [14]. In the same time the improvement of gyrotron, the device that has been invented a few years earlier, was impressive. This new tube has an important advantage, namely the area where interaction of electromagnetic wave and electron beam occurs is of simple geometry and does not require delay line with structure dimensions proportional to the wavelength as in devices such as klystron, magnetron or TWT. The delicate structure of the delaying lines and resonators limited their use at higher frequencies and high power levels. An additional advantage is the relatively high efficiency, which is being improved every year [18]–[21]. In addition, another factor that caused the big return of microwave vacuum tubes technology, was the power they can generate, especially in wavelength of millimetre waves. The power generated by gyrotron tubes may be several orders of magnitude greater than the power of a devices based on semiconductor structures.

2. A Brief History of Gyrotron

The operation of the device called a gyrotron is based on a phenomenon known as the ECR (Electron Cyclotron Resonance), instability of relativistic rotating electrons during the interaction, in a constant magnetic field, with an electric field of the electromagnetic wave [15]–[17], [23]. Theoretical work on this phenomenon was started by Twiss in Australia [24], Schneider in the USA and Gaponov in the USSR [25] in the late 50s. The first experiments were carried out and the results published by Gaponov and Pental in the 1959 [26]. Then the results of several experiments were mainly published by a group of scientists from the USA and the USSR [27]–[29]. The first working gyrotron was constructed by Hirshfield and Wachtel in 1964. The gyrotron with an annular magnetron electron gun with the adiabatic compression of the stream of rotating electrons and the cavity with smooth walls was invented in the Radio-Physical Institute, Gorki (now Nizhny Novgorod), in the USSR by Gaponov and Kiesel [27] in 1963. Figure 1 shows a scheme of the first gyrotron [16]. The output power of 6 W was obtained in the continuous work mode at the 10 GHz frequency. The use of a MIG (Magnetron Injection Gun) electron gun and a single cavity has delivered significant power output with a very good efficiency,

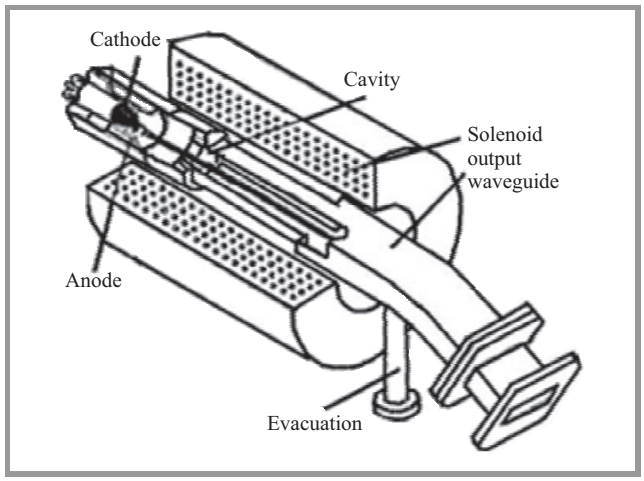

Fig. 1. Construction of the first gyrotron.

compared to the previous experiments. Later the new experiments were conducted with the gyrotrons working at higher harmonics and generating higher output power [16]. In the years 1970–1980 a significant progress was has been done, both in the theoretical and experimental field, including the theory of gyrotron and other devices based on extracting energy from the gyrating electrons, such as gyro-klystron, gyro-TWT, etc. There were also other experiments conducted in order to improve both the efficiency and the output RF power. They were focused mainly on the proper profiling of the cavity (area of interaction), elimination of the parasitic oscillation, increasing the work frequency and the development of tunable gyrotrons [30]–[34]. The use of helical output launcher developed by Vlasow in 1975 allowed the conversion of multimode wave into a Gaussian distribution mode [35]. In the 80s the work on gyrotrons has been started in many other countries such as Brazil, Korea, France, Japan, Australia and Germany. In the years 1990–2000 a significant development of terahertz and coaxial gyrotrons was done. During this period, the FZK Karlsruhe team, working for the ITER project has made the most significant progress [36]. Extensive investigation and production activities were carried out in USA, Japan and Russia. At present more countries like India and China, have started to work on their own gyrotrons. We expect that in the near future, Poland will also join this elite club. Initial research has already been done by the Wrocław Terahertz Team [37].

3. Applications

Gyrotron has found many applications in many different areas such as communication, military applications (from radar to missile guidance systems), science (elementary particle acceleration, thermonuclear plasma devices, diagnostics), industry (heating, processing of different materials, e.g. ceramics) and in medicine, i.e. innovative methods of cancer therapy, high power terahertz radiation [38]. Some of these applications will be briefly presented below.

3.1. Communication

Because of the considerable attenuation of electromagnetic radiation in the Earth's atmosphere along with the increase of the wave frequency, the present communication systems need to be improved in order to continue their tasks, including future demand for quick transfer of very large data quantities. Future microwave systems should also be able to generate high power required by the radar systems working in the millimetre wave regime, providing long range and high resolution. Microwave tubes, and in particular the gyrotrons that work at high frequencies, are among a few devices that can be used in these applications. In addition, these devices can provide microwave power for radars tracking space junk, as well as for georadars, which detect the underground structures, such as bunkers, mines, pipes, and other. Additionally, the latest terahertz gyrotrons can generate teraherz frequencies radiation, which in turn can be used for inter-satellite communication (due to the wide bandwidth) and for communication at short distances, which can be very useful in military applications.

3.2. Defence Applications

The gyrotron that works on the frequency of 95 GHz and with output power of 100 kW was used as a source of millimetre radiation for ADS (Active Denial System). The ADS System was developed by Raytheon for the U.S. Army Air Force. It is a not lethal, anti-personnel, weapon that uses the directed energy. Officially published data provide information about effective coverage within the limits up to 1 km. The available materials about the ADS reveal the frequency of work to be 95 GHz, probably chosen because of a natural window of low atmosphere attenuation in this frequency range. The depth of skin penetration of the wave of this frequency range is about 0.4 mm and after 2 seconds causes rise of the water temperature in upper layer skin up to 50–60°C, causing a hard to stand feeling of pain. Turning off the beam causes almost immediate relief of symptoms. The exposure of skin causes no permanent effects, but the beam of sufficient power and duration can cause eye damage and even second degree burns. Published data show that the effective power density is approximately 2 W/cm^2. The countermeasures are very simple, the thicker layer of clothing or metal foil [39]. There is no data on the effectiveness of that weapon in the rain, fog or snow. Local conditions, including climate, resulted in the withdrawal of ADS from Afghanistan in 2010 without its use. In the year 2010 the Los Angeles police (USA) was equipped with such weapon for tests [41].
The millimetre wave radars were developed, which allow to obtain high location resolution of tracked objects [42]. In addition, thanks to the gyro-sources, the effective range rises up to several hundred kilometres, which is a remarkable result especially together with high resolution imaging. Currently such radars are working in Russia and in USA. The Russian installation consists of a matrix of 120 antennas, works at 34 GHz frequency. It is fitted with two gyro-klystrons, 0.5 MW output power, bandwidth of 50 MHz, and the duration of the pulse of 100 μs each. The American installation is based on the gyro-klystron that works at 94 GHz (92 kW of output power) with about 420 MHz bandwidth [43].

3.3. Meteorology

A high power signal of a millimetre wave can be easily used in all kinds of research concerning the structure and behaviour of the Earth atmosphere e.g. monitoring of clouds, humidity measurement, detection and identification of turbulence structures and other [44]–[46]. Radar systems operating at the frequency of 35 GHz and 94 GHz can easily be used to detect turbulence. In addition, the teraherz radiation can be used to study the water content in the atmosphere [48].

3.4. Defense of the Planet

Another possible application of the source of high power teraherz radiation is monitoring of the outer space. It is becoming more and more polluted by various types of space garbage and waste (old satellites, rocket modules, components, etc.), which are becoming a serious problem for the active satellites and other space vehicles. Because space debris detection and accurate maps of their orbits become necessary in order to ensure an appropriate level of security. For the system, which has been proposed by Chang and other, it is estimated that for detection of an object of 1 cm size at a distance of 1000 kilometres, the 20 MW signal and antenna with a diameter of 20 metres are needed [49]. Gyrotrons that work in the regime of 35 GHz are currently the best sources of radiation needed for detection of space debris.

3.5. The Topography of the Planet, Maps

The radiation of millimetre wavelength could be used to prepare topological maps of the planets [50]. The radiation beam would be focused on the surface of the planet, while the scattered radiation, depending on the topography of the area, would be detected by the radar system. As a source of radiation a miniature gyrotron could be used.

3.6. Security

A possible use of the gyrotron is the remote detection of various undesirable substances. The radiation has got already a number of applications, with the ability to penetrate a non-conductive and non-polar materials such as clothing, paper, wood and other. Such properties of terahertz radiation makes it suitable for applications in the area of public security, e.g., already operating scanning systems in airports or envelope content inspection systems [51]–[52].
An experiment was conducted, in which the radioactive substance was remotely detected using a specially designed gyrotron (670 GHz, 300 kW). The method was based on focusing the beam of THz radiation (produced by the gyrotron) on a small area (point), in which the amplitude of the electromagnetic field could exceed the discharge threshold and caused the air breakdown. Such a system may be used for remote detection of radioactive materials e.g. in containers or vehicles. This makes a new application field of both (sub)terahertz radiation, and the gyrotron as a source of this radiation [53].

3.7. Scientific Applications

The demand for the high power and high frequency radiation sources has been present from the beginning of modern science, particularly in physics of elementary particles and in fundamental research. Recent years have shown that especially applications in plasma and nuclear fusion research require dynamic development of the gyrotron technology. In many various tokamaks around the world, are already working the first gyrotrons. The gyrotron plays a very important role in plasma research already for the last 30 years. The latest international programme focused on the creation of the reactor capable to carry controlled nuclear fusion is the ITER programme. This programme is the largest one in progress, where gyrotrons will be working with the 170 GHz frequency and generating output power of 1 MW. High output power, high efficiency and long pulse of generated radiation are key requirements for gyrotrons in ITER project.
Another area of application of the radiation generated by the gyrotrons are the different techniques of investigation of structure of materials. One of these techniques is electron spin resonance (ESR), as a tool for studying of material microstructures [54]. Currently, this technique is used in the X-ray band, however thanks to the strong sources of terahertz radiation it is possible to use it for investigations of materials with a very short relaxation time.
The large terahertz signal is required in the dynamic nuclear polarization used together with the nuclear magnetic resonance (NMR/DNP) [54]. The nuclear magnetic resonance (NMR) uses strong pulse of electromagnetic radiation, which is then tested in terms of emission and absorption. The disadvantage of this method is the very low level of the recorded output. To increase the efficiency of NMR a phenomenon of electron spin transfer into the nucleus is used (Dynamic Nuclear Polarization, DNP). NMR is a very powerful tool in the bio-molecular analysis of protein and peptides structures. NMR/DNP spectroscopy in low magnetic fields is used to study polymers. On the other hand, for biological molecules (proteins) a strong magnetic field is required. For NMR/DNP that uses strong magnetic fields, high frequency and long radiation pulses, the low power gyrotrons are used as teraherz radiation sources.
The mentioned improvements of the classic diagnostic methods may be also applied in the future medical diagnostics. Other medical applications (e.g. therapeutic applications) are being examined. Presently there is an ongoing development of new hybrid therapy against cancer [55]. THz radiation, generated by continuous-wave gyrotron was used. The frequency range was from 200 GHz to 305 GHz, with the maximum power of up to 20 W. The tests, which were performed on laboratory mice gave the positive results, the growth of cancer cells after exposure to the radiation was stopped [54], [55].

3.8. Industrial Applications

In metallurgy applications microwave radiation in the range from 300 MHz to 300 GHz is mainly used for heat treatment of materials. Microwave heating is used in the processing of rubber, ceramics sintering, technology of chemical processes, production of composites, food industry. In some applications the millimetre waves have better properties than the centimetre ones. They are used in the following types of heat treatments: strengthening of surface, drying, removal of organic binders and moisture from the ceramics surface, growing of ceramic nanostructures. The

gyrotron, is able to provide output power ranging from hundreds of kilowatts to several megawatts in the regime of millimetre wavelength. Gyrotrons may be installed inside the final devices because of high stability of generated frequency and power level. The millimetre waves in material heating surpass the use of centimetre waves in some applications because attenuation of electromagnetic radiation in dielectric materials increases with frequency and the heating efficiency is better than for centimetre waves. Due to the shorter wavelength the depth of penetration is smaller and the incident radiation power is lost in the shorter depth, allowing the near surface treatment of the material.

4. The Construction and Method of Operation

The gyrotron in its basic configuration consists of the following parts: the source of the electron beam (electron gun), magnets or solenoids producing a static magnetic field, cavity, output circuit and collector. As the output system a special launcher with set of mirrors can be used, in order to guide the electromagnetic wave perpendicular to the axis of the gyrotron or along with main axis of the tube using a special electron collector ended with a in-axis vacuum-tight window, which transmits the output signal out of the tube. A schematic diagram of the gyrotron is presented in Fig. 2. The annular electron beam is generated by an annular magnetron electron gun. The external magnetic field, usually generated by a liquid nitrogen cooled solenoid or superconducting one. The magnetic field increases gradually from low value at the emitting cathode surface (should be almost parallel to the surface to obtain a quasi laminar electron beam) to the value required for the desired cyclotron frequency. The increase of magnetic field causes compression of the average diameter of the annular beam. The maximum magnetic field occurs in the region of the resonance cavity, and its value (together with the accelerating voltage of electrons) specifies the electron cyclotron frequency and thus the tube frequency of operation. The relationship between the wavelength, magnetic field and voltage is given by the formula:

$$B\ [\mathrm{T}] = 10.7\gamma/s\lambda\ [\mathrm{mm}]\,, \tag{1}$$

where $\gamma = 1 + \mathrm{V}$ [kV]/511 is the relativistic Lorentz factor, s is harmonic number of operation, λ is the wavelength in millimetres [56]. It follows that for a wavelength below 1 mm at the fundamental harmonic and with accelerating voltage of 50 kV, the magnetic field must exceed 10 T. To obtain such high fields the use of a superconducting solenoid is required. To reduce the requirements for magnetic field, higher harmonics are often used, at some expense of efficiency. However, achievable conversion efficiency for the second harmonic can be even 35% [57].

Rotating electrons move to the cavity into the electron-wave interaction area. In this area the electrons are retarded by the electric field of the electromagnetic wave, thus a portion of their energy is transferred to the electromagnetic (EM) wave. The magnetic field in the interaction area is chosen in such a way that the frequency of an electron cyclotron resonance, or one of its harmonics, close to the desired EM wave frequency. In axial gyrotron the electron beam is captured by the walls of a hollow coaxial collector, due to reduction of the axial magnetic induction (almost zero), while the electromagnetic wave is transmitted out of the tube through the axial vacuum-tight window at the end of waveguide collector section. In the radial type of the gyrotron output, the vacuum-tight window is perpendicular to the main gyrotron axis (Fig. 2) [58].

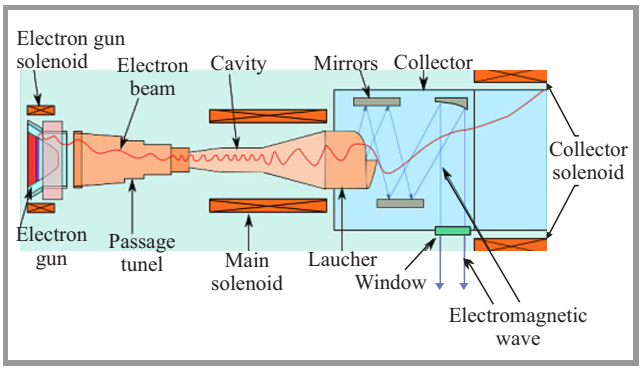

Fig. 2. Gyrotron sample construction scheme.

The main working component is the cavity, where the interaction of the beam of rotating electrons, and electromagnetic wave takes place. Usually it is an open round resonator with smooth walls, whose main section is ended on both sides by short sections with tapered diameters, causing partial reflections of electromagnetic wave [15]–[17]. The first section should present the reflection coefficient as high as possible, preventing passage of the EM wave back to the electron gun, whereas the output section should the reflection coefficient rather low. Beam-wave interaction occurs mainly in the central part of the resonance cavity, while the last section is used for coupling the cavity with a launcher or the output waveguides. Coaxial cavities are also used, because the distribution of electric field, associated with electron beam space charge, is more favourable. This allows for higher efficiency of energy transformation. However, the coaxial gyrotrons have more complicated structure of the electron gun.

The electron trajectories are helical with the axes of rotation along the lines of the static magnetic field. In order to extract energy from the rotating electrons and to transfer it to EM wave, the electrons should be focused in phase on their cyclotron orbits. Such focusing makes possible the net extraction of electron energy to the wave. To take benefit from such mechanism, it is required to satisfy the resonance condition between the periodic movements of electrons and EM wave in the interaction section, according to the following formula [15]–[17]:

$$\omega - k_z v_z = s\omega_c\,, \tag{2}$$

where ω is the EM wave frequency, k_z is the axial characteristic wave number, is the electron drift velocity, v_z is

harmonic number, and ω_c equation stands for the cyclotron electron frequency. Because of very high energy of the electron beam, the frequency shift occurs ($k_z v_z$), which is caused by the relativistic Doppler effect. In the gyrotron the electron drift velocity (v_z) is always lower than the transverse electron velocity, what causes that Doppler effect may be neglected. In such case the cyclotron resonance condition can be written down in the following way:

$$\omega \approx s\omega_c \,. \tag{3}$$

4.1. The Electron-optical System

The gyrotron electron-optical system consists of a launcher, tube tunnel and electron collector. Part of the tunnel tube is a cylindrical or coaxial resonator, where the electron beam is rotating around the main axis of the cavity.
A critical element of the gyrotron is the source of electrons, which should generate a laminar beam. The electron gun is of a magnetron injection type [59]. Two kinds of electron gun are used: a diode in the cathode-anode configuration and a triode in the cathode – modulating anode – anode configuration. Diode MIG launcher has a single anode and its construction is much simpler than the triode type, which has two anodes and requires two separated supplies and additional high voltage gun insulator. However, the use of modulation anode provides better control of the electron beam.

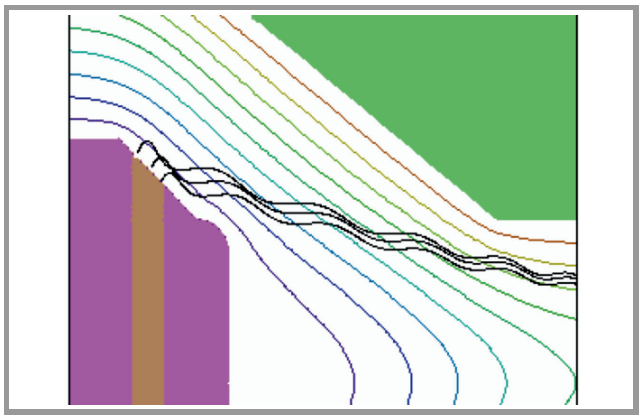

Fig. 3. Quasi-laminar electron trajectories in the magnetron injection gun. The cathode emission is confined by the space charge. $U_a = 55$ kV, $B_z = 4.3$ T. The electron trajectories are started from edges and centre of the emission layer.

Electrons emitted from the cathode are accelerated towards the anode, forming a beam of relevant parameters (Fig. 3) [37]. Magnetic field lines should be parallel to the electrons emitting surface. The increase of magnetic induction towards the cavity causes adiabatic compression of diameter of the electron beam in the tunnel between the electron gun and the cavity. The transmission tunnel is often equipped with damping elements to prevent a microwave signal from going back into the gun area. The external diameter of the gyrotron is determined by the maximum internal diameter of the magnetic system.

The ratio of the accelerating voltage to the magnetic field determines the cyclotron frequency and the ratio of radial velocity of the electron to its axial velocity, which is along the axis, around which the spiral movement occurs. The radial velocity of the electron determines the amount of possible extracted energy. However, the pursuit of excessive increase of it can lead to magnetic mirror formation and reflections of the electrons back into the source. The ratio of radial velocity to the axial velocity α is usually about 1.2. The trajectories of the electrons are helical along the magnetic field lines. The change of the magnetic field from B_0, at the cathode, to the $B_{\max}$ at cavity, is determined by $F_m = B_0/B_{\max}$, called magnetic field compression. This factor determines the change in diameter of a annular electron ring beam.

The function that describes the change of the magnetic field, $B_z = f(z)$ must comply with certain conditions (such as field lines must be approximately parallel to the emission surface), that is why the gyrotron electron gun is often equipped with a separate adjustment solenoids [60].

Because of the very important role of the electron gun, the effort was made to perform numerical simulations of such devices. Simulations were performed using the Amaze (Field Precision) set of codes for calculations of electric and magnetic static fields and electron trajectories. The simulated gun was a typical diode with a cathode and a single anode (Fig. 3), working in the space charge limited emission regime. The obtained results were quite promising. Simulated beam of electrons showed good laminarity. It is interesting because the electron guns that work in the temperature limited current mode are able to emit quasi-laminar beam easily, on the other hand emission from the

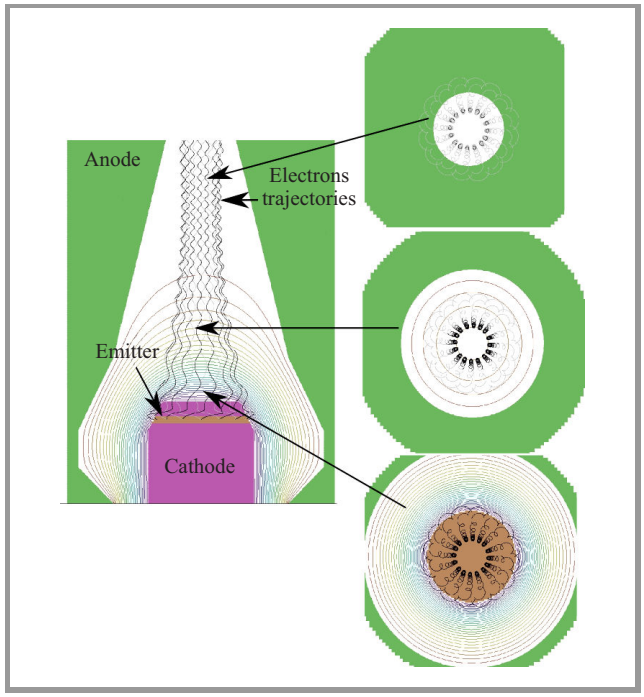

Fig. 4. The electron trajectories in magnetron diode gun. The 16 trajectories of 160 used in simulation are shown.

cathode that works in spatial charge mode is more uniform [61]. Figure 4 presents the electron trajectories in transverse planes in the tunnel as seen from the resonator side [37]. Note: Fig. 4 presents another configuration of the electrodes and fields than Fig. 3.

4.2. The Resonator

Construction of the resonator is very simple. It is a cylinder or section of a coaxial line. The resonator is ended on the side of the electron gun by a short tapered section, which has different impedance, causing reflection of electromagnetic wave. Because this kind of resonator ending does not cause complete reflection, the passage tunnel is usually fitted with means for suppressing of the EM signal in the direction of the electron gun. Attenuation is achieved by suitable design of the tunnel walls, by lining them with damping material or by both methods. The other end of the resonator is a funnel shaped transition section passing into the multimode waveguide. The reflection coefficient is sufficiently low to allow the flow of the generated signal. It should be noted that the reflection towards the cavity is not necessary for signal generation. From any point, where the exchange of energy between the electron and the electromagnetic wave occurs, the wave propagates in both directions, as in classic Backward Wave Oscillator (BWO), whose counterpart is the described type of gyrotron.

4.3. The Output System and the Collector

Two types of signal output systems are commonly used in gyrotrons. In the first type the resonator output is transformed into a circular waveguide, whose walls act simultaneously as collector of electrons. The magnetic field in this section should be reduced to zero. The electrons under the influence of the spatial charge and not focused by the magnetic field, are guided towards cooled walls of the waveguide. There is often an additional solenoid producing crossed magnetic field, which is directing the rest of electrons to the walls of the collector section of output waveguide. It is necessary for the protection of vacuum-tight window, closing the vacuum part of device. Even a minute electron bombardment of the dielectric window might initiate its destruction by the multipactor effect.
The second solution involves the guidance of the signal perpendicularly to the main axis of the gyrotron. The signal is directed from the waveguide following the resonator by means of the Vlasov launcher into the system of the transformation mirrors, that changes the multimode signal into a coherent one [62], [63]. It is directed by the vacuum-tight window to the receiver. The electrons in this solution are moving along the axis of the gyrotron into the collector, which is not the part of the waveguide, so it can be isolated and can be at lower potential than accelerating voltage. Such solution allows for partial energy recuperation and thus for improvement of the overall efficiency. The price for that is a complexity of the structure (additional high voltage insulator and additional high voltage collector supply). Such type of collector is commonly used in high power linear microwave tubes and satellite TWTs, whose the overall efficiency is an important parameter.
The microwave vacuum-tight windows, especially for the high power and for continuous wave may be quite a technological problem. The best (and the most expensive) are the diamond ones, primarily due to the high thermal conductivity of diamond. Usually the windows are cooled.

4.4. Magnet

As it is clear from Eq. (1), a gyrotron requires very strong magnetic fields, inversely proportional to the wavelength of the signal. These fields can, in extreme cases, reach up to 20 T. The medium size gyrotron that generates wave longer than 1 mm still requires several Tesla magnetic field. One of the solutions is to work with harmonics higher than the first one. High power gyrotrons, stationary and designed for work without interruptions, generally are fitted with magnets placed in cryostats and cooled with liquid nitrogen.
For stronger fields superconducting solenoids are used, placed in liquid helium. This solution excludes its application in mobile devices, because the usual practice is keeping the magnet in the cooled state. Preparation from ambient temperature to the work one requires many hours of cooling down and large amounts of liquid helium. Maintenance in a state of continuous readiness is also very expensive. The search for better solutions, especially for mobile applications, led to the development of solutions based on permanent magnets and classic solenoids. For few millimetre wavelengths liquid-cooled solenoids are successfully used. Pulsed solenoids are also tested. Presently the permanent magnets can generate magnetic fields just above 1 T in the volume of resonant cavity [64]. There are also reports on conventional solenoids that were able to produce 1.8 T and 2.1 T [57], [65]. The first of them was the solenoid made with copper foil, placed between liquid-cooled copper plates. The second solution was the solenoid made of copper tube, cooled with liquid.

4.5. Technology

Gyrotron technology does not much differ from the metal-ceramic tube technology of high power TWT and it does not present serious problems. Such technology is fully available in Poland.

5. Summary

The gyrotron undoubtedly is one of the most promising devices. It is currently the object of very extensive research around the world. The article mentions some possible applications of such devices. The principle of operation and construction has been described briefly. Particularly, attention was focused on the electron beam generation, and more specifically on magnetron electron guns.
The required parameters of the electron beam, formed by the electron gun in gyrotron, were described. The results

of simulations of the electron gun, intended for gyrotron application, first in Poland, have been presented.

References

[1] B. N. Basu, *Electromagnetic Theory and Applications in Beam-Wave Electronics*. Singapore: World Scientifc Publishing Co., 1996.

[2] A. W. H. Beck, *Space Charge Waves and Slow Electromagnetic Waves.* New York: Pergamon, 1958.

[3] R. G. E. Hutter, *Beam and Wave Electronics in Microwave Tubes*. Princeton: D. Van Nostrand, 1960.

[4] G. D. Sims and I. M. Stephenson, *Microwave Tubes and Semiconductor Devices.* London: Blackie and Son, 1963.

[5] M. Chodorow anf C. Susskind, *Fundamentals of Microwave Electronics*. New York: McGraw Hill, 1964.

[6] J. W. Gewartowski and H. A. Watson, *Principles of Electron Tubes*. New Jersey: D. Van Nostrand, 1965.

[7] R. E. Collin, *Foundations for Microwave Engineering*. New York: McGraw Hill, 1966.

[8] S. Y. Liao, *Microwave Devices and Circuits*. Englewood Cliffs: Printice-Hall, 1985.

[9] A. S. Gilmour Jr, *Microwave Tubes*. Boston: Artech House, 1986.

[10] S. Y. Liao, *Microwave Electron Tubes*. New Jersey: Prentice-Hall, 1988.

[11] R. G. Carter, *Electromagnetic Waves, Microwave Components and Devices*. London: Chapman and Hall, 1990.

[12] L. Sivan, Microwave Tube Transmitters. London: Chapman and Hall, 1994.

[13] T. G. van de Roer, *Microwave Electronic Devices*. London: Chapman and Hall, 1994.

[14] E. F. Nicol, B. J. Mangus, and M. K. De Pano, "TWTA versus SSPA: A new look at boeing fleet on-orbit reliability data and comparison factors", in *Proc. Vacuum Electron. Conf. 2006*, Monterey, CA, USA, 2006, pp. 61–62.

[15] C. J. Edgcombe, *Gyrotron Oscillators: Their Principles and Practice*. London: Taylor and Francis, 1993.

[16] G. S. Nusinovich, *Introduction to the Physics of Gyrotrons*. Baltimore: Johns Hopkins University Press, 2004.

[17] M. V. Kartikeyan, E. Borie, and M. Thumm, *Gyrotrons High-Power Microwave and Millimeter Wave Technology*. Germany, Springer, 2004.

[18] V. S. Bajaj *et al.*, "250 GHz CW gyrotron oscillator for dynamic nuclear polarization in biological solid state NMR", *J. Magn. Reson.*, vol. 189, no. 2, pp. 251–279, 2007.

[19] J. M. Baird, "Survey of fast wave tube developments", in *Proc. Electron Devices Meeting Technical Digest*, Washington, USA, 1979, pp. 156–163.

[20] R. S. Symons and H. R. Jory, "Cyclotron resonance devices", *Adv. Electron. Electron Phys*., vol. 55, pp. 1–75, 1986.

[21] R. S. Symons, "Tubes still vital after all these years", IEEE Spectr., vol. 35, pp. 52–63, 1998.

[22] H. Steyskal, "Microwave tubes 1920–1990: A review of ideas and progress", *IETE Rev.*, vol. 9, pp. 81–85, 1992.

[23] V. A. Flyagin, A. V. Gaponov, I. Petelin, and V. K. Yulpatov, "The gyrotron", *IEEE Trans. Microw. Theory Tech.*, vol. 25, no. 6, pp. 514–521, 1977.

[24] R. Q. Twiss, "Radiation transfer and the possibility of negative absorption in radio astronomy", *Aust. J. Phys.*, vol. 11, pp. 567–579, 1958.

[25] A. V. Gaponov, "Interaction of irrectilinear electron flows with electromagnetic waves in waveguides", *Izv. VUZov Radiofiz.*, vol. 2, pp. 450–462, 1959.

[26] G. S. Nusinovich, E. Jerby, "Guest editorial", *IEEE Trans. Plasma Sci.*, vol. 27, no. 2, pp. 287–293, 1999.

[27] A. V. Gaponov, M. I. Petelin, and V. K. Yulpatov, "The induced radiation of excited classical oscillators and its use in high frequency electronics", *Radiophys. Quantum Electron*., vol. 10, no. 9–10, pp. 794–813, 1967.

[28] V. L. Granatstein, M. Herndon, R. K. Parker, and P. Sprangle, "Coherent synchrotron radiation from an intense relativistic electron beam", *IEEE J. Quantum Electron.*, vol. QE-10, no. 9, p. 651, 1974.

[29] V. L. Granatstein *et al*., "Microwave amplification with an intense relativistic electron beam", *J. Appl. Phys.*, vol. 46, no. 9, pp. 3800–3805, 1975.

[30] D. V. Kisel, G. S. Korablev, V. G. Pavelyev, M. I. Petelin, and S. H. E. Tsimring, "An experimental study of a gyrotron operating at the second harmonic of the cyclotron frequency, with optimized distribution of the high frequency field", *Radio Eng. Electron. Phys.*, vol. 19, pp. 95–100, 1974.

[31] Yu. V. Bykov and A. L. Goldenberg, "Influence of resonator profile on the maximum power of a cyclotron resonance maser", *Radiophys. Quantum Electron.*, vol. 18, no. 7, pp. 791–792, 1975.

[32] Yu. V. Bykov *et al.*, "An experimental investigation of a gyrotron with whispering-gallery modes", *Izv. VUZov Radiofiz.*, vol. 18, pp. 1544–1547, 1975.

[33] L. V. Nikolayev and M. M. Ofitserov, "A gyrotron with a pulsed magnetic field", *Radio Eng. Electron. Phys.*, vol. 19, pp. 139–140, 1974.

[34] N. I. Zaytsev, T. B. Pankratova, M. I. Petelin, and V. A. Flyagin, "Millimeter- and submillimeter wave gyrotrons", *Radio Eng. Electron. Phys.*, vol. 19, pp. 103–107, 1974.

[35] N. Vlasov, L. I. Zagryadskaya, and M. I. Petelin, "Transformation of a whispering gallery mode propagating in a circular waveguide, into a beam of waves", *Radio Eng. Electron. Phys*., vol. 12, no. 10, pp. 14–17, 1975.

[36] M. Thumm, "History, presence and future of gyrotrons", in *Proc. IEEE Int. Vacuum Electron. Conf. IVEC-2009*, Rome, Italy, 2009, pp. 37–40.

[37] "Wrocław Teraherz Team" [Online]. Available: http://www.thz.pwr.wroc.pl

[38] K. Yujong, "Applications of coherent terahertz light source and possibility at Indiana University", *Workshop on ICS and High Intensity Accelerators*, Bloomington, USA, 2010.

[39] "GlobalSecurity.org" [Online]. Available: http://www.globalsecurity.org/military/systems/ground/v-mads.htm

[40] "Death Ray Turns Warm and Fuzzy, Strategypage", Oct. 6, 2012 [Online]. Available: http://pl.wikipedia.org.wiki/Active_Denial_Systems

[41] "New Device Unveiled Intended to Stop or Lessen Inmate Assaults", L. A. County Sheriff, Aug. 20, 2010.

[42] A. A. Tolkachev, B. A. Levitan, G. K. Solovjev, V. V. Veytsel, and V. E. Farber, "A megawatt power millimeter-wave phased-array radar", *IEEE Aerosp. Electron. Syst. Mag.*, vol. 15, no. 7l, pp. 2–31, 2000.

[43] B. G. Danly *et al.*, "Development and testing of a high-average power, 94-GHz gyroklystron", *IEEE Trans. Plasma Sci*., vol. 28, no. 3, pp. 713–726, 2000.

[44] A. V. Gaponov-Grekhov and V. L. Granatstein, Eds., *Application of High Power Microwaves*. Boston: Artech House, 1994.

[45] H. J. Liebe, "MPM-an atmospheric millimeter-wave propagation model", *Int. J. Infrared Millimeter Waves*, vol. 10, pp. 631–650, 1989.

[46] R. M. Lhermitte, "Small cumuli observed with a 3 mm wavelength doppler radar", *Geophys. Res. Lett*., vol. 14, no. 7, pp. 707–710, 1987.

[47] W. M. Manheimer, "On the possibility of high power gyrotrons for super range resolution radar and atmospheric sensing", *Int. J. Electron.*, vol. 72, pp. 1165–1189, 1992.

[48] Y. Yang, M. Mandehgar, and D. R. Grischkowsky, "Understanding THz pulse propagation in the atmosphere, terahertz science and technology", *IEEE Trans*., vol. 2, no. 4, pp. 406–415, 2012.

[49] K. Chang, M. A. Pollock, M. K. Skrehot, G. Dickey, and J. Suddath, "System feasibility study of a microwave/millimeter-wave radar for space debris tracking", *Int. J. Infrar. Millim. Waves*, 1988.

[50] M. Lucente *et al*., "An innovative multimode millimeter wave radar for moon remote sensing" in *Proc. IEEE Aerosp. Conf.*, Big Sky, USA, 2009, pp. 1–8.

[51] J. F. Federici *et al.*, "THz imaging and sensing for security applications-explosives, weapons and drugs", *Semiconductor Sci. Technol.*, vol. 20, no. 7, pp. 266–280, 2005.

[52] K. Kawase, Y. Ogawa, and Y. Watanabe, "Non-destructive terahertz imaging of illicit drugs using spectral fingerprints", *Opt. Express*, vol. 11, pp. 2549–2554, 2003.

[53] G. S. Nusinovich *et al.*, "Development of THz gyrotrons with pulse solenoids for detecting concealed radioactive materials", in *Proc. 35th Int. Conf. Infrar. Millim. Terahertz Waves IRMMW-THz 2010*, Rome, Italy, 2010, pp. 1–2.

[54] S. Sabchevski and T. Idehara, "Development and applications of high-frequency gyrotrons in FIR FU", FIR Center Rep., Oct. 2011.

[55] S. Sabchevski, T. Idehara, S. Ishiyama, N. Miyoshi, and T. Tatsukawa, "A dual-beam irradiation facility for a novel hybrid cancer therapy", Tech. Rep., Jun 2012.

[56] A. S. Kesar *et al.*, "Design of a magnetron Injection Gun for a 670 GHz, 300 kW gyrotron, *IEEE Trans. Plasma Sci.*, vol. 39, no. 12, pp. 3337–3344, 2011.

[57] L. Barret, "High Power 95 GHz Gyro-Devices with Permanent or Conventional Solenoid Magnets, Mountain Technology" [Online]. Available: http://2008.www.virtualaquisitionshowcase.com/document/1249/briefing

[58] M. Thumm, "State-of-the-art of high power gyro-devices and free electron masers update 2010", Scientific Rep. FZKA 7575, Forschungszentrum Karlsruhe, Karlsruhe, Germany, 2010.

[59] J. M. Baird and W. Lawson, "Magnetron injection gun (MIG) design for gyrotron applications", *Int. J. Electron.*, vol. 61, pp. 953–96, 1986.

[60] S. Kern, "Numerische Simulation der Gyrotron-Wechselwirkung in koaxialen Resonatoren", Scientific Rep. FZKA 5837, Forschungszentrum Karlsruhe, Nov. 1996.

[61] W. Lawson, H. Ranghunathan, M. Esteban, Space-Charge Limited Magnetron Injection Gus for High-Power Gyrotrons, IEEE Trans. Plasma Sci. 35,3, pp. 1236-1241, 2004.

[62] S. Vlasov and I. M. Orlova, "Quasi-optical transformer which transforms the waves in a waveguide having a circular cross section into a highly-directionalwave beam", *Izv.VUZov. Radiofiz*, vol. 15, pp. 1913–1918, 1974.

[63] S. Vlasov, L. I. Zagryadskaya, and M. I. Petelin, "Transformation of a whispering gallery mode, propagating in a circular waveguide into a beam of waves", *Radiotekhnika i Elektronika*, vol. 20, pp. 2026–2030, 1975.

[64] R. L. Ives, "3rd harmonic W-Band Permanent Magnet Gyrotron", Calabazas Creek Research Inc., San Mateo 2009 [Online]. Available: http://www.virtualaquisitionshowcase.com/document/1158/briefing

[65] A. W. Cross *et al.*, "A W-band Gyro-BWO with a helical waveguide", in P*roc. 15th Int. Conf. on Teraherz Electr.*, Cardiff, UK, 2007, pp. 581–582.

Mariusz Hruszowiec graduated Applied Computer Science at the Wrocław University of Technology in 2012. At present he is Ph.D. student at Faculty of Electronics at the Wrocław University of Technology. The main topics of his interest are gyrotron theory, electromagnetic field theory and numerical methods.

E-mail: mariusz.hruszowiec@pwr.edu.pl
Telecommunication and Teleinformatics Department
Wrocław University of Technology
Janiszewskiego st 9
50-370 Wrocław, Poland

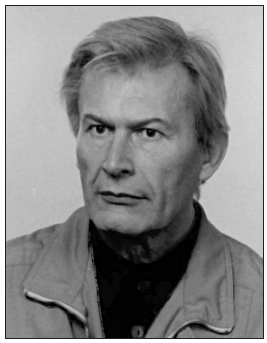

Wojciech Czarczyński received the M.Sc. Eng. in Electronics from the Wrocław University of Technology, Poland, in 1957. From 1956 to 1964 he was with the Industrial Institute of Electronics, Wrocław Branch (PIE). In the years 1964–1965 he was Research Fellow on ONZ Fellowship at the Southampton University involved in the design and research in the field of power microwave tubes. From 1965 to 1978 he was again with PIE as a head of microwave tube laboratory. In 1956 he received the Ph.D. degree in the electron beam research from the WUT. In 1978 he joined the Institute of Electron Technology, WUT, where he was involved in electron beam and plasma research. He was appointed the Institute Head for the 1987–1990 term. In 1995 he received D.Hab. degree from the Faculty of Electronics, WUT and was appointed University Professor. In 2001 he became full professor. He retired in 2003 and was a part-time research worker till 2008. Currently is the voluntary member of the Terahertz Center of the WUT, Wrocław, Poland.

E-mail: wojciech.czarczynski@pwr.edu.pl
Faculty of Microsystems Electronics and Photonics
Wrocław University of Technology
Janiszewskiego st 11/17
50-372 Wrocław, Poland

Edward F. Pliński received the Diploma degree in Physics, with specialization on Solid State Physics, from the University of Wrocław, in 1974 and the Ph.D. degree in Technical Sciences, with specialization on carbon dioxide lasers, from the Wrocław University of Technology in 1983. In 1985, he joined the Twente University, Enschede, the Netherlands, where he worked with a Professor W. J. Witteman's group on a waveguide carbon dioxide laser technology. In 2002, he received the D.Sc. degree in technology of RF excited carbon dioxide waveguide lasers. In 2006, he changed his subject of interest and he established the Wrocław Terahertz Team. From 2012 he is heading the Wrocław Terahertz Center at the Wrocław University of Technology. Currently, his subject of interest is terahertz technique and technology.

E-mail: edward.plinski@pwr.wroc.pl
Faculty of Electronics
Wrocław University of Technology
Wybrzeże Wyspiańskiego st 27
50-370 Wrocław, Poland

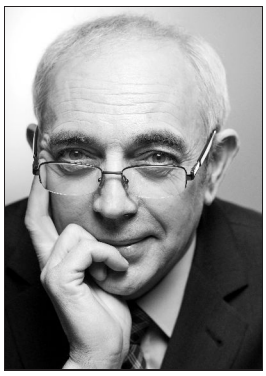

Tadeusz Więckowski specializes in the field of electromagnetic compatibility of device, systems and installations, in particular the intersystem compatibility of radio communication and telecommunication installations. He is the author of over 175 scientific publications, 6 patents and patent issues, and over 600 elaborations on economy. With the support of his colleagues he initiated, created and promoted the world class Electromagnetic Laboratory of Compatibility. One of his greatest successes is the creation of the Knowledge and Innovation Community for Information and Communication Technologies, and The Academic Incubator of Entrepreneurship at Wrocław University of Technology. For his scientific and teaching activity and cooperation with industry Professor Więckowski was twice awarded by the Prime Minister of Poland. He was honored with the Golden Badge of Wrocław University of Technology, Medal of the Commission of National Education and Silver and Gold Cross of Merit, Order of Rebirth of Poland. He is doctor honoris causa of Lviv Polytechnic National University, honorary professor of Obuda University. Currently he is rector of Wrocław University of Technology.

E-mail: Tadeusz.Wieckowski@pwr.wroc.pl
Institute of Telecommunications and Acoustics
Wrocław University of Technology
Wybrzeże Wyspiańskiego st 27
50-370 Wrocław, Poland

Paper

An Ontological Framework for Representing Clinical Knowledge in Decision Support Systems

Marco Iannaccone and Massimo Esposito

National Research Council of Italy, Institute for High Performance Computing and Networking, Naples, Italy

Abstract—In the last decades, clinical evidence and expert consensus have been encoded into advanced Decision Support Systems (DSSs) in order to promote a better integration into the clinical workflow and facilitate the automatic provision of patient specific advice at the time and place where decisions are made. However, clinical knowledge, typically expressed as unstructured and free text guidelines, requires to be encoded into a computer interpretable form suitable for being interpreted and processed by DSSs. For this reason, this paper proposes an ontological framework, which enables the encoding of clinical guidelines from text to a formal representation, in order to allow querying, advanced reasoning and management in a well defined and rigorous way. In particular, it jointly manages declarative and procedural aspects of a standards based verifiable guideline model, named GLM-CDS (GuideLine Model for Clinical Decision Support), and expresses reasoning tasks that exploit such a represented knowledge in order to formalize integrity constraints, business rules and complex inference rules.

Keywords—Clinical Practice Guidelines, Decision Support Systems, Ontology, Rules, Unstructured Data.

1. Introduction

In the last years, healthcare has been more and more characterized by an extensive practice variation and overuse, underuse, and misuse of medical resources. To address these issues, both clinical evidence and expert consensus have been systematically captured and joined to encode Clinical Practice Guidelines (CPGs), aimed at supporting general practitioners in making clinical decisions and managing medical actions about appropriate healthcare for specific clinical circumstances [1], [2].

Most CPGs, however, are expressed in a text-based format and, thus, are not easily accessible to care providers, who need to apply them either at the time and place where clinical decisions are made, or to assess the quality of their application, retrospectively.

Even if, recently, CPGs have been published also in electronic formats, such as HTML or PDF files, they are poorly adopted and examined by care providers [3], who rarely have the time to utilize the valuable knowledge, encoded in the guidelines, during the treatment of their patients. Therefore, there is a need to facilitate automated guideline specification, dissemination, application, and quality assessment in order to realize the actual potential of CPGs in improving health outcomes.

Several recent studies have suggested that automation might be realized by encoding CPGs into advanced Decision Support Systems (DSSs), i.e., computer-based systems designed to promote a better integration into the clinical workflow and to facilitate the automatic provision of patient-specific advice at the time and place where decisions are made [2], [4]. However, this requires clinical knowledge, expressed into an unstructured and free-text format, to be encoded as computer-interpretable guidelines (CIGs), suitable for being interpreted and processed by DSSs.

Even if, in the recent past, many knowledge representation formalisms have been developed to address this issue, it remains strongly critical, since a mismatch exists between the unstructured narrative form of published CPGs and the formality that is necessary for the operationalization of clinical knowledge in CIGs for DSSs. Moreover, the poverty of the methodological rigor typically used to computerize guideline knowledge further complicates this operationalization, which might generate malformed, incomplete, or even inconsistent CIGs.

For this reason, this paper proposes an ontological framework, which enables the encoding of CPGs from text to a formal representation, where domain knowledge, clinical process structures and data, and the behavioral semantics of such processes are encoded in order to allow querying, advanced reasoning and management in a well-defined and rigorous way.

In particular, it jointly manages declarative and procedural aspects of a standards-based verifiable guideline model, named GuideLine Model for Clinical Decision Support (GLM-CDS) [5], and expresses reasoning tasks that exploit such a represented knowledge in order to formalize integrity constraints, business rules and complex inference rules.

The solution here proposed is particularly relevant for the design and development of a CIG, enabling the possibility of inferring implicit knowledge not expressly formulated or verifying the consistency and coherency of the knowledge explicitly modeled.

The rest of the paper is organized as follows. Section 2 outlines an overview of the state-of-the-art solutions. In Section 3, the proposed framework is described by referring to the guideline model used, i.e. GLM-CDS. Section 4

depicts an example application in order to highlight how the proposed framework can be used to formalize an existing guideline defined in GLM-CDS. Finally, Section 5 concludes the work.

2. Related Work

To date, the effort in defining new solutions for computerizing CPGs has produced many process-flow-like models, such as SAGE [6], GLIF [7], Asbru [8], EON [9] and PROforma [10], which are characterized by different coverage and particularities in order to represent both the structure of the domain-specific knowledge, named declarative knowledge, and the process-oriented knowledge, named procedural knowledge.

In particular, declarative knowledge concerns the domain compositional elements, such as raw and abstract concepts, their properties and inter-relations explicitly expressed in the CPGs.

On the other hand, procedural knowledge captures the control-flow logic to be modelled by providing suggestions about the actions to be taken or conclusions to be drawn from *declarative knowledge*, as well as constraints between tasks, temporal constraints in a global plan, and so on [11].

All the above-mentioned models are process-flow-like and share same basic procedural elements: some kind of action/decision tasks, some implicit or explicit mechanisms for coordination or synchronicity of actions, the ability to create sub-plans or sub-guidelines, the possibility of storing the state of a guideline which is being executed and synchronizing the management of a patient with the corresponding parts of a guideline by means of some entry/exit points [11].

Various types of actions can be supported, such as medically-oriented (e.g., recommending the administration of a particular substance) or programming-oriented (e.g., notifying a message to a care provider).

Moreover, two basic types of decisions are mainly defined: decisions in the form of if-then-else choices and decisions requiring a heuristic choice from a set of rule-in and rule-out conditions that support or oppose alternatives [12].

A drawback common to all these proposals is represented by the lack of a seamless integration of both declarative and procedural knowledge expressed in a CPG by means of a highly expressive and formal framework able to jointly manage control-flow and domain-specific aspects and express reasoning tasks to automatically infer implicit knowledge or verify a number of desired properties of correctness, coherency and well-formedness of a CIG, also with respect to the time perspective.

The solution here proposed has been conceived to face these issues by expressing in a combined way domain ontologies, clinical processes, related decision and inference rules, and integrity constraints, as described in the following sections.

3. The Ontological Framework for Computerizing CPGs

The formal framework here proposed is aimed at computerizing CPGs by defining a guideline model, named GLM-CDS, and by encoding such a model through a hybridization of the theoretic semantics of ontology and rule languages.

Deeply speaking, the proposed model GLM-CDS consists of a control-flow part, which is based on a formal Task-Network Model (TNM) for codifying CPGs in terms of structured tasks connected with transition dependencies between them from an initial state of the patient.

Domain-specific knowledge is coded through an information model built on the top of the Domain Analysis Model, Release 1 of the HL7 Virtual Medical Record [13] (HL7 vMR-DAM) issued by HL7 Clinical Decision Support-Working Group. This information model is populated by using existing standard terminological resources, such as Logical Observation Identifiers Names and Codes (LOINC) [14] and Systematized NOmenclature of MEDicine (SNOMED) [15].

Data types used in GLM-CDS resemble the ones defined in the HL7 vMR DAM, which gives a simplified/constrained version of ISO 21090 data types, based on the abstract HL7 version 3 data types specification, release 2 [16].

The control flow part is formally defined as the following 8-tuple:

$$C_f = \langle G, E_n, E_x, T, C, D_r, I_r, C_s \rangle \,, \tag{1}$$

where:

- G indicates the set of *sub-guidelines* included into a CPG,
- E_n and E_x represent the *entry point* and the *exit point* of the TNM modeling a CPG,
- T represents the set of *tasks* composing a CPG,
- C is the set of *connections* between the nodes of a TNM,
- D_r is the set of *decision rules*, which relate a decision node to a task node and are used at runtime to automatically control the execution flow of a process,
- I_r is the set of *inference rules*, which combine known knowledge to produce ("infer") new information,
- C_s is the set of *constraints*, which have to be verified in order to preserve the correctness, coherency and consistency of the CPG modeled.

Moreover, T is partitioned into the following sub-sets:

- D is the set of *decision* nodes for directing the control-flow from a point into the TNM to various alternatives,

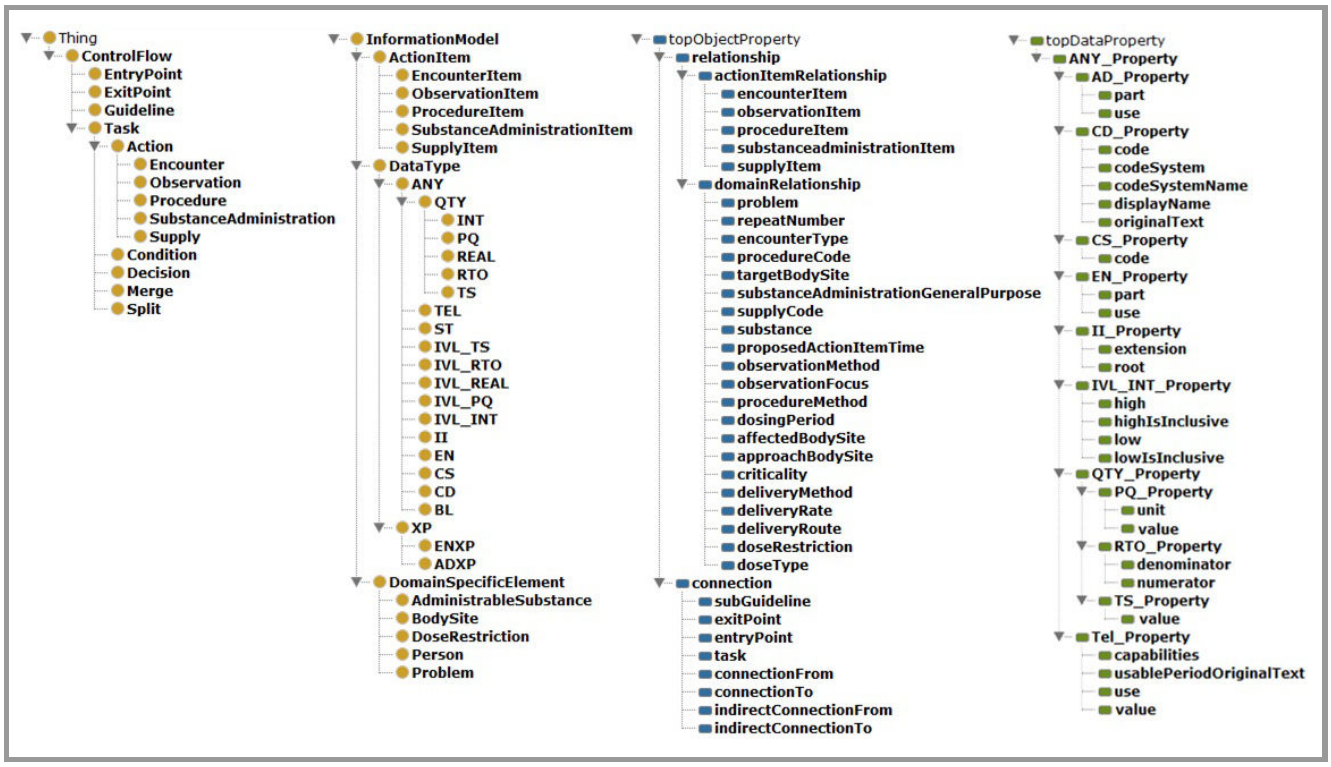

Fig. 1. A compacted perspective of both ontology concepts and roles formalized in GLM-CDS.

- C_n is the set of *conditions*, defined as observable states of the patient that persist over time and tend to require intervention or management,
- S indicates the set of *split* nodes, which enable to branch the guideline flow to multiple parallel tasks,
- M indicates the set of *merge* nodes, which enable to synchronize parallel tasks by making them converging into a single point,
- A models the set of high level *actions* to be performed and is further specialized into the following sub-sets:
  - A_O is the set of *observations*, which are used to determine a measurement, a laboratory test or a user input value,
  - A_S models the set of *supplies*, which are aimed at providing some clinical material or equipment to a patient,
  - A_E is the set of *encounters*, which are applied to request an appointment between a patient and healthcare participants for assessing his health status,
  - A_P represents the set of *procedures*, whose outcome is the alteration of the patient's physical condition,
  - A_{SA} refers to the set of *substance administrations*, which allow giving a substance to a patient for enabling a clinical effect.

Furthermore, C is also composed by the following sub-sets:

- C_d indicates the set of *direct connections* between pairs of nodes of a TNM without other intermediary nodes,
- C_i indicates the set of *indirect connections* between pairs of nodes of a TNM with other intermediary nodes.

Finally, C_s is partitioned into:

- IC_s indicates the set of *integrity constraints* devised to detect violations, errors and/or missing information in the TNM encoding a CPG,
- TC_s represents the set of *temporal constraints* formulated according to some time patterns, i.e. task duration, periodicity, deadline, scheduling and time lags.

On the other hand, the information model is formalized as the following 5-tuple:

$$I_m = \langle A_I, E_D, R_D, P_D, D_T \rangle \,, \tag{2}$$

where:

- A_I models the set of elementary and repeatable *action items*, associated to each action and specialized into:
  - I_O the set of *observation items*,
  - I_S the set of *supply items*,
  - I_E the set of *encounter items*,
  - I_P the set of *procedure items*,
  - I_{SA} the set of *substance administrations*.

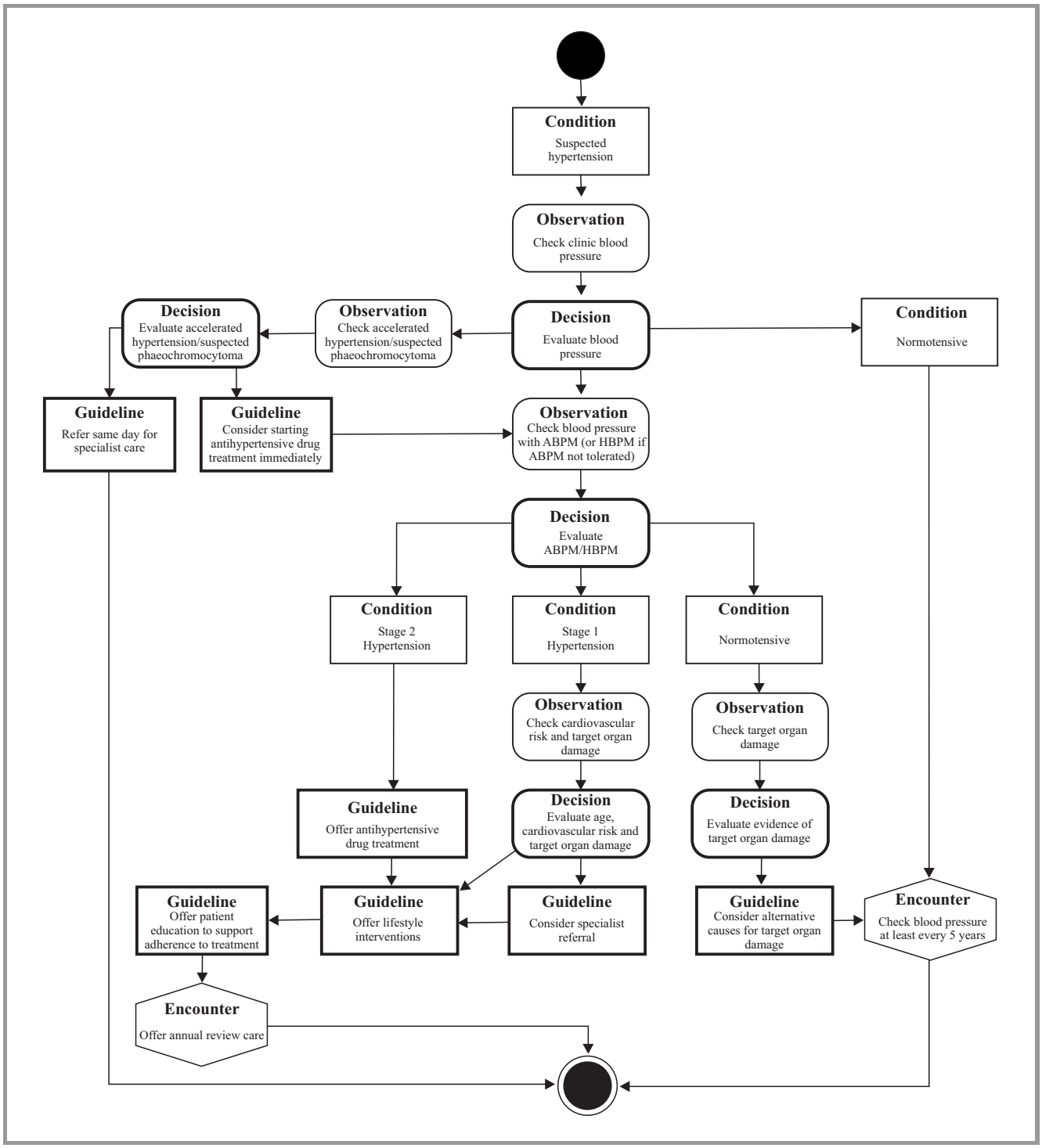

Fig. 2. A fragment of the NICE guideline for hypertension in adults encoded in GLM-CDS.

- E_D models the set of *domain-specific elements*, such as *Administrable Substance, Dose Restriction* or *Body Site*, which are linkable to the action items,
- R_D indicates the set of relationships existing between:
  - *action items* and *domain specific* concepts,
  - *action items* and *data types*,
  - *domain-specific concepts* and *data types*,
  - elements belonging to the subset $G \cup E_n \cup E_x \cup T$ of the control flow part and *data types*.
- P_D represents the set of properties used for specifying values a data type can assume,
- D_T models the set of data types used in GLM-CDS.

This guideline model has been encoded by exploiting the theoretic semantics of ontology and rule languages.

In detail, ontology languages rely on decidable fragments of first order logic and are based on the notions of concepts (unary predicates, classes), individuals (instances of concepts), abstract roles (binary predicates between concepts) and concrete roles (binary predicates between concepts and data values).

On the other hand, rule languages are widely considered in literature as a syntactic and semantic extension to ontology languages. Indeed, rules have been widely used as a new kind of axiom to define abstract roles as well as arithmetic relationships between data values assumed by concrete roles.

As a result, a subset of the control flow part C_f of GLM-CDS, i.e. $G \cup E_n \cup E_x \cup T$, as well as a subset of its information model I_m, i.e. $A_I \cup E_D \cup D_T$, have been encoded as ontology concepts. Furthermore, the sets C of C_f and R_D of I_m have been encoded by means of ontology abstract roles, whereas the set P_D of I_m has been formalized by using ontology concrete roles.

Figure 1 reports a compacted perspective of ontology concepts and abstract roles formalized in GLM-CDS.

The sets D_r and I_r of decision and inference rules are formulated by using the Horn Clause Logic. In particular, decision and inference rules are expressed as definite Horn clauses, in the form:

$$h_1(X_1) \leftarrow b_1(Y_1) \wedge \cdots \wedge b_k(Y_k), \tag{3}$$

where the clause $h_1(X_1)$ is named head, the clauses $b_1(Y_1) \ldots b_k(Y_k)$ (with $k \geq 0$) are called *body*, $h_1, b_1 \ldots b_k$ are rule predicates and $X_1, Y_1 \ldots Y_k$ are tuples of variables or constants. Rule predicates are built by using ontology concepts and roles and by using ontology individuals as constants. Moreover, each variable in the head is obliged to appear also in the body of a rule, so granting soundness and completeness of the reasoning process.

Finally, the sets IC_s and TC_s of integrity and temporal constraints are expressed as negative Horn clauses, in the form:

$$\leftarrow b_1(Y_1) \wedge \cdots \wedge b_k(Y_k), \tag{4}$$

where no clause is reported in the head. For the sake of uniformity with decision and inference rules, each constraint is associated with a special predicate C_s , which indicates whether it is violated, as formulated in (5):

$$C_s \leftarrow b_1(Y_1) \wedge \cdots \wedge b_k(Y_k). \tag{5}$$

4. An Example Application: a CIG for Hypertension in Adults

This section reports, as an example, the application of GLM-CDS to the CPG for the "Clinical management of primary hypertension in adults", issued by the National Institute for Health and Care Excellence (NICE).

A fragment of this CPG, containing recommendations on blood pressure measurement, the use of ambulatory/home blood pressure monitoring (ABPM/HBPM) and the management of hypertension, has been encoded according to the GLM-CDS as shown in Fig. 2.

A partial translation of this fragment of CPG into its ontological representation is given in Fig. 3.

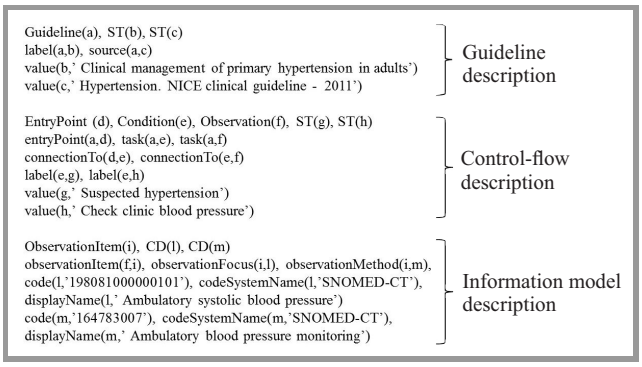

Fig. 3. A partial translation of a fragment of the guideline into its ontological representation.

In detail, the CPG is first described, by listing some relevant information, such as its name and source. Next, the first three nodes, i.e. the Entry Point, the Condition named "Suspected hypertension" and the Observation named "Check clinic blood pressure", of the control-flow part reported in Fig. 2 are formalized as ontology concepts and roles.

Finally, with respect to Observation named "Check clinic blood pressure", a specific Observation Item is codified, whose roles *observationFocus* and *observationMethod* are valued according to the data type *CD* of the HL7 vMR-DAM.

An example of decision rule, associated to the Decision node named "Evaluate blood pressure", is reported in Fig. 4. It evaluates whether the systolic blood pressure is less than 140 mmHg.

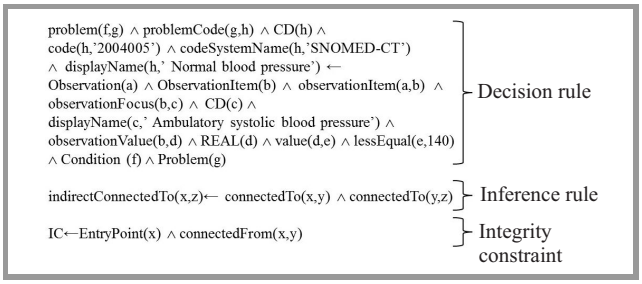

Fig. 4. Some examples of decision rules, inference rules and integrity constraints.

Moreover, an inference rule, which defines the role *indirectConnectionTo* starting from the role *connectionTo*, is also reported.

Finally, an example of integrity constraint is also codified, which states that each Entry Point node of a CPG is not admissible to have a direct connection from any other node.

5. Conclusion

To date, the different attempts proposed for encoding CPGs in a computer interpretable form suitable for DSSs are not fully concerned with enabling an intuitive and, contextually, formal representation of CPGs, in terms of their logic, the clinical processes involved and the different types of clinical knowledge represented.

For this reason, this paper proposed an ontological framework for encoding CPGs from text to a formal representation, by jointly managing declarative and procedural aspects of a standards based verifiable guideline model, named GLM-CDS, and expressing reasoning tasks that exploit such a represented knowledge in order to formalize integrity and temporal constraints, business rules and complex inference rules.

The strength of this solution relies on the support to design and develop a CIG, by enabling the possibility of inferring implicit knowledge not expressly formulated or verifying the consistency and coherency of the knowledge explicitly modelled.

In order to promote and facilitate the widespread use of this framework, ongoing activities are being carried out to design and realize an ad hoc, intuitive and user friendly authoring tool for encoding CPGs graphically and, successively, translating them into a formal representation expressed in terms of ontology concepts and roles, as well as decision/inference rules and integrity/temporal constraints.

Acknowledgements

This work has been partially supported by the Italian project "ASK-Health" Advanced system for the interpretation and sharing of knowledge in the healthcare sector.

References

[1] B. S. Bloom, "Crossing the quality chasm: a new health system for the 21st century", *JAMA: The J. Amer. Medical Assoc.*, vol. 287, no. 5, pp. 646–647, 2002.

[2] M. J. Field and K. N. Lohr, *Guidelines for Clinical Practice: From Development to Use*. Washington: National Academy Press, 1992.

[3] F. A. Sonnenberg and C. G. Hagerty, "Computer-interpretable clinical practice guidelines: Where are we and where are we going?", *Methods Infor. Med.*, vol. 45, no. 1, pp. 145–158, 2006.

[4] F. Moscato, V. Vittorini, F. Amato, A. Mazzeo, and N. Mazzocca, "Solution workflows for model-based analysis of complex systems". *IEEE Trans. Autom. Sci. Engin.*, vol. 9, no. 1, pp. 83–95, 2012.

[5] M. Iannaccone, M. Esposito, and G. De Pietro, "A standards-based verifiable guideline model for decision support in clinical applications", in *Process Support and Knowledge Representation in Health Care*, D. Riano, R. Lenz, S. Miksch, M. Peleg, M. Reichert, and A. Teije, Eds. Springer, 2013, pp. 143–157.

[6] S. W. Tu *et al.*, "The SAGE guideline model: Achievements and overview", *J. Am. Med. Inform. Assoc.*, vol. 14, pp. 589–598, 2007.

[7] A. A. Boxwala *et al.*, "GLIF3: a representation format for sharable computer-interpretable clinical practice guidelines", *J. Biomed. Inform.*, vol. 37, no. 3, pp. 147–161, 2004.

[8] A. Seyfang, S. Miksch, and M. Marcos, "Combining diagnosis and treatment using Asbru", *Int. J. Med. Inform.*, vol. 68, no. 1, pp. 49–57, 2002.

[9] S. W. Tu and M. A. Musen, "Modeling data and knowledge in the EON guideline architecture", *Stud. Health. Technol. Inform.*, vol. 84, no. 1, pp. 280–284, 2001.

[10] J. Fox and N. Johns, "Rahmanzadeh A. Disseminating medical knowledge: the PROforma approach", *Artif. Intell. Med.*, vol. 14, pp. 157–181, 1998.

[11] D. Isern and A. Moreno, "Computer-based execution of clinical guidelines: a review", *Int. J. Med. Inform.*, vol. 77, pp. 787–808, 2008.

[12] P. De Clercq, K. Kaiser, and A. Hasman, "Computer-interpretable guideline formalisms", *Stud. Health. Technol. Inform.*, vol. 139, pp. 22–43, 2008.

[13] "HL7 Virtual Medical Record (vMR) Project Wiki", Health Level 7 [Online]. Available: http://wiki.hl7.org/index.php?title=Virtual_Medical_Record_(vMR)

[14] "Logical Observation Identifiers Names and Codes (LOINC)", Regenstrief Institute, Inc and the LOINC Committee [Online]. Available: http://loinc.org/

[15] "Systematized Nomenclature of Medicine (SNOMED)", International Health Terminology Standards Development Organisation [Online]. Available: http://www.ihtsdo.org/snomed-ct/

[16] "HL7 Reference Information Model, Version 3", Health Level 7 [Online]. Available: http://www.hl7.org/implement/standards/rim.cfm

Marco Iannaccone is a research assistant at the Institute for High Performance Computing and Networking (ICAR) of the National Research Council of Italy (CNR). He received his M.Sc. in Computer Science Engineering from University of Naples Federico II in 2004. Since July 2012, he has been a member of the iHealthLab – Intelligent Healthcare laboratory. His research interests cover knowledge representation and ontologies for healthcare processes, process modeling, interoperability and standards in healthcare, workflow management in healthcare. His research is described in scientific articles published in international conferences.

E-mail: marco.iannaccone@na.icar.cnr.it
National Research Council of Italy (CNR)
Institute for High Performance Computing
and Networking (ICAR)
Via Pietro Castellino, 111
80131, Naples, Italy

Massimo Esposito is a scientific researcher at the Institute for High Performance Computing and Networking (ICAR) of the National Research Council of Italy (CNR). He received his M.Sc. in Computer Science Engineering (Cum Laude) from University of Naples Federico II in 2004. He received a University 1st level Master

degree, named European Master on Critical Networked Systems in 2007, and a Ph.D. degree in Information Technology Engineering in 2011 from the University of Naples Parthenope. Since 2007, he has been a member of the Advanced Medical Imaging and Computing labOratory (AMICO), developed from a cooperation agreement between the Institute of Biostructure and Bioimaging (IBB) and ICAR of CNR. Since 2011, he has been a member of the iHealthLab – Intelligent Healthcare laboratory. His research interests cover pervasive computing, knowledge-based medical decision support systems, knowledge discovery in biomedical databases, workflow management in healthcare. His research is described in many scientific articles published in international conferences and journals. He participates in the editorial boards of many international journals and has been on the program committee of many international conferences.

E-mail: massimo.esposito@na.icar.cnr.it
National Research Council of Italy (CNR)
Institute for High Performance Computing
and Networking (ICAR)
Via Pietro Castellino, 111
80131, Naples, Italy

Information for Authors

Journal of Telecommunications and Information Technology **(JTIT)** is published quarterly. It comprises original contributions, dealing with a wide range of topics related to telecommunications and information technology. **All papers are subject to peer review**. Topics presented in the JTIT report primary and/or experimental research results, which advance the base of scientific and technological knowledge about telecommunications and information technology.

JTIT is dedicated to publishing research results which advance the level of current research or add to the understanding of problems related to modulation and signal design, wireless communications, optical communications and photonic systems, voice communications devices, image and signal processing, transmission systems, network architecture, coding and communication theory, as well as information technology.

Suitable research-related papers should hold the potential to advance the technological base of telecommunications and information technology. Tutorial and review papers are published only by invitation.

Manuscript. TEX and LATEX are preferable, standard Microsoft Word format (.doc) is acceptable. The author's JTIT LATEX style file is available:
http://www.nit.eu/for-authors

Papers published should contain up to 10 printed pages in LATEX author's style (Word processor one printed page corresponds approximately to 6000 characters).

The manuscript should include an abstract about 150–200 words long and the relevant keywords. The abstract should contain statement of the problem, assumptions and methodology, results and conclusion or discussion on the importance of the results. Abstracts must not include mathematical expressions or bibliographic references.

Keywords should not repeat the title of the manuscript. About four keywords or phrases in alphabetical order should be used, separated by commas.

The original files accompanied with pdf file should be submitted by e-mail: redakcja@itl.waw.pl

Figures, tables and photographs. Original figures should be submitted. Drawings in Corel Draw and PostScript formats are preferred. Figure captions should be placed below the figures and can not be included as a part of the figure. Each figure should be submitted as a separated graphic file, in .cdr, .eps, .ps, .png or .tif format. Tables and figures should be numbered consecutively with Arabic numerals.

Each photograph with minimum 300 dpi resolution should be delivered in electronic formats (TIFF, JPG or PNG) as a separated file.

References. All references should be marked in the text by Arabic numerals in square brackets and listed at the end of the paper in order of their appearance in the text, including exclusively publications cited inside. Samples of correct formats for various types of references are presented below:

[1] Y. Namihira, "Relationship between nonlinear effective area and mode field diameter for dispersion shifted fibres", *Electron. Lett*., vol. 30, no. 3, pp. 262–264, 1994.

[2] C. Kittel, *Introduction to Solid State Physics*. New York: Wiley, 1986.

[3] S. Demri and E. Orłowska, "Informational representability: Abstract models versus concrete models", in *Fuzzy Sets, Logics and Knowledge-Based Reasoning*, D. Dubois and H. Prade, Eds. Dordrecht: Kluwer, 1999, pp. 301–314.

Biographies and photographs of authors. A brief professional author's biography of up to 200 words and a photo of each author should be included with the manuscript.

Galley proofs. Authors should return proofs as a list of corrections as soon as possible. In other cases, the article will be proof-read against manuscript by the editor and printed without the author's corrections. Remarks to the errata should be provided within one week after receiving the offprint.

A copy of the JTIT is provided to each author of paper published.

Journal of Telecommunications and Information Technology has entered into an electronic licencing relationship with EBSCO Publishing, the world's most prolific aggregator of full text journals, magazines and other sources. The text of *Journal of Telecommunications and Information Technology* can be found on EBSCO Publishing's databases. For more information on EBSCO Publishing, please visit www.epnet.com.

(*Contents Continued from Front Cover*)

INSTYTUT ŁĄCZNOŚCI
PAŃSTWOWY INSTYTUT BADAWCZY

Editorial Office

National Institute
of Telecommunications
Szachowa st 1
04-894 Warsaw, Poland

tel. +48 22 512 81 83
fax: +48 22 512 84 00
e-mail: redakcja@itl.waw.pl
http://www.nit.eu